The Role of Instability in Gaseous Detonation

Thesis by

Joanna M. Austin

In Partial Fulfillment of the Requirements

for the Degree of

Doctor of Philosophy

California Institute of Technology

Pasadena, California

2003

(Submitted May 21st, 2003)

© 2003
Joanna M. Austin
All Rights Reserved

Acknowledgements

I would firstly like to thank Prof. Joe Shepherd for his great insight, enthusiasm, and support which resulted in an enormously rewarding and challenging experience during my graduate study. I would also like to thank Prof. Hans Hornung for numerous extremely helpful ideas along the course of this work, and the other members of my doctoral committee, Profs. Dale Pullin, Don Cohen and Tony Leonard, for their suggestions and guidance during my time at Caltech.

I would particularly like to thank and acknowledge Florian Pintgen for his invaluable contribution in developing the PLIF system for use in detonations. I also gratefully acknowledge many enjoyable and helpful discussions with and assistance from past graduate students and post-docs Chris Eckett, Mike Kaneshige, Eric Schultz, Julian Lee, and present students Marco Arienti, Tony Chao, Marcia Cooper, Patrick Hung, Scott Jackson, Dan Lieberman, Eric Wintenberger, and Marty Grunthaner.

Pavel Svitek, Joe Haggerty, Larry Frazier, Ali Kiani, and Brad St. John provided a great deal of technical and machining assistance over the years of my research, and Suzy Dake's organizational and secretarial skills are very much appreciated. Dr. Vadim Gamezo from the Office of Naval Research kindly shared his data with me.

I would particularly like to thank my parents for their inspiration and support and finally, and most importantly, my husband Giles.

This research was partially funded by a Multidisciplinary Research Program of the University Research Initiative (MURI) award from the Office of Naval Research.

Abstract

In detonation, the coupling between fluid dynamics and chemical energy release is critical. The reaction rate behind the shock front is extremely sensitive to temperature perturbations and, as a result, detonation waves in gases are always unstable. A broad spectrum of behavior has been reported for which no comprehensive theory has been developed. The problem is extremely challenging due to the nonlinearity of the chemistry-fluid mechanics coupling and extraordinary range of length and time scales exhibited in these flows. Past work has shown that the strength of the leading shock front oscillates and secondary shock waves propagate transversely to the main front. A key unresolved issue has emerged from the past 50 years of research on this problem: What is the precise nature of the flow within the reaction zone and how do the instabilities of the shock front influence the combustion mechanism?

This issue has been examined through dynamic experimentation in two facilities. Key diagnostic tools include unique visualizations of superimposed shock and reaction fronts, as well as short but informative high-speed movies. We study a range of fuel-oxidizer systems, including hydrocarbons, and broadly categorize these mixtures by considering the hydrodynamic stability of the reaction zone. From these observations and calculations, we show that transverse shock waves do not essentially alter the classic detonation structure of Zeldovich-von Neumann-Döring (ZND) in weakly unstable detonations, there is one length scale in the instability, and the combustion mechanism is simply shock-induced chemical-thermal explosion behind a piecewise-smooth leading shock front. In contrast, we observe that highly unstable detonations have substantially different behavior involving large excursions in the lead shock strength, a rough leading shock front, and localized explosions within the reaction zone. The critical decay rate model of Eckett et al. (2000) is combined with experimental observations to show that one essential difference in highly unstable waves is that the shock and reaction front may decouple locally. It is not clear

how the ZND model can be effectively applied in highly unstable waves. There is a spectrum of length scales and it may be possible that a type of "turbulent" combustion occurs. We consider how the coupling between chemistry and fluid dynamics can produce a large range of length scales and how possible combustion regimes within the front may be bounded.

Contents

List of Figures

List of Tables

Chapter 1 Detonation Structure

1.1 Introduction

This work is an experimental study of detonation front structure aimed at understanding the time-dependent instability of the front that results in i) quasi-periodic variations in the shock front velocity, ii) associated disturbances in the chemical species. We study fully developed detonation waves propagating through a channel or tube filled with a quiescent, premixed, combustible gas using non-intrusive measurements and visualizations of the front. As the structure of the detonation front is dependent on the confining geometry, two experimental facilities of different cross sections were used, one of which was built for this study. 270 experiments were carried out in the new facility, in addition to numerous experiments in the existing facility, to cover a range of mixture parameters and to capture the front at different phases. The purpose of this study is to make detailed observations of the front in order to improve our understanding of the nature of the instability and the governing physical and chemical processes.

A detonation is a supersonic (M $\sim$ 5) combustion wave consisting of a leading shock front followed by a reaction zone. The shock heats and compresses the reactant gas and, after some induction time, rapid chemical energy release occurs. The volumeric gas expansion due to the reaction supports the shock wave. The coupling between the shock and reaction is a critical mechanism in detonation propagation and occurs on length scales on the order of 0.1-10 mm for fuel-oxygen-diluent mixtures.

All unsupported detonation waves in gases are experimentally observed to be unstable. This was discovered by optical visualizations (White, 1961) and by using the so-called "soot-foil" technique (Denisov and Troshin, 1959, Shchelkin and Troshin, 1964). A shadowgraph of a detonation front in a hydrocarbon mixture from our study is shown in Fig. 1.1 (a). In this front, the induction length scale is 1.2 mm and is not clearly

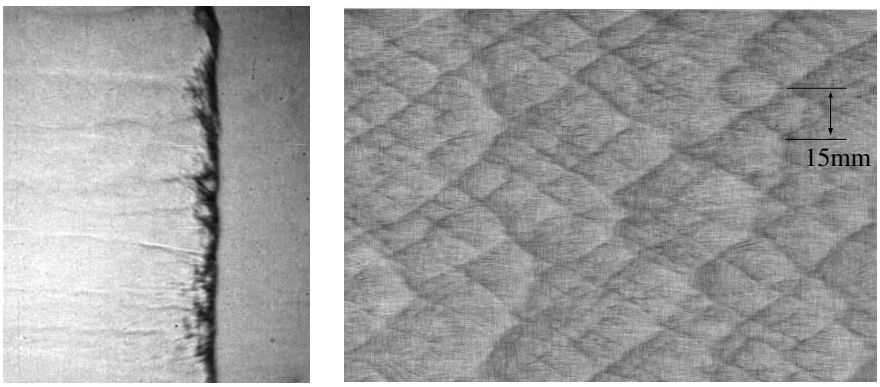

(a) (b)

Figure 1.1: (a) Shadowgraph of detonation front propagating from left to right in a channel in C_2H_4-$3O_2$-$6N_2$, P_1=20 kPa (Shot nc268). Image height is 82 mm. (b) Soot foil from detonation in C_2H_4-$3O_2$-$5N_2$, P_1=20 kPa (Shot nc49). The soot foil was mounted to the wall of a channel while the detonation passed over it. The cellular pattern that remains is due to the instability of the front. Image height is 75 mm.

resolved. Disturbances in the lead shock profile and transverse shock waves can be seen. An example of a soot foil is shown in Fig. 1.1 (b). When a detonation passes over a lightly sooted surface, a pattern is left scoured in the soot. The "cellular" pattern is a manifestation of the instability of the front and occurs on length scales on the order of 1-300 mm for gaseous fuel-oxygen-diluent mixtures. In Fig. 1.1 (b), the length scale of the instability, called the cell width, is about 15 mm.

One of the main goals of this study is to explain differences associated with the structure of the instability that have been observed in mixtures with different chemical composition. Mixtures highly diluted with a monotonic gas such as argon are observed to have a "regular" or more organized structure in comparison to undiluted mixtures with "irregular" or disorganized structure. Detonations with regular structure appear to have distinctly different macroscopic behavior than those with irregular structure and parameters such as initiation energy, failure diameter, and critical tube diameter all appear to scale differently. While most previous experimental studies of detonation front structure have concentrated on mixtures with regular instabilities, mixtures with irregular instabilities, such as hydrocarbons, are most important for detonation applications to

practical problems of explosion hazard analysis.

The length scales of the detonation and nature of the instability may be controlled by adjusting the chemical composition of the mixture and initial conditions. We consider a number of fuel-oxidizer systems that are representative of fronts with different macroscopic behavior and choose the initial pressure to result in resolvable structure. We focus in particular on two extremes: weakly unstable fronts and highly unstable fronts. The original contributions of this study include overlaid visualizations of the shock and reaction fronts in propagating detonations. High-speed shadowgraph movies were made to obtain time-resolved data. A critical question that is addressed is how the coupling between the shock and reaction, for which we have only one-dimensional, steady models, is affected by the instability of the front in mixtures with different chemical composition.

1.2 Historical background

The instability of the front and appearance of transverse waves in an unsupported detonation front was first observed by White (1961) using interferometry and subsequently imaged using schlieren techniques by several researchers (Voitsekhovskii et al., 1963, Nagaishi et al., 1971, Edwards et al., 1972, Strehlow and Crooker, 1974, Takai et al., 1974, Subbotin, 1975). These early studies resulted in an understanding of the main features in a weakly unstable propagating detonation, such as occurs in mixtures highly diluted with a monotonic gas such as argon. The structure is shown schematically in two dimensions in Fig. 1.2. The lead shock undergoes cyclic oscillations in space and in time. Transverse waves propagate perpendicularly to the the overall direction of detonation propagation and collide periodically with waves of the opposite family as the detonation propagates forward. After a collision, there is a region of high temperature and pressure and the local lead shock is accelerated with respect to weaker neighboring portions. As the front moves forward, the local gas expands and the shock strength decays smoothly until the next transverse wave collision. The oscillation of the front is referred to as a "cell" cycle. The smoothly decaying velocity of the lead shock along the centerline through one cell

cycle is shown in Fig. 1.2 (b). This data is from a numerical study by Eckett (2000); experimental measurements have also been made by Voitsekhovskii et al. (1963), Lundstrom and Oppenheim (1969), and Dormal et al. (1979). The instability of the front is a coupled longitudinal-transverse instability, involving periodic oscillations of the lead shock and the transverse waves in space and in time.

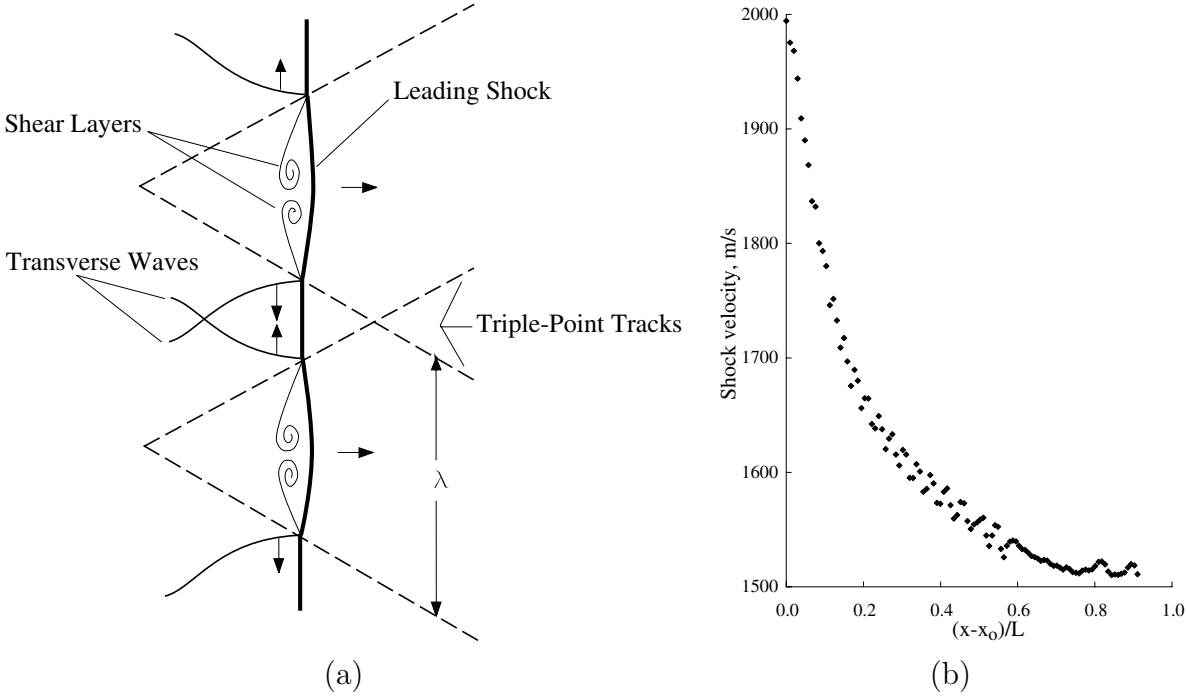

Figure 1.2: (a) 2-D schematic of detonation front propagating from left to right. Triple point tracks (dashed lines) form a cellular pattern as the detonation propagates forward. (b) Lead shock velocity along the centerline of one cell as a function distance from the apex at the collision of two triple points, from two-dimensional numerical simulation by Eckett (2000) in $2H_2$-O_2-7Ar, P_1=6.67 kPa.

Triple points exist at the junction of the leading shock front and a transverse wave and the pattern observed on soot foils is a history of the triple point tracks in the propagating detonation front. Urtiew and Oppenheim (1966) have shown that the tracks are closely associated with the triple points on the detonation front, although the precise physical mechanism by which the tracks are made in the soot layer is still unclear. The width of cells that appear on the foil are a measure of the spacing of the transverse waves in the

detonation front. This global length scale, referred to as the detonation cell width, λ, can not in general be calculated a priori but may be related to the induction zone length by a constant of proportionality A. The constant is different for fuel-O_2 and fuel-air mixtures (Westbrook, 1982) and also varies with the equivalence ratio (Shepherd, 1986). However, the induction zone length and cell width are approximately proportional for a wide range of mixtures and can be empirically related to dynamic parameters such as the critical initiation energy (Lee, 1984).

Experimental detection of chemical species in a detonation wave has proven difficult. Natural chemiluminescence has been the most common way to locate reacting portions of a detonation front. Chemiluminescence has also been a significant obstacle to the development of techniques that are able to make direct, resolved images of chemical species (Andresen et al., 1992). Dormal et al. (1979) combined OH emission spectroscopy with soot foils and pressure traces to measure induction time along the cell centerline. Deflagration to detonation transition was studied using planar laser induced predissociated fluorescence (LIPF) by Gerlach (1996) and Eder (2001), and recently Pintgen (2000) was successful in using planar laser induced fluorescence (PLIF) to detect OH radicals in detonation waves. This visualization technique, together with schlieren and soot foils, is used in the present work.

1.2.1 Characterization of the front

The cell width and the regularity of the cellular pattern have been traditionally used to characterize detonation waves and also make inferences about the structure and propagation mechanism of the detonation front. It can be observed from soot foils that some mixtures appear to have an easily identifiable, dominant cell width and a regular structure, while other mixtures have a broader spectrum of length scales and a more irregular structure (see Fig. 1.3).

A classification of various mixtures by the regularity of the cellular structure observed on soot foils was carried out by Strehlow (1969) and by Libouton et al. (1981). H_2-O_2

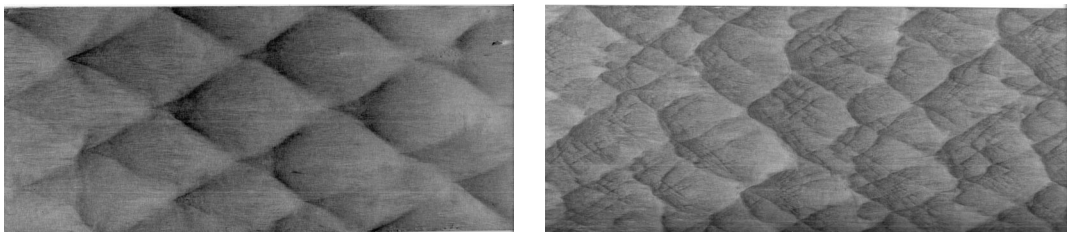

(a) (b)

Figure 1.3: Sample soot foils with (a) regular cellular structure in $2H_2$-O_2-17Ar, P_1=20 kPa (Shot nc38) and (b) irregular structure in C_3H_8-$5O_2$-$9N_2$, P_1=20 kPa (Shot nc47). Detonation propagated from left to right and foils were mounted downstream of the window section of the narrow channel. Image height is 152 mm.

with more than 60% argon dilution were found to have excellent regularity. There was no apparent effect in H_2-O_2 with up to 50% N_2 dilution. The addition of CO_2 was also found not to improve the regularity. C_2H_4-$3O_2$ soot foils were reported to be considerably more complex than hydrogen-oxygen foils. The regularity of CH_4-$2O_2$ and C_3H_8-$5O_2$ mixtures was classified as poor. These classifications are based on rather subjective observations and serve only to define broad categories.

A more quantitative analysis of regularity was made by Shepherd et al. (1986) who used peaks in the power spectral density computed from digital images of soot foils to identify the frequencies present. Their results confirm the classification described by Strehlow (1969) for hydrogen and acetylene with argon and nitrogen dilution. Regularity of cellular structure has been linked to the activation energy of the mixture (Ul'yanitskii, 1981) and mixtures with higher activation energy generally have a more irregular structure. However, Shepherd et al. (1986) found that this parameter does not fully account for the observed variations in a systematic way.

1.2.2 Detonation structure and propagation

Although classification of detonation structure by regularity is not rigorous, it has been useful in the sense that there is evidence of differences in structure and propagation mechanism in detonation fronts with different chemical composition which loosely correspond

to classification by regularity. As discussed above, soot foils from hydrocarbon mixtures have a range of length scales while soot foils from highly argon-diluted hydrogen-oxygen have one dominant cell width. Parameters such as initiation energy, failure diameter, and critical tube size have all been reported to scale differently for regular vs. irregular mixtures. Several experimental studies have reported the dynamic response of detonation fronts to changes in boundary conditions is dependent on the regularity of the cellular structure. In a study of the influence of cellular regularity on detonation propagation in small tubes (relative to the cell width), Moen et al. (1984) measured the minimum wave velocity U_{meas} and calculated a corresponding velocity deficit δU=(U_{meas} - U_{CJ})/U_{CJ} for a variety of mixtures. They report that regular mixtures, such as C_2H_2-2.5O_2-75%Ar, have a velocity deficit on the order of 10% while irregular mixtures, such as C_2H_2-Air, propagate at minimum speeds closer to the CJ value with deficits on the order of 2%.

Radulescu and Lee (2002), building on the work of DuPre et al. (1988), studied the failure mechanism of detonation in a variety of mixtures by propagating the wave over a porous wall. From steak photographs of light emission, they define a distance to failure x_F, and find $x_F \sim 100\lambda$ for Ar-diluted mixtures and $x_F \sim 3 - 7\lambda$ for undiluted hydrocarbon mixtures. They conclude that the failure occurs in Ar-diluted mixtures by mass and momentum loss from the detonation front due to the porosity, while in the hydrocarbon mixtures, failure occurs when attenuation of transverse waves at the porous wall overcomes their spontaneous generation in the front.

Studies of detonation diffraction from a tube into an unconfined volume have found that the critical tube diameter for successful transmission of the detonation front d_c may be empirically related to the cell width λ of the mixture, but the scaling factor increases with increasing mixture regularity (Moen et al., 1986, Desbordes, 1988). $d_c = 13\lambda$ has been reported as a scaling for irregular mixtures, while for regular mixtures, the ratio increases to $d_c = 40\lambda$. For a given detonation length scale and a given facility dimension, a mixture with irregular cellular structure will successfully transition through the area change while a mixture with regular cellular structure may fail.

Experimental visualizations, such as schlieren images from Takai et al. (1974). con-

firm differences in regularity between Ar-diluted H_2-O_2 mixtures and N_2-diluted H_2-O_2 observed on soot foils. Resolved visualizations of detonation front structure in other fuel-oxidizer systems are limited. In regular, Ar-diluted, mixtures, the instability appears dominated by a single scale while a more random variation in structure across a larger range of scales is observed in irregular, N_2-diluted mixtures. These images are difficult to interpret however, due to the three-dimensionality of the front. The appearance of highly unstable fronts in schlieren images such as Fig. 1.1 have lead some researchers (Lee, 1991) to question whether alternate combustion mechanisms need to be considered. In particular, do the highly irregular fronts involve a distributed or turbulent combustion mechanism in contrast to the laminar, shock-induced chain-branching/thermal explosion that is observed in very regular fronts? This issue is addressed in the present work.

1.3 Detonation theory

1.3.1 Chapman-Jouguet theory

There are two classical models of detonation. The simplest theory, due to Chapman (1899) and Jouguet (1905), considers a control volume containing a shock followed by a reaction zone. The conservation equations are applied across the control volume:

$$\rho_1 w_1 = \rho_2 w_2 \tag{1.1}$$

$$\rho_1 w_1^2 + P_1 = \rho_2 w_2^2 + P_2 \tag{1.2}$$

$$h_1 + 1/2 w_1^2 = h_2 + 1/2 w_2^2 \tag{1.3}$$

where w, ρ, P, h are the shock-fixed flow velocity, the density, the pressure, and the specific enthalpy. States 1 and 2 are upstream (reactants) and downstream (products) of the control volume.

The Chapman-Jouguet theory states that the product Hugoniot is tangent to the Rayleigh line and, as a consequence, the flow is sonic at the equilibrium point (state 2).

Mixture	U_{CJ} (m/s)
$2H_2$-O_2-17Ar	1415.0
$2H_2$-O_2-4.5N_2	1874.3
H_2-N_2O-2N_2	1925.5
C_3H_8-5O_2-9N_2	1934.4

Table 1.1: Chapman-Jouguet (CJ) velocities for some sample mixtures calculated using STANJAN, P_1=20 kPa, T_1=297 K.

A major result of the Chapman-Jouguet (CJ) theory is the calculation of a detonation wave speed, U_{CJ}. An equilibrium code such as STANJAN (Reynolds, 1986) may be used to calculate the detonation wave speed, thermodynamic properties, and species mole fractions at the CJ, or equilibrium, plane. Experimentally, detonation waves speeds are measured to be within 2% of the calculated CJ velocity.[1] Calculated CJ velocities are shown in Table 1.1 for some sample mixtures considered in this study. A full list is given in Appendix C.

The CJ velocity may also be approximately calculated from the conservation equations using the so-called two-gamma model which assumes the specific heat ratio has a constant value for the products, γ_1, and the reactants, γ_2. as shown in Eqn. 1.4.

$$\frac{U_{CJ}}{c_1} = \sqrt{H + \frac{(\gamma_1+\gamma_2)(\gamma_2-1)}{2\gamma_1(\gamma_1-1)}} + \sqrt{H + \frac{(\gamma_2-\gamma_1)(\gamma_2+1)}{2\gamma_1(\gamma_1-1)}} \tag{1.4}$$

where

$$H = \frac{(\gamma_2-1)(\gamma_2+1)Q}{2\gamma_1} \tag{1.5}$$

$$Q = \frac{h_R^o}{RT_1} \tag{1.6}$$

where h_R^o is the heat of reaction at absolute zero. It can be seen that the detonation velocity U_{CJ} is a function of initial conditions, the specific heat ratio, and the chemical

[1] if the facility is large with respect to the length scale of the cellular instability.

energy content of the mixture. In this work, the parameter Q is calculated by inverting Eqn. 1.4 where M_{CJ}, γ_1, and γ_2 are calculated by STANJAN.

1.3.2 Zel'dovich-von Neumann-Döring (ZND) theory

The Zel'dovich-von Neumann-Döring or ZND model (Zel'dovich, 1940, von Neumann, 1942, Döring, 1943) builds on the CJ theory and includes a finite reaction rate. The steady, reactive Euler equations, Eqns. 1.7-1.10, are solved to calculate thermodynamic property and chemical species profiles through the detonation wave with either detailed chemical reaction mechanisms or a simplified approximation such as one-step irreversible reactions.

$$w\frac{d\rho}{dx} = -\rho\frac{dw}{dx} \tag{1.7}$$

$$w\frac{dw}{dx} = -\frac{1}{\rho}\frac{dP}{dx} \tag{1.8}$$

$$\frac{de}{dx} = \frac{P}{\rho^2}\frac{d\rho}{dx} \tag{1.9}$$

$$w\frac{dY_i}{dx} = \Omega_i \qquad i = 1, ..., N \tag{1.10}$$

where w, ρ, P, e are the flow velocity in the shock-fixed frame, the density, the pressure, and the specific internal energy. Y_i is the mass fraction of species i and Ω_i is the production rate of species i, given by a kinetic rate law.

The equations may be rewritten

$$w\frac{d\rho}{dx} = -\frac{\rho\dot{\sigma}}{1-M^2} \tag{1.11}$$

$$w\frac{dw}{dx} = \frac{w\dot{\sigma}}{1-M^2} \tag{1.12}$$

$$w\frac{dP}{dx} = -\frac{\rho w^2\dot{\sigma}}{1-M^2} \tag{1.13}$$

$$\dot{\sigma} = \sum_i^N \frac{\Omega_i}{\rho c^2}\left(\frac{\partial P}{\partial Y_i}\right)_{\rho,e,Y_{k\neq i}} \tag{1.14}$$

where $\dot{\sigma}$ is the thermicity. To avoid singularity, the Mach number must approach one as the thermicity approaches zero. The condition is fulfilled at the equilibrium state behind a wave traveling at the CJ velocity.

Thermodynamic properties and species mole fractions through the reaction zone may be calculated using a numerical solution of the one-dimensional ZND model (Shepherd, 1986) together with validated detailed chemical kinetics mechanisms and CHEMKIN II (Kee et al., 1989) subroutines. A sample calculation of temperature and OH mole fraction is shown in Figure 1.4. The post-shock state consists of a thermally neutral region called the induction zone. The induction zone is terminated by a region of rapid radical formation and chemical energy release. The distance Δ between the shock and the location of maximum heat release is defined as the induction length (Shepherd, 1986). The induction length is a function of the initial conditions, mixture composition, chemical reaction rate, and a strong function of the leading shock velocity, Fig. 1.4 (b). This parameter is a length scale that may be used to characterize the thickness of the front from a theoretical viewpoint.

1.3.3 Constant volume explosion assumption

For detonations traveling at or above the CJ velocity, the ZND model may be used for calculations of induction length, and thermodynamic properties and species mole fractions through the reaction zone, as shown in Fig. 1.4. For sub-CJ waves, the induction time, thermodynamic properties and species mole fractions may be estimated by assuming a particle undergoes a constant volume, adiabatic explosion after the lead shock. The constant volume numerical calculation (Shepherd, 1986) is zero-dimensional, and uses a detailed chemical kinetics mechanism.

The induction time τ may be related to the induction length by multiplying by the post-shock velocity w_{vN}. The induction length has been empirically correlated to the

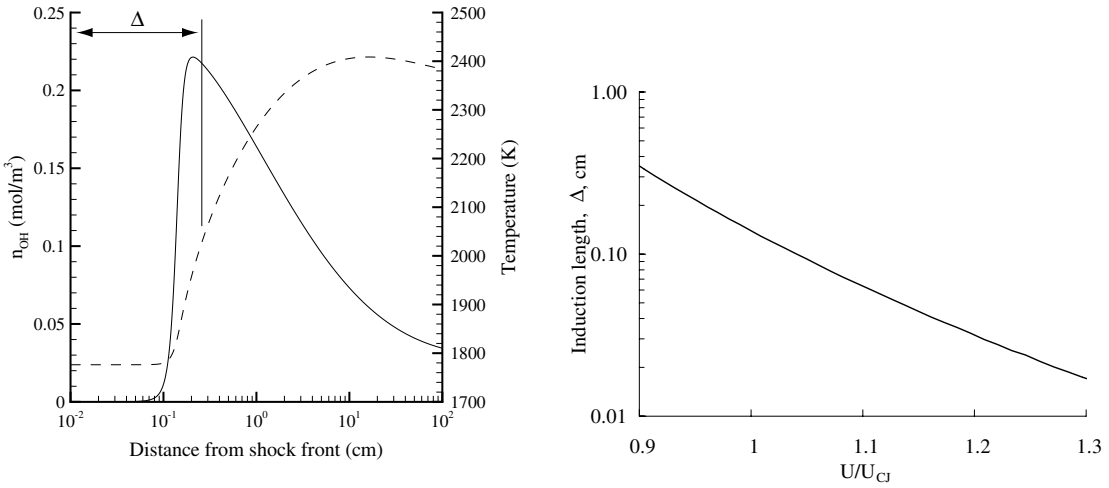

(a) (b)

Figure 1.4: (a) OH number density and temperature ZND profiles for a CJ detonation in $2H_2$-O_2-17Ar at 20 kPa initial pressure. The solid line corresponds to OH number density, the dashed line to the temperature profile. The detailed chemical kinetics mechanism of Warnatz and Karbach (1997) is used. The lead shock is located at x=0. (b) Induction length Δ as a function of the lead shock strength. The induction length is calculated using the constant-volume, adiabatic explosion assumption for a particle behind the lead shock, as described in the text.

instability length scale, the cell width λ

$$\Delta = w_{vN}\tau \ , \tag{1.15}$$

$$\lambda = A\Delta \ . \tag{1.16}$$

The constant A has a range $10 \leq A \leq 100$. The value of A is different for fuel-O_2 and fuel-air mixtures (Westbrook, 1982), and also to varies with the equivalence ratio (Shepherd, 1986). However, the induction zone length and cell width are approximately proportional for a wide range of mixtures. The detonation cell width λ can not in general be calculated a priori and is instead measured from soot foils.

An induction time calculated using a detailed chemical kinetics mechanism may be

represented by the approximation

$$\tau = C[\text{fuel}]_1^a[\text{oxidizer}]_i^b \exp\left(\frac{E_a}{R_g T_{vN}}\right) , \tag{1.17}$$

where C, a, b are empirical constants, E_a is the activation energy, and T_{vN} is the post-shock temperature. An effective activation energy, defined as $\theta = E_a/R_g T_{vN}$, may be calculated by considering the effect of a change in the lead shock velocity U (Schultz and Shepherd, 2000). Two constant volume explosion simulations are run with initial conditions $1.01U$ for state 1 and $0.99U$ for state 2. Interpreting the results with a one-step reaction leads to

$$\theta = \frac{1}{T_{vN}} \frac{\ln \tau_2 - \ln \tau_1}{\frac{1}{T_2} - \frac{1}{T_1}} \tag{1.18}$$

where T_1 and T_2 are post-shock temperatures corresponding to the velocities U_1=$1.01U$ and U_2=$0.99U$ respectively.

1.3.4 Stability analysis

Both the CJ and ZND models assume the flow is one-dimensional and steady in the wave frame. In fact, propagating gaseous detonation waves are experimentally observed to be unstable. The instability results from the strong coupling between the chemical reactions and the lead shock strength and may be illustrated by considering a one-step reaction mechanism, where Z is the product mass fraction.

$$\frac{DZ}{Dt} = k(1 - Z) \exp\left(\frac{-E_a}{RT}\right) \tag{1.19}$$

A small perturbation in the leading shock strength will produce a perturbation in the post-shock temperature. The chemical reaction rate has an Arrhenius form and so is very sensitive to temperature perturbations. As can be seen from the leading order expression given in Eqn. 1.21, a key parameter in the feedback between the gas dynamics and the chemical reactions is the activation energy, which acts to amplify perturbations

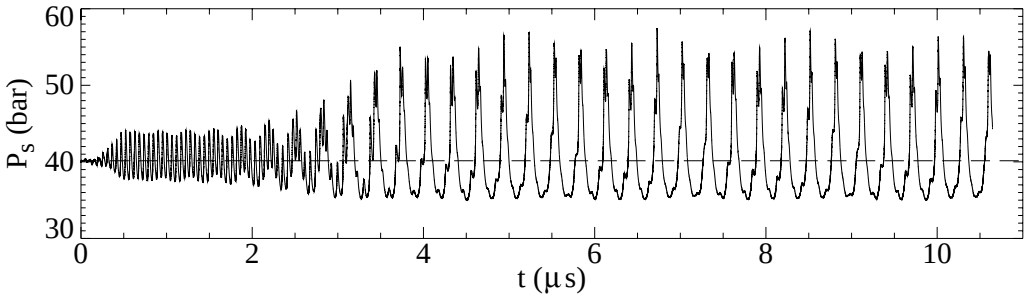

Figure 1.5: Post-shock pressure vs time from a one-dimensional detonation simulation with detailed chemistry by Eckett (2000) (Fig.3.7).

in the post-shock temperature.

$$\frac{T'}{T_{vN}} \approx \frac{2M'}{M_{CJ}} \tag{1.20}$$

$$\frac{DZ'}{Dt} \approx k(1-Z)\exp\left(\theta\frac{T'}{T_{vN}}\right) \tag{1.21}$$

where $\theta = E_a/RT_{vN}$, the normalized effective activation energy, ranges from 5 to 15 (Fig.1.6) and is usually considered to be a large parameter in analytic studies.

The result of the instability may be a limit cycle oscillation of the front. A numerical simulation from Eckett (2000) is shown in Fig. 1.5. Perturbations in the post-shock pressure are amplified until a limit cycle is reached. In multi-dimensions, the detonation may also be unstable to transverse perturbations and the instability results in secondary or transverse shock waves that perturb the leading shock front.

Hydrodynamic stability analysis of detonation waves was first performed by Erpenbeck (1964) using Laplace transforms in both one and two dimensions. A small perturbation is made on the shock speed and all the flow properties $(\rho, P, \underline{u}, Z)$ about a spatially dependent base state given by solutions to ZND equation set with initial conditions taken from (frozen) shock jump conditions. The relevant mixture parameters for their model are: the chemical energy Q, and the activation energy E. The third parameter, the over-

drive f, is defined as $f = (U/U_{CJ})^2$. Instability was determined pointwise and stability boundaries were interpolated. Erpenbeck found an approximate range of transverse wave numbers over which the system was unstable.

A normal modes analysis in one dimension about the steady (ZND) solution was carried out by Lee and Stewart (1990). An irreversible one-step reaction with progress variable λ is assumed. The analysis is carried out in the shock-fixed coordinate x

$$x = x_{lab} - (\tilde{D}/\tilde{c})t - \psi(t) \tag{1.22}$$

where x_{lab} is the lab frame coordinate, $\tilde{D}$ and $\tilde{c}$ are the detonation velocity and speed of sound in the steady (ZND) solution, and ψ is the perturbation to the shock. The ZND equations are linearized and solutions are found to a normal modes expansion of the form

$$z = \tilde{z}(x) + z'(x)\exp(\alpha t) \tag{1.23}$$

$$\psi = \psi' \exp(\alpha t) \tag{1.24}$$

where z is the vector (v, u, P, λ), $\tilde{z}$ is the steady solution, and the prime variables are a small perturbation. Neutral stability boundaries, growth rates, and oscillation frequencies were calculated.

This work was subsequently extended to include two-dimensional transverse instability by Short and Stewart (1998). The analysis was again in the shock-fixed frame

$$x = x_{lab} - (\tilde{D}/\tilde{c})t - \psi(y, t) \tag{1.25}$$

and considered a normal modes expansion of the form

$$z = \tilde{z}(x) + z'(x)\exp(\alpha t + iky) \tag{1.26}$$

$$\psi = \psi' \exp(\alpha t + iky) \tag{1.27}$$

Growth rates and frequencies as a function of transverse wave number are reported. The

frequencies at which the maximum growth rates are calculated do not correspond well with experimentally measured cell widths, but the results do show an increased range of unstable wavelengths at higher normalized activation energy θ, where cellular structure is generally found to be more irregular. For example fixing the parameters f=1, Q=50, and γ=1.2, a single low-frequency unstable mode (with maximum growth rate at about k=1) is present at θ=4.94 and a second, higher frequency mode (with maximum growth rate at about k=2.5) appears if θ is increased to 6.05. Neutral stability boundaries were calculated for various parameters. Short and Stewart found that increasing the lead shock velocity or f leads to sequential suppression of high frequency modes, so that at higher overdrive only a limited range of frequencies remains unstable until at sufficiently high overdrive only one low frequency mode is unstable. Except in the case of infinitely low energy release, the detonation can not be overdriven to be stable to transverse instability (although this is possible in the case of longitudinal disturbances).

All these analyses consider irreversible, one-step kinetics. An extension to a three-step chemical system in one dimension was made by Short and Quirk (1997). The three-step model consisted of a chain-initiation and chain-branching step, followed by a chain-termination step. They identify a "cross-over" temperature below which the detonation is stable. If the cross-over temperature is increased, successively more frequencies become unstable until chaotic behavior is observed.

As discussed in Section 1.2.1, the structure of detonation wave has traditionally been classified by the regularity of the cellular structure as observed on soot foils. However, quantitative comparison of cellular regularity is difficult and in this study, we will instead order detonation front structure using results from linear stability analysis. Three stability parameters have been identified by these studies: normalized chemical energy release Q, normalized activation energy E_a/RT_{vN}, and overdrive f. Eckett (2000) showed that if the CJ Mach number M_{CJ} is used as a parameter instead of the chemical energy release, the neutral stability curve is independent of γ. In Fig. 1.6, we show the neutral stability curve from Lee and Stewart for a CJ (f=1) detonation. Also shown are the stability parameters for mixtures considered in this study. Two broad categories of detonation

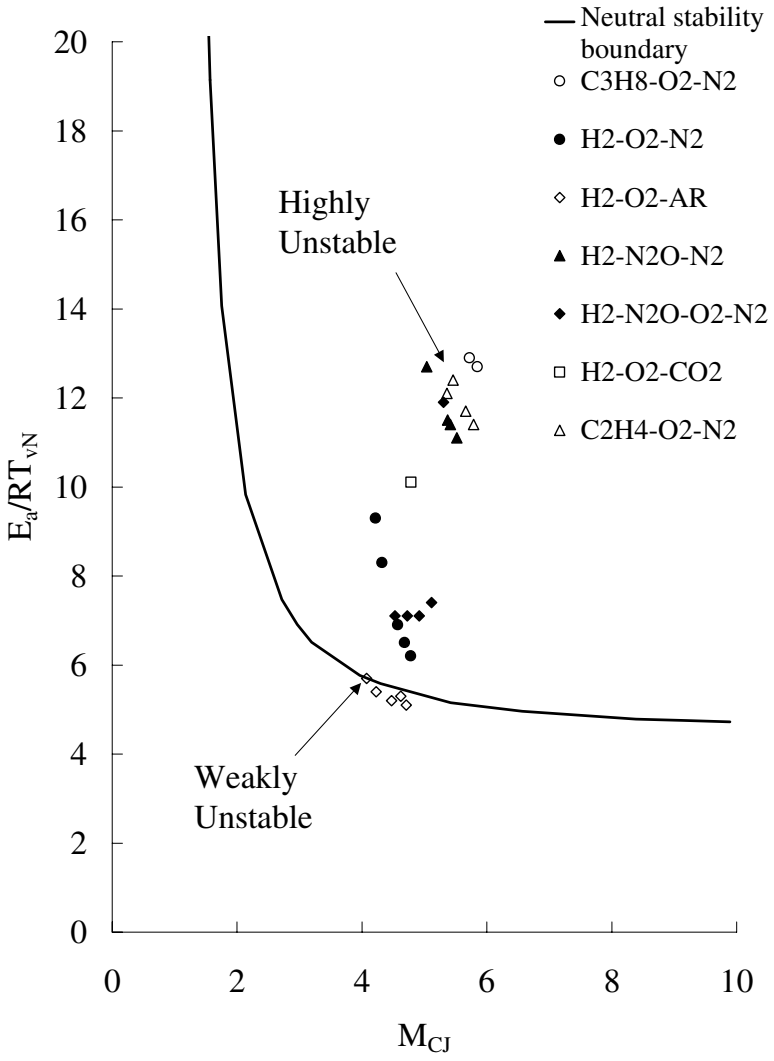

Figure 1.6: Categorization of detonation front structure from stability considerations. Parameters for mixtures considered in this study (symbols) are compared to the neutral stability boundary from Lee and Stewart (1990). Activation energy is calculated using the procedure described in Schultz and Shepherd (2000) from one-dimensional constant volume explosion assumption with detailed kinetics. M_{CJ} is calculated using STANJAN.

front structure may be defined in this figure: weakly unstable detonation and highly unstable detonation.

1.3.5 Numerical simulations

Numerical studies of detonation are challenging due to several reasons. Detailed chemical kinetics dramatically increase the required computational time. Most simulations to date include only one-step reaction, but detailed chemical kinetics for the hydrogen-oxygen system were used in simulations by Oran et al. (1998) and Inaba and Matsuo (2001). Gamezo et al. (1999b) used a one-step reaction with different activation energies to study the appearance and nature of unreacted gas pockets downstream of the front, and the oscillation of the centerline velocity. These results are discussed in more detail in Chapter 4. Several results from a simulation by Eckett (2000) with an ILDM-reduced mechanism for argon-diluted hydrogen-oxygen are used in the present work. Simulations in three dimensions with detailed kinetics in hydrogen-oxygen-argon were recently made by Deiterding (2003). Khoklov (2003) is currently running three-dimensional simulations with a simplified mechanism representing ethylene-air.

Simulating detonation with sufficient resolution to capture the reaction zone is also challenging due to the large range of time scales involved, particularly in highly unstable system with large excursions in the lead shock velocity. Sharpe (2001) shows that simulations with insufficient numerical resolution may predict an artificially accelerated reaction rate.

1.4 Thesis Outline

A discussion of the goals of this work, a summary of previous work on detonation structure, and a discussion of the relevant theory are contained in Chapter 1.

Chapter 2 gives a description of the two experimental facilities used in this study, together with a description of the advantages and limitations of each facility. Experimental procedures and diagnostics are described.

Chapter 3 discusses the influence of confining geometry of the facility on detonation structure, including the motivation for constructing the narrow channel. An attempt was made to suppress or weaken out-of-plane waves by relection from a porous wall. The motivation, experiment description, and results of this work are given here.

In the main part of this study, two extreme types of detonation instability were considered: weakly unstable fronts and highly unstable fronts. Results for each are given separately in the next two chapters. Chapter 4 presents results for weakly unstable fronts. Structures are analyzed using triple point calculations and zero-dimensional reactive calculation along particle paths. Chapter 5 presents results for highly unstable fronts, including a discussion of the increased lead shock oscillation, local decoupling of the front using the CDR model of Eckett et al. (2000), and structure over a range of scales. A statistical approach to analyzing front structure is proposed.

Chapter 6 is a speculative discussion of how detonation regimes may be bounded. A comparison with turbulent combustion and the Broghi diagram is made.

Conclusions and future work are discussed in Chapter 7.

Chapter 2 Experimental Setup

Two experimental facilities of different cross sections were used in this study: the gaseous detonation tube (GDT) and the narrow channel facility (NC). The two facilities have different advantages and limitations; they are used together to extend the generality of our results. In the GDT facility, the wave is a fully developed, self-sustaining (CJ) detonation, although a transient region occurs during the transition from a round geometry to a 150×150 mm square test section. The detonation structure is fully three-dimensional in the square test section of the GDT but this creates difficulties for flow visualization techniques that integrate through the test volume. The second facility, the narrow channel, has a constant 152×18 mm cross section and was built for this study. The facility is designed to weaken or suppress the detonation instability in one dimension, simplifying the flow field for integrating visualization techniques (discussed in greater detail in Section 3). Suppressing one plane of the instability results in some differences in the detonation structure. In particular, Strehlow and Crooker (1974) report the track angle and the calculated transverse wave strength are increased. Narrow channels were used by several researchers in the 1960's and 1970's to obtain schlieren images of detonation structure in very regular fronts. The construction of the present facility had three motivations. Schlieren could be combined with the newly developed OH PLIF capability (Pintgen, 2000) to locate the lead shock front and position in the cell cycle. The facility dimension was carefully chosen (Section 3.1) and is 2-3 times the size of previous facilities to allow the work on weakly unstable detonation to be extended to highly unstable, hydrocarbon mixtures. In addition, chemiluminescence is reduced, so that the current PLIF imaging technique could be used in hydrocarbon detonations.

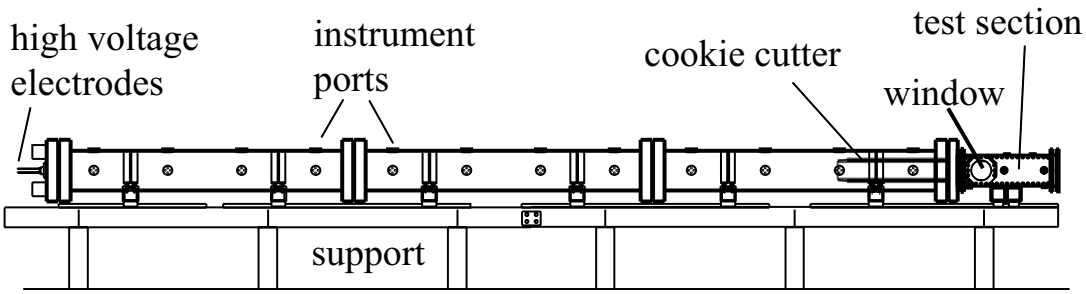

Figure 2.1: Schematic of the GDT facility.

2.1 Facility description

The GDT (Akbar, 1997), shown in Fig.2.1, consists of a stainless steel detonation tube which is 7.3 m long and has an internal diameter of 280 mm. A "cookie-cutter" is used to attach the tube to a 150 mm square test section described in Kaneshige (1999). 184 mm diameter windows provide optical access to the test section approximately 7.5 m from the initiation point. In performing an experiment, the entire tube is first evacuated to about 10 Pa and then filled by the method of partial pressures. Pressure in the tube is measured by an electronic Heise 901a gauge which is accurate to $\pm$ 0.17 kPa. Prior to ignition, the test gas is circulated through external lines and a pump to ensure a homogeneous mixture. Ignition is by an exploding wire which is created by discharging a 2 μF capacitor (initially charged to 9 kV) through a copper wire. The exploding wire initiates a slug of oxygen-acetylene driver gas which is injected into the tube in the vicinity of the wire just prior to ignition. The initiation system is described in greater detail in Akbar (1997). The equivalent energy of the driver gas is calculated to be 70 kJ from the pressure decay of the blast wave in air by the procedure described in Thibault et al. (1987), see the discussion in Akbar et al. (1997).

Three PCB pressure transducers are mounted along the tube and record the detonation pressure and time-of-arrival of the wave which is used to calculate the wave speed. The chemical equilibrium program STANJAN (Reynolds, 1986) is used to calculate the Chapman-Jouguet (CJ) wave speed, pressure, and temperature. The wave speed obtained from the pressure transducers in the main tube is checked against the calculated

CJ value and is typically within ± 2%. In addition, three PCB pressure transducers are mounted in the test section. One of these is at the centerline of the window and may be used to trigger flow visualization.

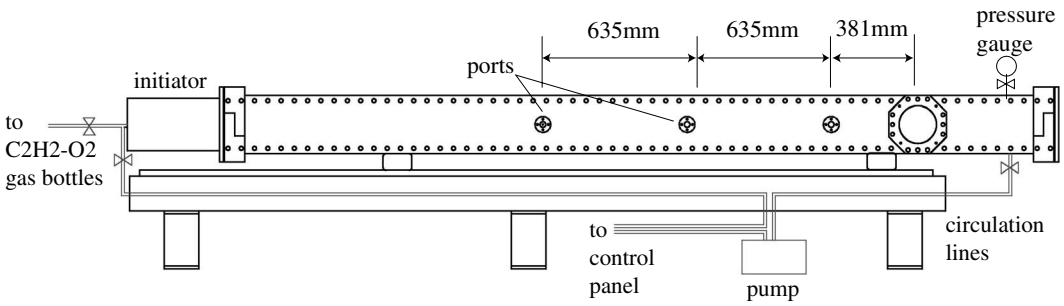

Figure 2.2: Schematic of the NC facility.

The NC facility, shown in Fig. 2.2, is a high aspect ratio (18x152 mm) rectangular channel built for this study. The channel is made of 304 stainless steel. It is 4.2 m long with 184 mm diameter windows approximately 3.6 m downstream of the initiation point. Initially, the entire tube is evacuated to about 40 Pa and then filled with the test gas by the method of partial pressures. Filling lines are evacuated before changing gases to ensure the mixture composition is accurate. Pressure in the tube is measured by an electronic Heise 901a gauge which is accurate to ± 0.17 kPa. Prior to ignition, the test gas is circulated through external lines and a pump to ensure a homogeneous mixture.

Direct and repeatable initiation was a critical issue in this facility. An initiator capable of producing a planar detonation front from the merging of eight smaller wavefronts was used (Jackson and Shepherd, 2002). As part of this study, the initiator was tested and subsequently modified for dynamic injection so that no diaphragm was necessary. An interlocked timing circuit was built to control the injection valves and ignition, and also timing of flow visualization. The narrow channel is filled with test gas then equimolar C_2H_2-O_2 is dynamically injected to fill the initiator channels. After a one second delay, a detonation is initiated in the C_2H_2-O_2. Pressure transducers monitored the planarity of the detonation front at the exit plane of the initiator. A photo of the bottom plate

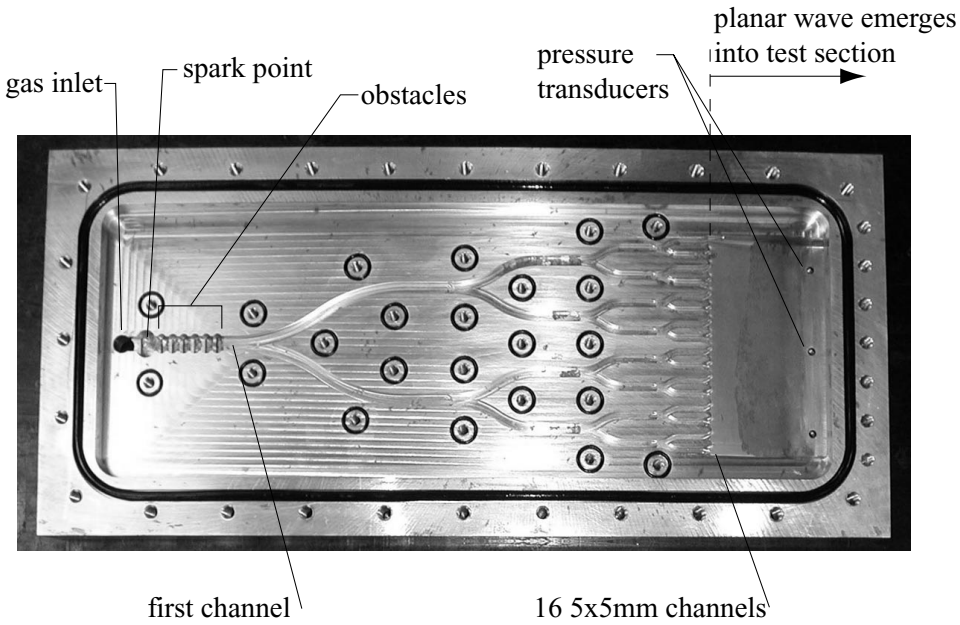

Figure 2.3: Bottom plate of initiator showing channel geometry.

of the initiator is shown in Fig. 2.3. A top plate is bolted to seal the channels. Sample exit plane pressure traces are shown in Fig. 2.4 (a). The initiator transmits a blast wave which directly initiates detonation in the test gas in the channel. A shadowgraph of a blast wave produced by the initiator in air is shown in Fig. 2.4 (b).

Four pressure transducers were flush mounted in ports along the channel to measure detonation pressure and time-of-arrival. From these data, velocity deficits relative to the CJ velocity could be obtained. These data are discussed in Section 3.2. One transducer was located 21.4 mm upstream of the window centerline and was used to trigger the flow visualization.

2.2 Flow visualization

Single-shot schlieren, high-speed shadowgraph movies, chemiluminescence, and PLIF visualization techniques were used. The GDT and NC facilities are located beside one another and can slide on linear bearings in and out of the light paths so they may be

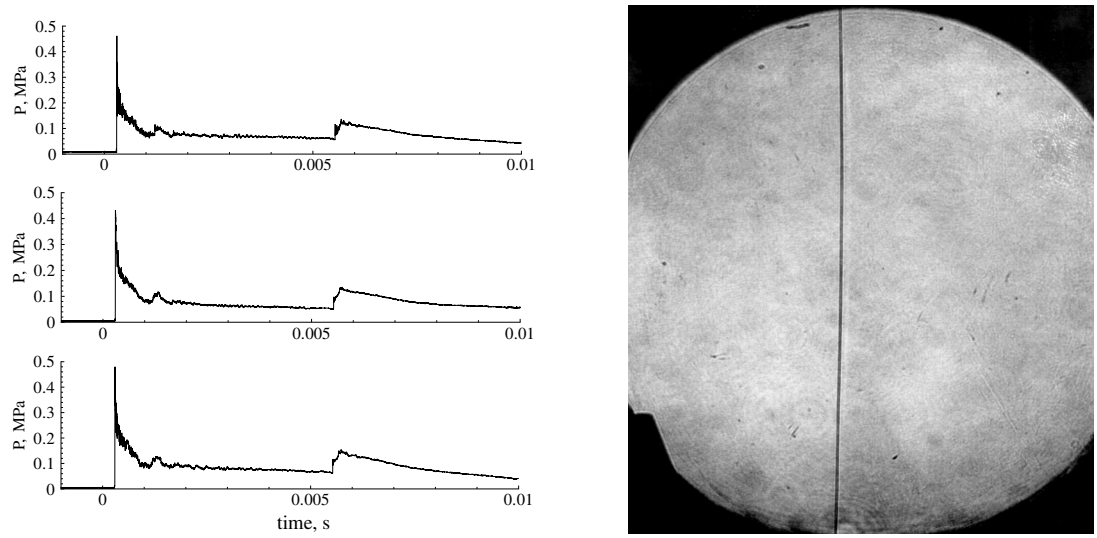

(a) (b)

Figure 2.4: (a) Pressure histories at exit plane of planar initiator. Arrival times of the front are within 2 μs. (b) Blast wave in air, traveling from left to right, produced by initiator. The Mach number at the window location is approximately 1.9. Field of view is about 146 mm.

used interchangeably with just a small adjustment to the image plane. The facilities have the same test section height and used the same windows, one of which is quartz to transmit in the UV. Window frames and glass are flush with interior surface of the facility.

The schlieren system (Akbar, 1997) consists of a Q-switched, flash-lamp pumped ruby laser which creates a short (< 50 ns) light pulse at 693 nm. The light is collimated into a 150 mm diameter beam, passed through the test section, and imaged using a combination of mirrors and lenses on to high-speed instant (Polaroid 3000 ISO) film, Fig. 2.5. The final image size is 72×92 mm. Both vertical and horizontal knife edges were used.

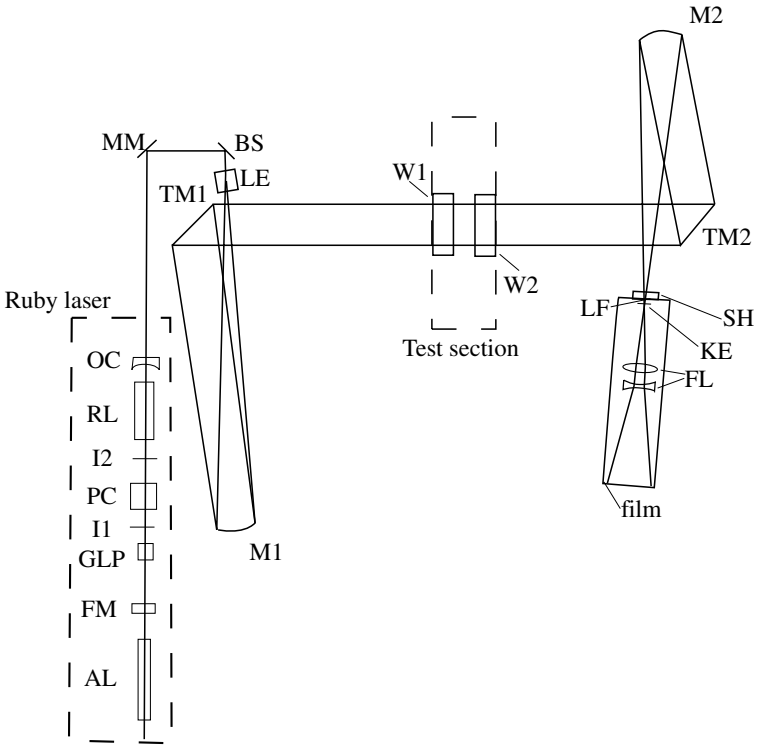

AL	He Ne alignment laser
FM	Rear cavity Mirror
GLP	Glan Laser Polarizing Beam Splitter
I1	Iris
PC	Pockels Cell
I2	Iris
RL	Ruby Rod and Flash Lamp
OC	Output Coupler
MM	Turning mirrors
BS	Bean Steering mirror pair
LE	Beam expander
M	Concave mirrors (f=1.5m)
TM	Turning mirrors
W	Windows
LF	Laser line filter
SH	Capping Shutter
KE	Knife edges
FL	Focusing lenses (f=0.6m, f=-0.5m)

Figure 2.5: Schematic of the ruby laser schlieren setup, based on the setup of Akbar (1997). The alignment laser is used to align the ruby laser cavity, and also the rest of the path. The ruby laser cavity alignment is checked with a test burn. The beam expander is removed (unscrewed) to align along the centerline of the path. Pinholes may be positioned in front of the mirrors. The beam expander is then replaced and the room lights turned off while the expanded beam is aligned. The focus adjustment and knife edge alignment were done assuming the ruby and alignment lasers were coincident.

The OH PLIF system (Pintgen, 2000) is based on an excimer-pumped dye laser. The XeCl excimer laser (Lambda Physik, Model Compex 102) produces a 17 ns pulse of broadband light centered at 308 nm with a total energy of about 300 mJ. The dye laser (Lambda Physik, Model Scanmate 2E) uses Coumarin 153 dye and a frequency doubler to produce narrowband UV light tuned to about 284.008 nm with a total energy of about 3 mJ. The image was aquired by a Princeton ITE/ICCD-576 intensified CCD camera with a 576×384 pixel array through a bandpass filter with a centerline of 313 nm and 10 nm FWHM. Sheet-forming optics were used to create a light sheet that is about 0.3 mm thick at the waist. The light sheet entered the facility through a quartz window in the end plate. The height of the light sheet and the size of the image were varied from 30-80 mm. One PLIF image was obtained per experiment.

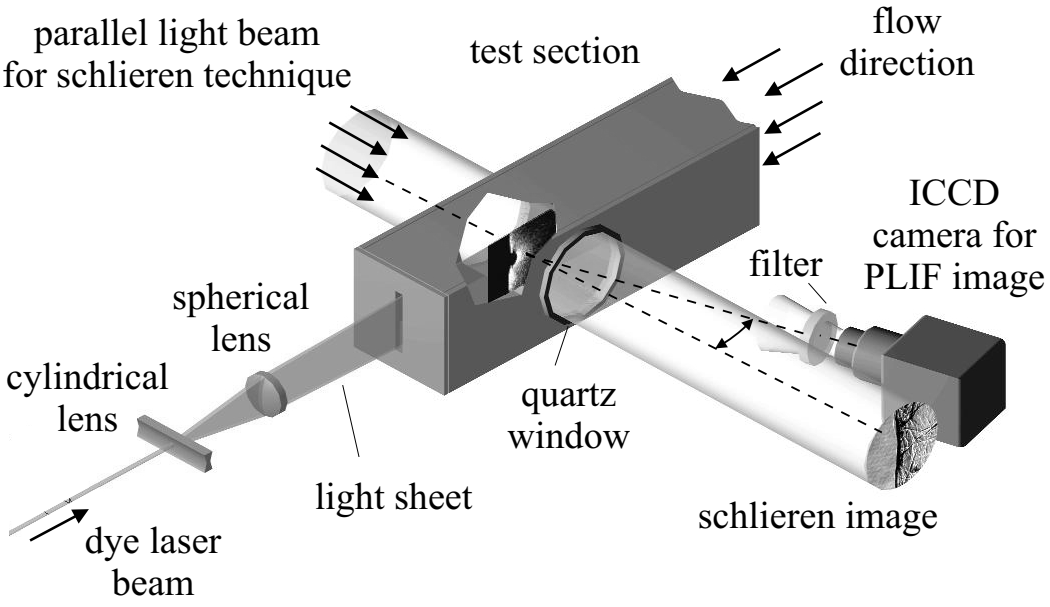

Figure 2.6: Schematic of the experimental setup for acquiring schlieren and PLIF images for a single experiment, from Pintgen et al. (2003). In experiments where only a PLIF image was acquired, the camera is placed exactly perpendicular to the light sheet. The order of the cylindrical and spherical sheet-forming lenses was reversed for the 30 mm images.

In the narrow channel experiments, both schlieren and PLIF images were made of

a single experiment. The setup is shown in Fig. 2.6. Timing between the images was measured using photodiodes to be around 800 ns with the schlieren image taken first. The schlieren image was acquired orthogonally to the flow direction, while the camera for the PLIF image was set at an angle of 16^o to the flow. Postprocessing of a target image, positioned at the test section centerline, was used to superimpose the images and also to correct for distortion.

Chemiluminescence and schlieren images were made using the same setup as the PLIF and schlieren images with a few changes: a 308 nm (10 FWHM) filter was used in front of the ICCD camera, and the gate time of the camera was increased to 200 ns.

Multiple shadowgraph images per experiment may be acquired using a Beckman and Whitley model 189 framing camera (Schultz, 2000). The camera uses high pressure air to drive a rotating mirror at 5000 rpm. 25 images are acquired on Kodak TMAX 400 black and white 35 mm film. Time between frames is 832 ns with a 152 ns exposure time. A linear flashlamp white light source supplies up to 100 J over a 25-100 μs pulse. The optical path is shown in Fig. 2.7. In these experiments, detonation initiation was synched to the location of the rotating mirror by a timing circuit.

2.3 Soot foils

Before the experiment, an aluminum sheet or "foil" may be covered in a light layer of soot and mounted along the facility walls. In the GDT, the foil (0.61 m by 0.91 m by 0.5 mm) is rolled to match the internal diameter of the tube and sooted in a chimney over a burning rag soaked in waste hydrocarbon fuel, such as kerosene. The foil is then riveted to a steel ring on the upstream end of the foil, inserted into the downstream end of the tube and anchored in place at the downstream end of the foil with a bar extended across the tube diameter. In the NC facility, flat soot foils were mounted to the test section wall at the window location to the and anchored at downstream end of the channel. As the detonation propagates over the sooted foil, a cellular pattern is scoured in the soot. The cellular pattern is associated with the instability of the detonation front and the

width of the cells is a measure of the spacing of the transverse waves. To determine an average length scale, about 10 cell width measurements are made on each foil from which a minimum, a maximum, and an average cell width are recorded. To give an indication of the range of cell widths recorded for each experiment, the minimum and maximum cell widths are presented in the form of "error bars" about the average value. Two factors contribute to the cell width range. Cell width measurements are subject to variation from observer to observer. These can be on the order of $\pm$ 50% (Tieszen et al., 1991). To minimize this, all present data were measured by one observer. There can be a spectrum of cell widths recorded for a particular mixture due to the inherent irregularity of the cells, as discussed in Section 1.2.1.

2.3.1 Soot transport by detonation

Using stroboscopic schlieren through a sooted window, Urtiew and Oppenheim (1966) showed the cellular tracks are associated with the triple points in the front, but the precise mechanism by which the tracks are formed is unknown. High pressure, vorticity, and soot combustion have all been suggested as possible mechanisms. Pintgen and Shepherd (2003) have used PLIF images of the front overlaid on soot foils to study this process and find that the soot tracks are nearly coincident to the triple point, but a systematic displacement is observed. Recent work by Inaba et al. (2002) suggests that directional differences in the shear stress are responsible for transport of the soot. As a contribution to this work, a study of the transport of soot by detonation was carried out. Soot foils were partially sooted along striped sections in different directions. Partial sooting was achieved very simply by covering regions of the foils with scotch tape before sooting and then removing the tape. Samples are shown in Fig. 2.8. The transport of soot is observed to depend on the local lead shock configuration. Soot appears to be accumulated on the side of the track with the stronger lead shock (Mach stem, see Section 4.1.1).

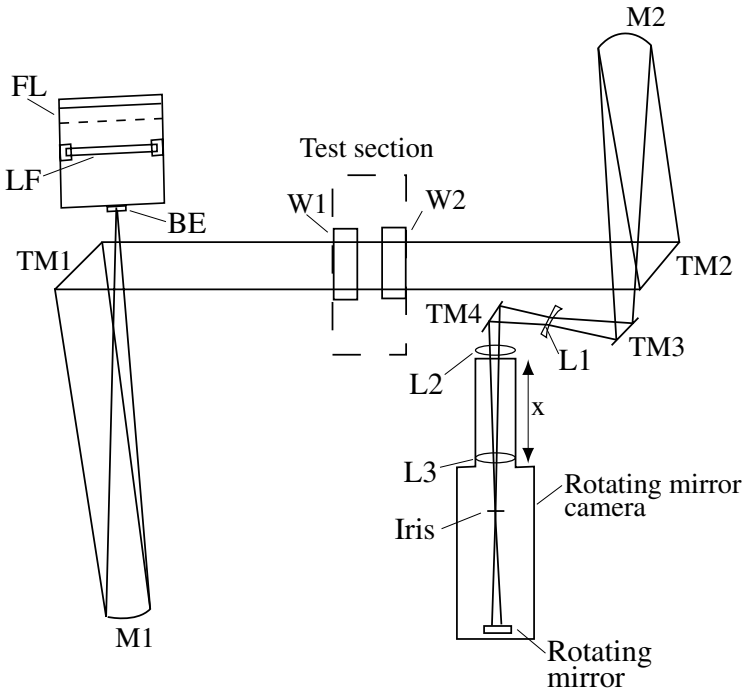

FL	Fresnel lens
LF	Linear flashlamp
BE	Beam expander
M	Concave mirrors (f=1.5m)
TM	Turning mirrors
W	Windows
L1	lens (f= -350mm)
L2	lens (f= 750mm), acromat
L3	Internal objective lens

from M2 to L1 =1270mm
from L1 to L2 = 315mm
x (camera extension) = 300mm

Figure 2.7: Schematic of the framing camera light path, based on the setup of Schultz (2000). The path is a modification of the ruby laser setup, Fig. 2.5. The beam steering mirror pair is replaced by the box containing a linear flashlamp and fresnel lens. A beam expander is located at the focus of the first concave mirror, M1. Its purpose is to prevent the linear flashlamp being imaged as a horizontal line. An alternative is to use an iris to cut out only a small fraction of the light. The optical path is aligned by positioning a He-Ne alignment laser in place of the flashlamp box. The beam expander may be removed to first align the centerline of the path. The focus and image size at the camera are adjusted using lenses L1 and L2 and the extension, x which controls the position of the internal camera lens. The focus is checked by positioning a piece of exposed film at the field-flattening lenses of the camera and using an magnifying eyeglass to view a target located at the test section centerline. Screens were used along the path to obstruct indirect light from the detonation.

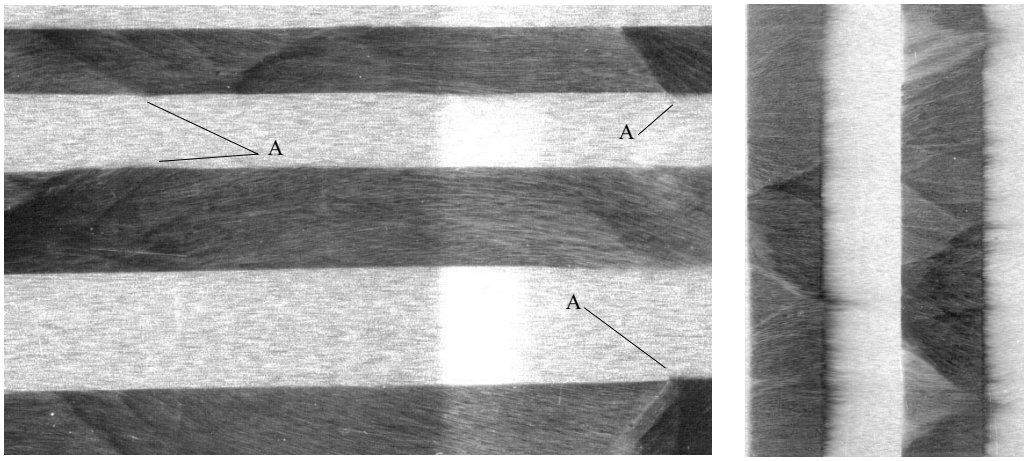

(a) (b)

Figure 2.8: Partially sooted foils after passage of detonation from left to right. Detonation propagated left to right in CH_2-O_2-0.2Air (Shot gdt1527). (a) Soot is transported transversely in locations marked A, which appear to correspond to Mach stem portions of the front. Image height is 43 mm. (b) Periodic variation in location of transported soot. Darker regions correspond to the Mach stem portions of the front. Image height is 106 mm.

Chapter 3 The Effect of Confinement Geometry

The cellular structure of a detonation wave is three-dimensional and dependent on the confining geometry since the transverse waves are reflected from the walls of the facility as well as from each other. In a round tube, the transverse waves will propagate in circumferential and radial directions (Voitsekhovskii et al., 1963). In a rectangular channel, the propagation direction of transverse waves will ideally be in two planes orthogonal to one another and to the tube walls (Strehlow, 1969). The three-dimensional complexity of the front creates difficulties for visualization techniques that integrate through the flowfield. To overcome this, the instability may be weakened or suppressed in one plane in a facility in which at least one dimension is on the order of the detonation cell width. This was the concept behind the construction of the narrow channel facility. Initially, the possibility of using a porous wall to suppress the out-of-plane instability was considered and tested in the GDT using a secondary cookie-cutter, as described in Section 3.1. Solid wall experiments were also conducted and the results were used to determine the dimensions of the NC facility to suppress the out-of-plane instability over an appropriate length scale range. It must be noted that, as discussed in Strehlow and Crooker (1974), detonations in a narrow channel differ from ordinary detonations, in particular, the track angle and the calculated transverse wave strength is increased. To explore the generality of our results, two facilities of different geometry were used in this study.

3.1 Transverse wave damping

The possibility of weakening or suppressing out-of-plane transverse waves by reflection from a porous surface was explored. To first study the feasibility of this idea, numerical

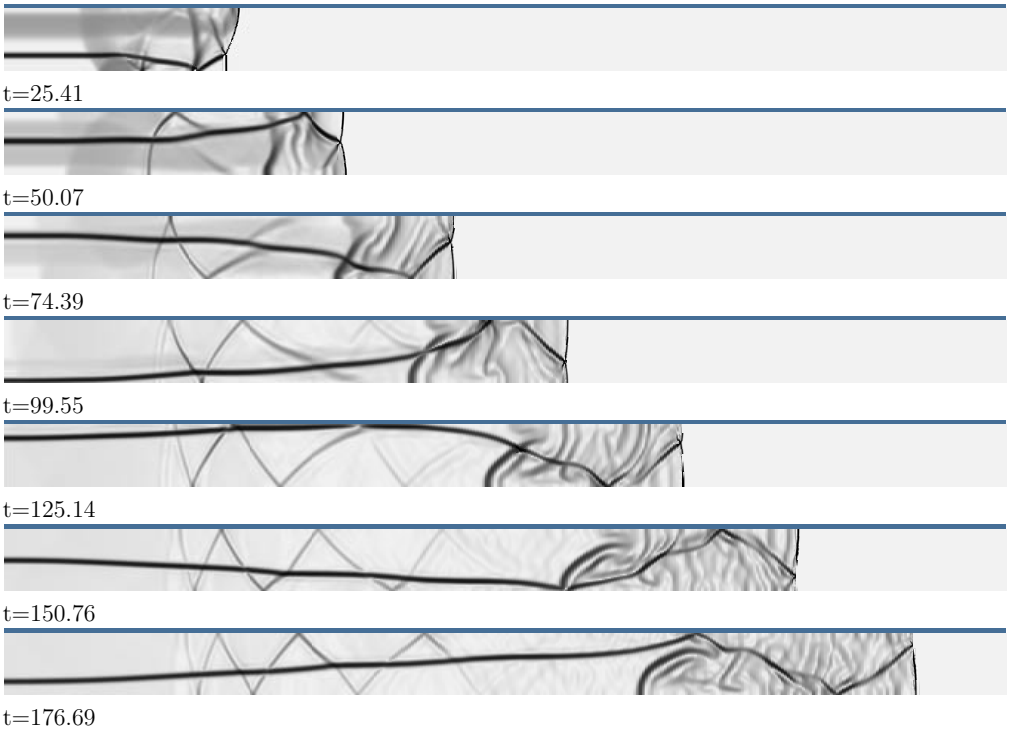

Figure 3.1: Numerical simulation of transverse shock wave reflection from solid surface. Simulation performed by Prof. Hans Hornung using AMRITA (Quirk, 1998) with initial Mach number of 2 and wave angle of 20^o. The simulation is unreactive, with γ=1.4.

[1] simulations of the reflection of nonreacting Mach stem from a solid (Fig. 3.1) and porous wall (Fig. 3.2) were performed by Prof. Hornung of GALCIT. Parameters such as the length of the porous section L and the width g and depth l of the porous holes relative to the channel dimension w were varied to optimize the attenuation of the transverse waves while introducing minimal flow disturbances. Hole parameters over the range $0.05 \leq l/h \leq 0.5$ and $3 \leq l/g \leq 10$ were studied and optimal dimensions were found to be l/w=0.25 and l/g=5, see Table 3.1. These dimensions were then used as a basis for an experimental study. In the experiments, l/g was 3.5 and 5.8 as the range of hole diameters available in porous sheeting was limited.

The 280 mm diameter gaseous detonation tube described in Section 2.1 was modified for this study with the addition of a second "cookie-cutter" in the test section, as shown

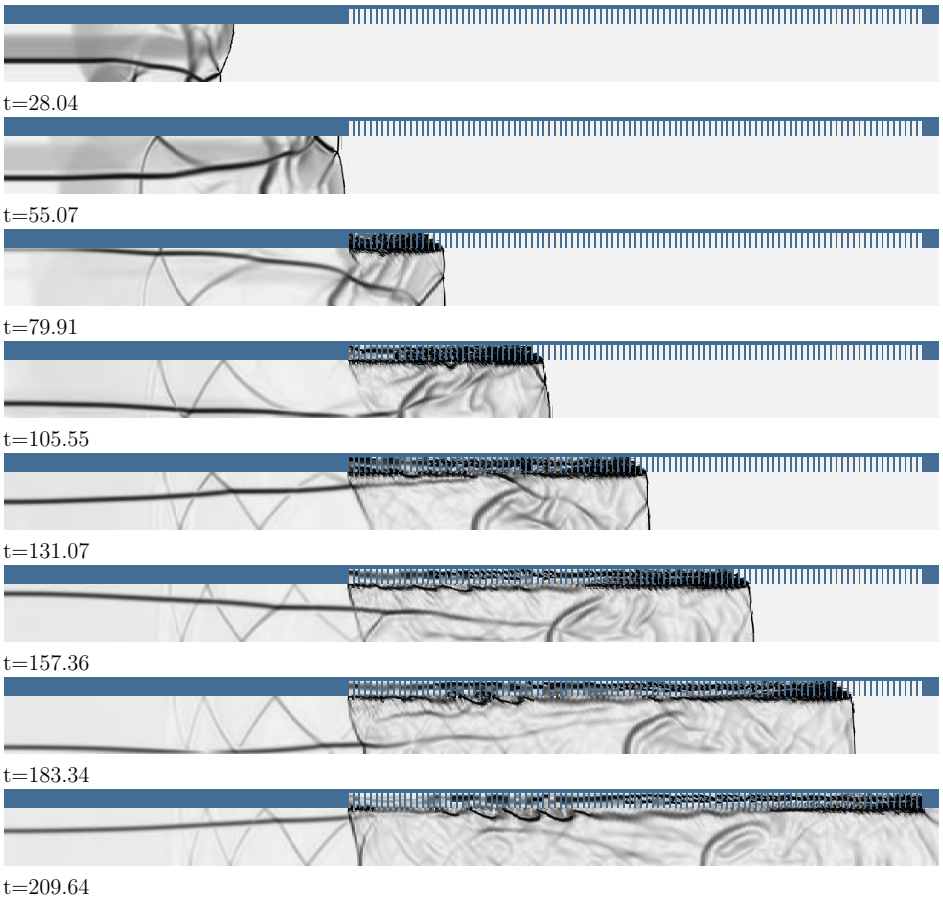

Figure 3.2: Numerical simulation of transverse shock wave reflection from porous surface. Simulation performed using AMRITA (Quirk, 1998) with initial Mach number of 2 and wave angle of 20^o. The simulation is unreactive, with γ=1.4. Holes have an aspect ratio of 5 and a depth 1/4 of the channel dimension. The length of porous section is 10 times the channel dimension.

Wall section type	Depth, mm	Length, mm
Non-porous	-	-
Porous	4.5±0.5	180
Porous	4.5±0.5	300
Porous	7.5±0.5	180

Table 3.1: Porous wall section configurations.

in Fig. 3.3. The second cookie-cutter was attached to the end flange of the facility with a gap left at the downstream end so that the gas could be circulated and mixed. A 127×300 mm portion of the channel wall of the second cookie-cutter was interchangeable and could be used to mount either solid or porous wall sections. The step at the transition between sections was less than ± 0.5 mm. The porous section was composed of perforated brass sheets 450 μm thick (26 gauge) that were layered with the holes aligned. The layers were compressed together and a final solid sheet was added so that the porous section is composed of blind holes 1.3 mm in diameter with 45% porosity and has variable depth. A summary of facility configurations that were tested is shown in Table 3.1. Stoichiometric H_2-O_2 with Ar or N_2 dilution and initial pressures varying from 10-30 kPa were studied in the porous experiments. Pressure transducers were used to determine the wave speed, and soot foils were mounted along the facility walls in both planes to record the effect of the porous wall on the cellular structure. Along surface A, the soot foils were made from aluminum sheets which were fixed at the sides and glued to the leading edge of the second cookie-cutter for each experiment. Soot foils along surface B were Mylar sheets that were scotch-taped on all four sides to the side walls of the channel. Relatively modest attachment techniques may be used if care is taken to ensure the flow does not get under the foil.

Experiments with a solid wall section are discussed first. Soot foils were mounted along surface A in Fig. 3.3 upstream and downstream of the interchangeable section. Soot tracks from weakly unstable (Ar-diluted) detonations are shown in Fig. 3.4. A change in the cellular structure can be seen along the channel as the detonation adjusts to the change in the channel geometry. Two planes of detonation structure can be seen on

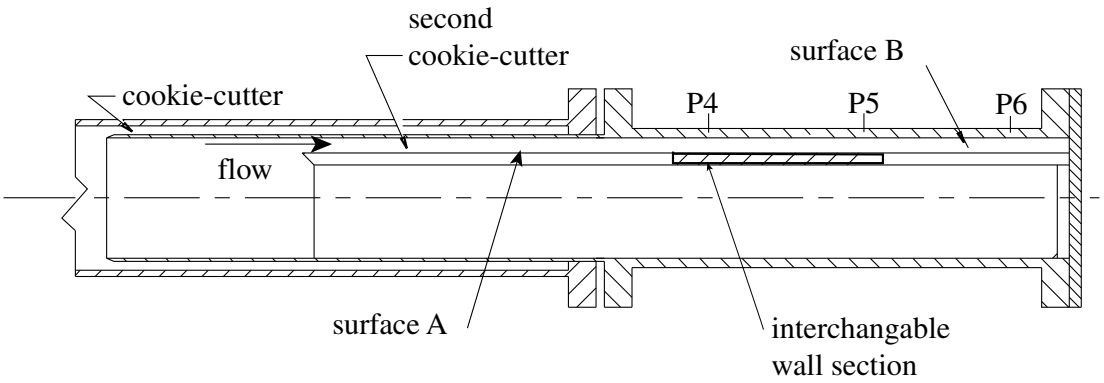

Figure 3.3: Schematic of downstream portion of the gaseous detonation tube modified with second cookie cutter. The channel height was 127 mm and three different channel widths were studied: 8 mm, 18 mm, and 30 mm. The 127×300 mm interchangeable wall section is shown. Soot foils were mounted along surface A, upstream and downstream of the interchangeable section, and along surface B. Three pressure transducers were located in the 280 mm tube (see Fig. 2.1) and three additional transducers (P4 at x=4.83 m, P5 at x=5.04 m, P6 at x=5.26 m where x=0 is the ignition location) were located along the top wall of the test section, as shown.

the downstream foil when the structure has adjusted to the rectangular channel geometry: tracks due to waves propagating parallel to the foil appear as a diamond-shaped cellular pattern and tracks due to waves propagating orthogonally to the foil (in the out-of-plane direction) appear as lines and are commonly called "slapping" waves. It can also be observed that in Fig 3.5 (a) and (b) the cell width increases further downstream, as reported by Strehlow and Crooker (1974). It should be noted that in these cases, when the initial cell width is comparable to the channel dimension, the cell width of the detonation is no longer an intrinsic length scale but depends on the facility dimension.

Sample results for the effect of the porous wall on weakly unstable detonation are shown in Fig. 3.5. Case (a) shows both planes of the detonation apparently unaffected. In case (b) damping of the out-of-plane waves is observed (lines due to the out-of-plane slapping waves are not observed downstream of the porous section). The in-plane structure is also affected with the cell width increases by 50% from 6 mm to 9 mm over the porous wall. Without the porous wall (Fig. 3.4 (a)), the cell width increases 20% in this distance. Further downstream, the out-of-plane structure reappears. In case (c), the initial pressure is decreased resulting in an increase in the cell width but no change in the regularity of the mixture. In this case, the structure in both planes appears significantly disturbed downstream of the porous wall. Further increase of the cell width by dilution, case (d), results in failure after the porous section, followed by reinitiation. The soot foils shown above are oriented in the plane of the porous wall. Soot foils could also be mounted along the side walls (surface B), as shown in Fig. 3.6 for the mixture of case (a). The tracks can be seen to weaken significantly as the detonation propagates over the porous wall. A summary of the behavior for the 50% dilution case is presented in Table 3.2. For the limited range of parameters studied, damping of the transverse waves in one plane is found to be effective for $w/d = 1.7$, where w is the channel width and d is the hole depth, for λ=6 mm. If the damping was not effective, increasing the length of the porous section by a factor of 1.7 does not make it so.

Velocity deficits $\delta U=(U_{meas}\text{-}U_{CJ})/U_{CJ}$ as a function of downstream distance for weakly unstable detonations with increasing argon dilution are shown in Fig. 3.7. The transient

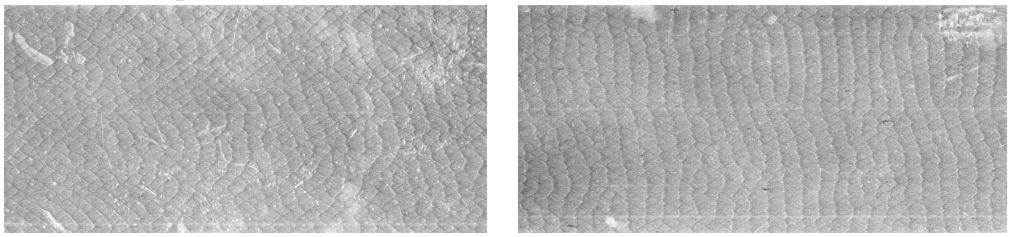

(a) $2H_2$-O_2-3Ar, P_1=30 kPa, λ=5 mm, Shot gdt1354.

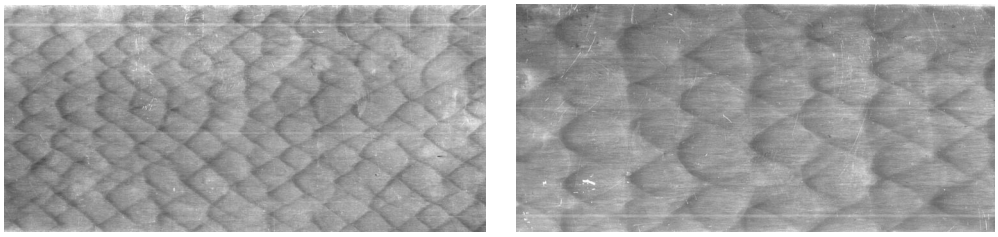

(b) $2H_2$-O_2-12Ar, P_1=30 kPa, λ=14 mm, Shot gdt1355.

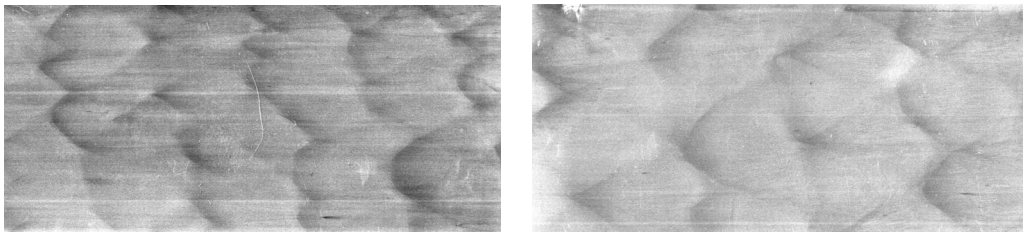

(c) $2H_2$-O_2-17Ar, P_1=30 kPa, λ=28 mm, Shot gdt1356.

Figure 3.4: Soot foils from weakly unstable detonations in the 127×18 mm channel. Image height is 127 mm. Soot foils were located upstream and downstream of the interchangeable wall, which in these experiments contained a solid section. λ is the average cell width measured on the upstream foil.

Channel width	Porous section length	Hole depth	Out-of-plane damping
18	180	4.5 ± 0.5	yes
30	180	4.5 ± 0.5	no
30	300	4.5 ± 0.5	no
30	180	4.5 ± 0.5	yes

Table 3.2: Summary of results for detonation in $2H_2$-O_2-3Ar, P_1=30 kPa, λ=6 mm.

due to the change in channel geometry can be clearly observed. For the case with 50% dilution ($2H_2$-O_2-3Ar), an additional velocity deficit of about 1% is due to the porous wall. For increased dilution, soot foils show the detonation fails after the porous wall section and then reinitiates. Failure, followed by re-initiation, is observed when $\lambda/w \geq 0.6$, where w is the channel width, for Ar-diluted mixtures and when $\lambda/w \geq 0.8$ for more irregular, N_2 diluted mixtures. Failure is not observed in these mixtures in the case of a solid wall.

From these results, it was concluded that the use of a porous wall in damping the out-of-plane waves could not be done over a range of mixtures without significantly affecting the in-plane structure. Instead, experiments with a solid wall showed a channel that was 18 mm in dimension would weaken the out-of-plane structure over an appropriate range of length scales.

Experiments were also performed on a highly unstable detonation front in CH_4-$2O_2$-0.2Air, P_1=80 torr, the same mixture as used by Subbotin (1975). A soot foil, shown in Fig. 3.8, was now located the entire distance along surface A, and there was no porous wall. Dramatic transients and changes in the cellular structure may be observed. The cell width increases until only two transverse waves are present. The detonation decouples at corners of the channel (at the edges of the foil) and a re-initiation process is observed. As can be seen from the soot foils in Appendix A, this case is not typical of the detonations studied in the rest of this work.

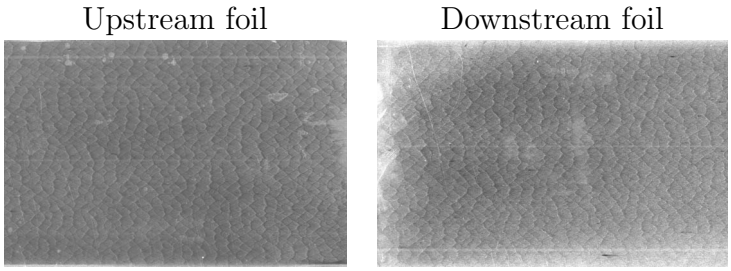

(a) $2H_2$-O_2-Ar, P_1=30 kPa, λ=5 mm, Shot gdt1475.

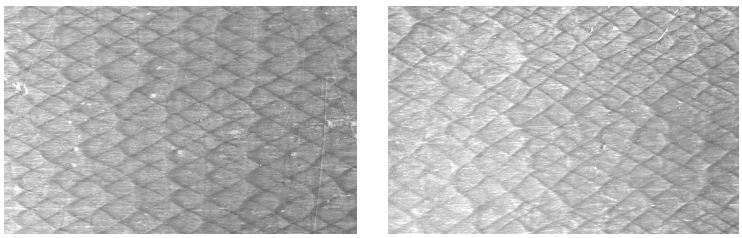

(b) $2H_2$-O_2-3Ar, P_1=30 kPa, λ=6 mm, Shot gdt1471.

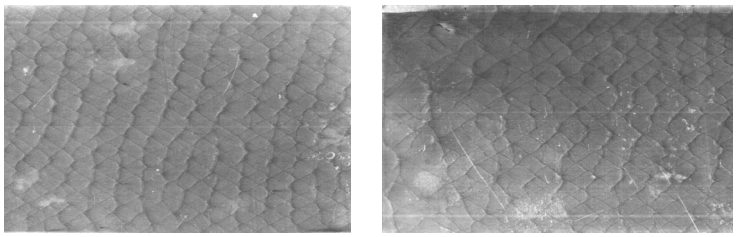

(c) $2H_2$-O_2-3Ar, P_1=20 kPa, λ=9 mm, Shot gdt1476.

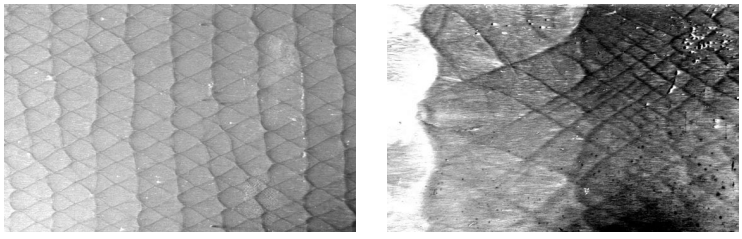

(d) $2H_2$-O_2-8Ar, P_1=30 kPa, λ=11 mm, Shot gdt1472.

Figure 3.5: Soot foils from weakly unstable detonations in the 127×18 mm channel. Soot foils were located upstream and downstream of the interchangeable wall, which in these experiments contained a porous section 4.5 mm deep and 180 mm long. λ is the average cell width measured on the upstream foil.

Figure 3.6: Soot foil (Shot gdt1494) located along the side wall of the facility (surface B in Fig. 3.3). Channel (and soot foil) width is 18 mm. Vertical lines show the location of the porous wall, oriented orthogonally to the foil along surface A.

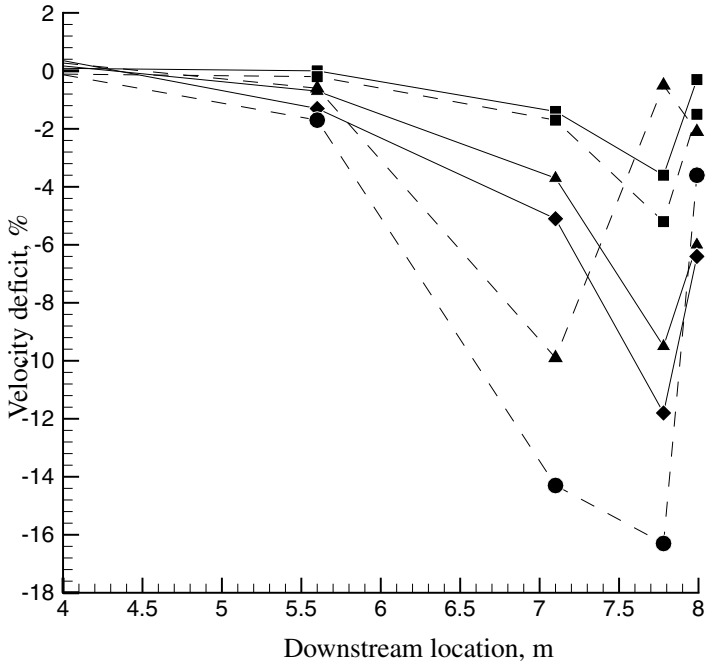

Figure 3.7: Velocity deficits as a function of distance along the facility consisting of three different cross-sectional geometries. From x=0 to x=6.59 m, the detonation propagates through a 280 mm diameter tube, from x=6.59 to x=6.89 a cookie cutter reduces the channel dimension to 150×150 mm square, then from x=6.89 to the end of the facility, the second cookie cutter reduces the channel dimensions again to a 127 mm channel with variable width. In these experiments the channel width was 18 mm. Solid lines correspond to solid walls along the second cookie-cutter; dashed lines correspond to the porous wall. Squares: $2H_2$-O_2-3Ar, Circles: $2H_2$-O_2-8Ar, Triangles: $2H_2$-O_2-12Ar, Diamonds: $2H_2$-O_2-17Ar

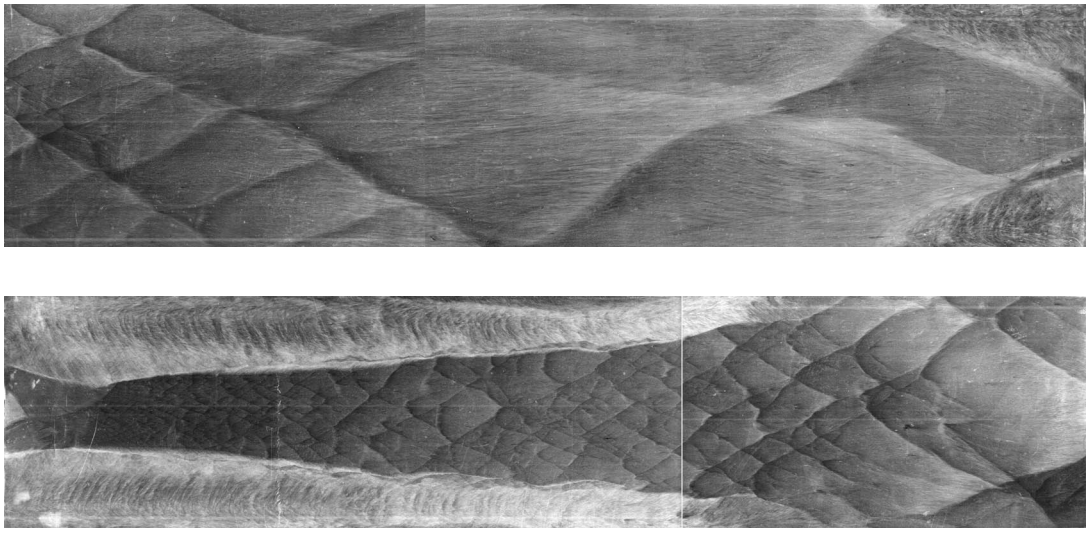

Figure 3.8: Soot foil from highly unstable, CH_4-$2O_2$-0.2Air detonation propagating from left to right in the 127×18 mm channel (Shot gdt1526). Foil is shown in two sections for convenience.

3.2 Boundary layers

The influence of viscous effects on the detonation in the narrow channel are considered. No exact calculations or direct measurements are available for the boundary layer in a detonation wave although Liu et al. (1983) developed a solution for a laminar boundary layer in the Taylor expansion wave following a detonation. Navier-Stokes codes are rarely used in studies of detonation waves. A few empirical models or empirical relations have been proposed, most often based on velocity or pressure data.

Fay (1959) proposed that the influence of the boundary layer on a detonation wave occurs only upstream of the sonic plane. This idea is supported by the fact that mixtures with a larger cell width, which is proportional to the reaction zone length, with respect to the channel dimension are observed to have a significant velocity deficit. Fay modeled the displacement effect of the boundary layer as a uniform flow divergence in the reaction zone over the entire front. He applied an empirical correlation developed for turbulent boundary layers behind shock waves (Gooderum, 1958) and compared predicted and measured velocity deficits δU, where $\delta U = (U - U_{CJ})/U_{CJ}$. Predictions agree to within 30% with measured values for highly diluted H_2-O_2-Ar, C_2H_2-O_2-Ar detonations. Agreement is only to within a factor of 2 for C_2H_2-Air detonations.

A difficulty with theories such as Fay's that are based on a steady, one-dimensional description of a detonation is the inability to account for the experimental observation that mixture regularity has an influence on the velocity deficit. Moen et al. (1986) and Murray (1985) report that for a given cell width and channel dimension, a mixture with a regular cellular structure has a significantly larger velocity deficit than an irregular mixture. Wolanski et al. (1981) report a velocity deficit of only 1.5% for a mixture with highly irregular structure (CH_4-Air) propagating in a 63 mm diameter tube which is four times smaller than the cell size (Tieszen et al., 1991).

Strehlow and Salm (1976) used a pressure history measured in their 6.4 mm wide channel to fit Schlichting's turbulent boundary layer relation to obtain a boundary layer thickness. They calculate that the boundary layer fills the channel 83 mm downstream

of the shock location. Only one mixture was used in the study, $2H_2$-O_2-3Ar, P_1 =12 kPa, which has a cell width of 60 mm. We are not aware of any other studies of the boundary layer thickness in detonations. In present work, we are interested in the leading shock and reaction front rather than the downstream behavior, so the boundary layer growth behind a strong shock may be used as a reasonable estimate. Such a calculation was carried out by Pintgen and Shepherd (2003) who found the boundary layer thickness to be less than 1 mm at the end of the induction zone. In view of this, the effect of the boundary layer is taken to be negligible in visualizations of the region of interest in this study.

However, velocity data may be used to gauge if the detonation is a fully developed and self-sustaining wave. Sample velocity data from the narrow channel experiments are shown in Fig. 3.2. Results for weakly unstable detonation with increasing argon dilution are shown in Fig. 3.2 (a). The velocity deficit increases with increasing Ar-dilution. For mixtures that are not classified as "marginal" for the purposes of this study, velocity deficits are less than 8%. N_2-diluted stoichiometric H_2-O_2 mixtures are shown in Fig. 3.2 (b). As reported by Moen et al. (1986), velocity deficits in these mixtures are less than in the Ar-diluted mixtures. For non-marginal waves, deficits are less than 5%. Also shown is an example of a highly unstable mixture, C_3H_8-$5O_2$-60%N_2. Deficits in these mixtures are less than 3%. Unless reported otherwise, detonations in this study are steady to within $\pm$ 3% by the window location.

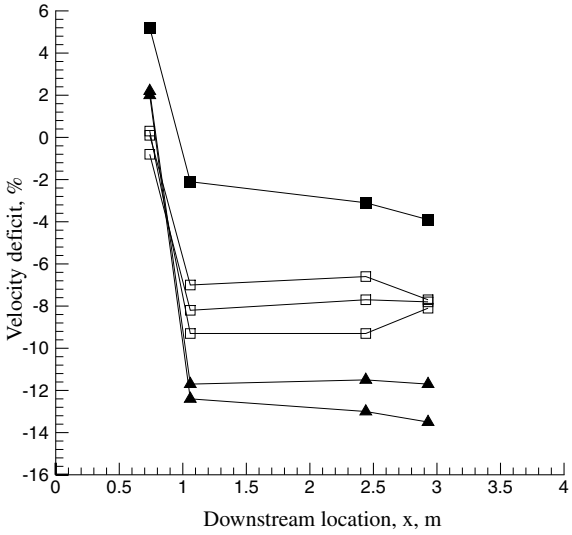

(a)

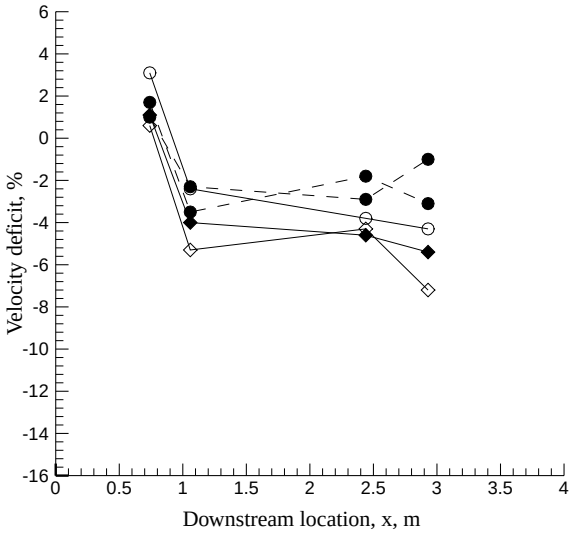

(b)

Figure 3.9: Velocity deficit as a function of distance downstream of the initiator exit (x=0) in the narrow channel, where x is the center of two time-of-arrival transducers. (a) $2H_2$-O_2 -7Ar (filled squares) -12Ar (squares), -17Ar (triangles). (b) $2H_2$-O_2 -3.5N_2 (filled diamonds), -4.5N_2 (open diamonds), -5.6N_2 (open circles) and C_3H_8-5O_2-9N_2 (filled circles).

Chapter 4 Weakly Unstable Detonation

In Fig. 1.6, we identify the category of weakly unstable detonations as mixtures with stability parameters close to the longitudinal neutral stability curve ($\theta \sim 5$, $Q \sim$ 10-30). In particular, this category includes detonation in $2H_2$-O_2 with more than about 50% Ar dilution, mixtures which are commonly called regular (Strehlow, 1969). The effect of the chemistry is in a sense decreased in these mixtures as the chemical energy release and activation energy are reduced. Ar-diluted mixtures have been extensively studied by previous researchers using schlieren and interferometry. As discussed in more detail below, these studies resulted in an understanding of the spatial and temporal oscillations of the lead shock and periodically-colliding transverse waves. Outstanding issues include the details of the shock configurations and the role of the transverse waves.

4.1 Transverse waves and triple point structure

The role of the transverse waves in detonation propagation has been investigated experimentally, theoretically, and numerically by numerous researchers. Progress has been made towards determining the triple point structure at different locations through the cell for varying geometries, mixtures, and initial pressures, but there is no comprehensive theory that explains the observed behavior.

Because of the difficulties associated with studying the full three-dimensional structure of detonation, most experimental visualizations and numerical simulations have concentrated on detonations with a simplified structure. The structure of the single-spin detonation has been studied extensively (Voitsekhovskii et al., 1963, Schott, 1965, Huang et al., 2000). It is generally agreed that these waves have a complex transverse wave structure involving more than one triple point, where the segment of the transverse wave in the immediate vicinity of the primary triple point is unreactive, while the sec-

tion downstream of a second triple point is an overdriven detonation (an example of the so-called "strong" triple point configuration, see Figure 4.1).

An alternate experimental geometry for studying reduced detonation structure is a narrow rectangular channel. Voitsekhovskii et al. (1963), Nagaishi et al. (1971), Edwards et al. (1972), Strehlow and Crooker (1974), Subbotin (1975), and Solouhkin have all exploited this geometry to create more nearly two-dimensional waves. Their work resulted in an understanding of the spatial oscillations of the leading shock front and periodic collision of triple points forming the cell cycle. Voitsekhovskii et al. (1963) describe a complex transverse wave structure similar to that obtained in the case of single spin. Triple point configurations with strong shear layers are evident in interferograms obtained by Edwards et al. (1972) in a narrow channel in $2H_2$-O_2-4.5Ar. As discussed in Strehlow and Crooker (1974), detonations in a narrow channel differ from ordinary detonations in several ways, in particular, the track angle and the calculated transverse wave strength is increased.

Two general classes of triple point structure have been suggested: "weak" configurations that involve a single triple point with nonreactive waves, and "strong" configurations that involve a second triple point, generally with some portion of the transverse wave becoming reactive. Many variations of these configurations have been reported.

There is some evidence that the triple point structure is unsteady and evolves through the cell. Lefebvre and Oran (1995) perform two-dimensional numerical simulations in which they examine the structure of the triple point in $2H_2$-O_2-7Ar at 6.67 kPa. The configuration found near the apex of the cell involves only a single triple point and a tranverse wave nearly orthogonal to the incident shock. As the incident wave progresses through the cell a second triple point develops and the transverse wave becomes reactive. Strehlow and Crooker also came to the same conclusion by examining soot foil tracks in a narrow channel and report the structure evolves from a simple (or "weak") structure involving only a single triple point near $x - x_o = 0.5L$ to a more complex structure involving a reactive transverse wave downstream of a second triple point. In contrast, Urtiew (1976) proposed the triple point configuration rotates as the leading wave moves

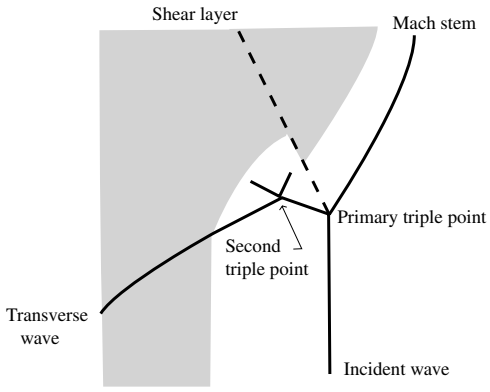

Figure 4.1: Cartoon to illustrate the nomenclature associated with the triple point. Two triple points are shown: a primary triple point at the intersection of the Mach stem and incident wave, and a secondary triple point downstream of the main front. The flow downstream of the second triple point is shown here as unreactive, but numerical studies and experiemental schlieren images describe a closely coupled reaction zone with this portion of the transverse wave, the so-called "strong" triple point configuration. A "weak" configuration generally omits the second triple point.

through the cell in such a way that both the track angle and the transverse wave strength may be approximated as constant.

The present experiments build on the previous work and address some of the questions mentioned above. Schlieren images of weakly unstable detonation fronts in the narrow channel are shown in Fig. 4.2. The shock configurations are very similar to those observed by previous researchers (Section 1.1) and shown schematically in Fig. 1.2. The spatially oscillating leading shock, triple points, transverse waves, and shear layers can all be clearly identified.

Resolved images of chemical species in the reaction front were made for the first time by Pintgen (2000) using PLIF to detect the OH radical. Fig. 4.3 shows an image from that work in a Ar-diluted H_2-O_2 mixture. A distinct front is seen due to the rapid increase on OH mole fraction that results from chain-branching reactions (Fig. 1.4). Distinctive "keystone" features, which correspond to spatial oscillations in the lead shock, were observed in this work and are analyzed in Section 4.1.1. This analysis is the present author's contribution to Pintgen et al. (2003).

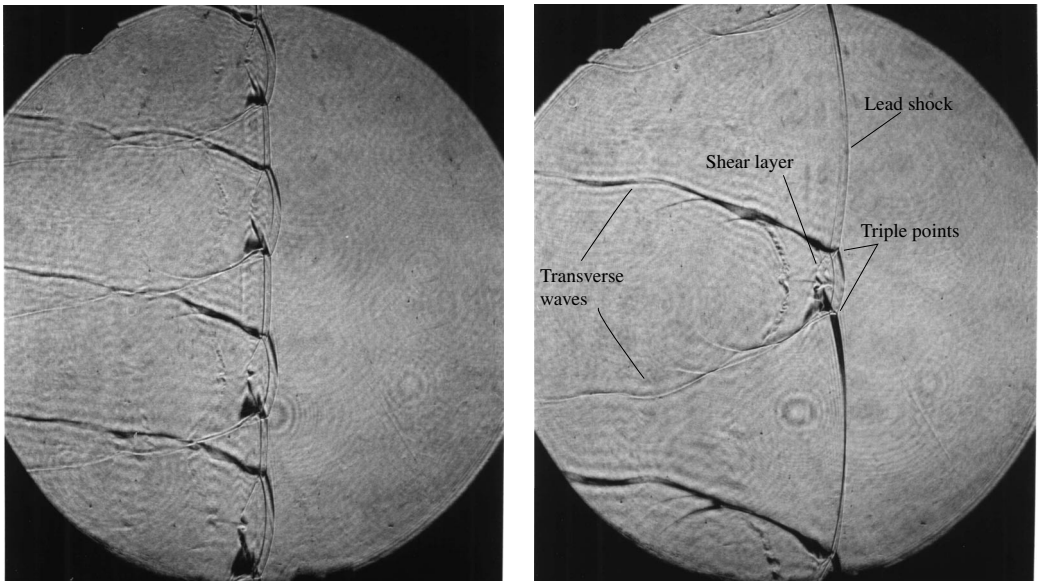

(a) (b)

Figure 4.2: Schlieren images of detonation in (a) $2H_2$-O_2-12Ar, P_1=20kPa (Shot nc77) (b) $2H_2$-O_2-17Ar, P_1=20kPa (Shot nc81). The field of view is about 146 mm. Detonation is propagating from left to right in the narrow channel facility.

4.1.1 Keystones

The induction time is known to be a strong function of the lead shock strength and the sudden changes in the location of the reaction front are linked to spatial oscillations in the lead shock which result from the instability of the detonation. As observed in Fig 4.2, triple points occur at the junction of the transverse wave and lead shock, linking portions of the lead shock of alternating strength. The local triple point structure is analyzed using gas dynamics and zero-dimensional chemical species calculations to explain the keystone features apparent in PLIF images from Pintgen (2000).

Shock and detonation polar calculations (Appendix B) are carried out to analyze the triple point configurations. This technique has been used previously by several researchers: Oppenheim et al. (1968), Urtiew (1970), Barthel (1972), Subbotin (1975). The shock polar is calculated using the oblique shock jump relations and assumes a perfect gas, with the ratio of specific heats taken to be that of the reactants, γ_1. The deto-

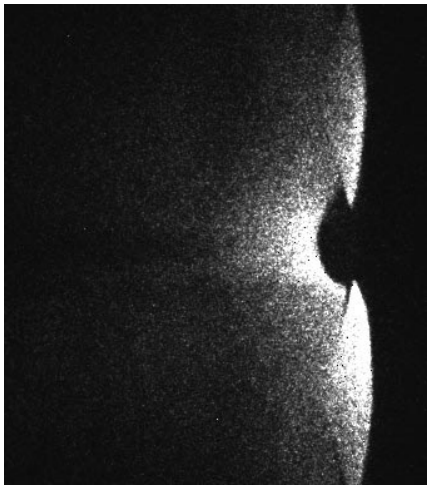

Figure 4.3: OH fluorescence image of reaction zone structure in $2H_2$-O_2-17Ar, P_1=20 kPa, taken from Pintgen (2000) (Shot gdt1419). Image height is 80 mm. Detonation is propagating left to right.

nation polar (Shepherd, 1994) is a locus of solutions possible for an oblique detonation which is overdriven at shock angles greater than that corresponding to the CJ wave. A two-gamma model (see Appendix B) is used to model the variation in thermodynamic properties between the reactants and products. The analysis assumes the flow is quasi-steady in the frame of the triple point and the waves are straight in the vicinity of the triple point, see Fig. 4.4. This assumption is more valid for a nonreactive flow than reactive, and a probable effect of the chemistry will be to produce some wave curvature in the vicinity of the triple point.

The incident shock Mach number at each location was estimated from the calculated centerline pressure profile from Eckett (2000) and the incident flow angle was taken to be 57° (corresponding to a track angle, ϕ, of 33°). This value is representative of track angles recorded on soot foils mounted on the side walls of the test section. Given the incident wave Mach number and the track angle, the triple point configuration can be solved by matching the pressure and flow deflection angle, θ, across the slip stream. The shock and detonation polars are therefore conveniently displayed on a pressure-deflection (P-θ) plot. An example of such a calculation together with the resulting triple point configuration for

a stoichiometric H_2-O_2 mixture with 70% Ar dilution at 6.67 kPa initial pressure is shown in Fig. 4.4 (a). Note that as there is no intersection of the detonation and transverse wave polars, there is no solution possible which involves a reactive Mach stem, i.e., the existence of an induction zone, however small, is crucial for obtaining a solution. For this and all other mixtures considered in this study, a solution consisting of a single triple point which involved the detonation polar for the leading wave was not possible; thus, the Mach stem is always modeled as non-reactive. In a study of an artificially-produced reactive Mach stem from interferograms obtained by White and Cary (1963), Strehlow (1964) concludes that a non-reactive triple point balance is appropriate in the region of the primary triple point.

A single non-reactive slip stream balance for the $2H_2$-O_2-7Ar mixture at 6.67 kPa is compared to numerical schlieren images (Fig. 4.4) and found to be in reasonable agreement (to within the resolution of the calculation) close to the triple point. As can be seen from the figure, the greatest discrepancy is in the transverse wave angle away from the triple point; the transverse wave is calculated to be almost perpendicular to the incident wave by the local non-reactive analysis. However, the transverse wave will interact with the reaction zone behind the incident wave, curving the wave towards the cell centerline as it moves into a region with higher speed of sound. An alternative explanation is the existence of a second triple point, unresolved by the numerical simulation. Deiterding (2003) recently carried out a simulation of detonation in $2H_2$-O_2-7Ar, P_1=6.67 kPa in two-dimensions with detailed chemistry. The resolution of the study was increased relative to previous studies by a factor of more than 4.5 in both spatial dimensions and a second triple point is observed. The single triple point polar calculation does not preclude the existence of a more complex Mach reflection since a second triple point calculation does not affect the initial triple point solution, but the angle of the downstream portion of the transverse wave is likely to be affected by such a secondary triple point.

An attempt was made to use shock and detonation polars to calculate a triple point configuration involving secondary triple points. Following the procedure commonly used to calculate double Mach reflections, the calculation was first made in the frame of the first

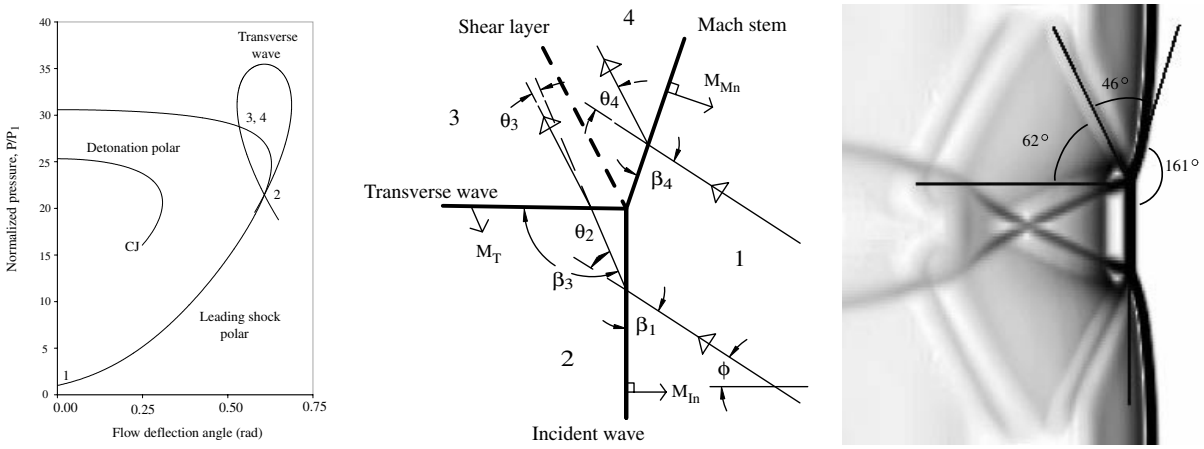

(a) (b) (c)

Figure 4.4: (a) Shock and detonation polars for stoichiometric hydrogen–oxygen mixture diluted with 70% argon, initial pressure 6.67 kPa, $x - x_o = 0.91L$, ϕ=33°. (b) Calculated wave angles from (a). (c) Triple point polar calculation superimposed on numerical schlieren from Eckett (2000) for $x - x_o = 0.91L$, in stoichiometric hydrogen–oxygen diluted with 70% argon, initial pressure 6.67 kPa.

triple point as discussed previously, then a transformation was made to the coordinate system of the second triple point where a similar second triple point calculation can be made. To perform this shift, the model of Law and Glass (1971) was used. This model assumes the second triple point moves with the velocity induced in the flow behind the incident wave (region 2, see Fig. 4.4) in the laboratory frame. For weakly unstable detonations considered in the study, the flow in region 3 becomes subsonic under this transformation and a double triple point configuration is not possible. However, the Law-Glass model was conceived for unreactive flow over a wedge and its use here is certainly speculative. In addition, the calculation assumes the flow is steady in the frame of the primary triple point.

Single triple point configurations were calculated for the mixtures in the experiments: stoichiometric H_2-O_2 with 80% Ar, with 85% Ar, and with 60% N_2 dilution, all at 20 kPa initial pressure. The calculated values for stoichiometric H_2-O_2 with 70% Ar at 6.67 kPa is also shown for comparison. Results for one location in the cell are shown in Table 4.1.

$2H_2$-O_2-	70% Ar	80% Ar	85% Ar	60% N_2	65% N_2
M_{In}	4.3	4.2	4.0	4.4	4.3
θ_2	35°	34°	33°	39°	39°
$(P_3\text{-}P_2)/P_2$	0.34	0.33	0.33	0.38	0.37
M_T	1.2	1.2	1.2	1.4	1.4
β_3	115°	112°	111°	124°	123°
θ_3	4°	4°	3°	6°	6°
β_4	76°	75°	75°	79°	79°
M_{Mn}	5.0	4.8	4.6	5.2	5.0

Table 4.1: Triple point configuration at $x - x_o = 0.7L$, (U/U_{CJ}=0.94), with $\phi = 33°$.

The Mach stem velocity, M_{Mn}, shown above does not correspond to the calculated centerline Mach stem velocity from Eckett (2000), which implies the Mach stem is curved. Except immediately at the apex of the cell, the centerline velocity of the Mach stem is lower than that predicted by the local triple point analysis, indicating the wave is weaker away from the triple point. The induction distance is therefore greatest at the centerline and the Mach stem shock may have more curvature than is apparent in the PLIF images of the OH contour.

The transverse wave strength and shock angle are very sensitive to changes in the track angle. From sooted foils mounted on the side wall of the test section, we observe cell-to-cell variations in the track angle of around ±3° for each mixture. The cell-to-cell variation results in a range of transverse wave strengths. In order to make qualitative comparisons of the triple point configurations in different mixtures, the track angle was held constant for the analysis shown above. A study of the influence of track angle is presented in Table 4.2, where the minimum, maximum, and average track angles measured from the side wall soot foils are used in calculating the triple point configuration. As can be seen from the table, changes in track angle have a significant effect on the transverse wave structure. An increase in track angle through the second half of the cell is evident in soot foil tracks of some detonations, particularly those with orthogonal structure (Strehlow, 1969). As the transverse wave strength increases with increasing track angle, this is consistent with the evolution of the transverse wave structure observed by Strehlow and Crooker (1974)

ϕ	θ_2	$(P_3\text{-}P_2)/P_2$	β_3	θ_3	β_4	M_T
30°	35°	0.20	105°	1.6°	71.°	1.1
33°	34°	0.33	113°	3.9°	75°	1.2
36°	34°	0.47	120°	5.2°	77°	1.4

Table 4.2: Triple point configuration with varying track angle for $2H_2$-O_2-12Ar at 20 kPa initial pressure. Triple point values are the minimum, maximum and average value observed on a soot foil for this mixture. The incident wave Mach number is kept constant at M_{CJ}.

and Lefebvre and Oran (1995).

Constant volume explosion calculations were made to obtain OH mole fraction contours in the region of the triple point. The detailed chemical mechanism of Warnatz and Karbach (1997), previously validated against shock tube ignition delay data (Schultz and Shepherd, 2000), was used. The constant volume calculations were carried out for flow along several particle paths through the calculated triple point configuration (see Fig. 4.5). A contour is drawn linking the locations along each path at which the OH mole fraction reaches a specified value representative of the end of the induction zone. Distance along the path is calculated by multiplying the time by the post-shock velocity. This is a commonly-used estimate that is reasonable as long as the velocity does not vary substantially within the induction zone. Particle path 1 passes directly through the Mach stem. The flow along particle paths 2-10 passes through the incident wave and is partially reacted before passing through the transverse wave. The transverse wave was assumed to remain straight with constant Mach number. Particle path 11 passes through only the incident wave before the OH mole fraction reaches the defined value. The dependence of the location of the rise in OH mole fraction, and therefore of the induction distance, on the varying shock strength in different parts of the front, results in the discontinuous keystone structure we see in the PLIF images.

Fig. 4.5a shows the calculated OH mole fraction contour for a transverse wave strength of 0.325 in $2H_2$-O_2-17Ar, initial pressure 20 kPa. Other weakly unstable mixtures considered in experiments have similar profiles. Varying the track angle has the most significant effect on the OH contour. Fig. 4.5b shows a calculated OH mole fraction contour in the

same mixture for a significantly increased track angle, $\phi = 40°$, corresponding to a transverse wave strength of 0.666.

These calculations show quantitative agreement with the PLIF images, although the location of the shock structure in the images must be estimated. From this analysis and from the images themselves, we can conclude the transverse waves have little influence on the reaction in weakly unstable fronts. We also find that the shear layers separate reacted and unreacted gas to form the keystones.

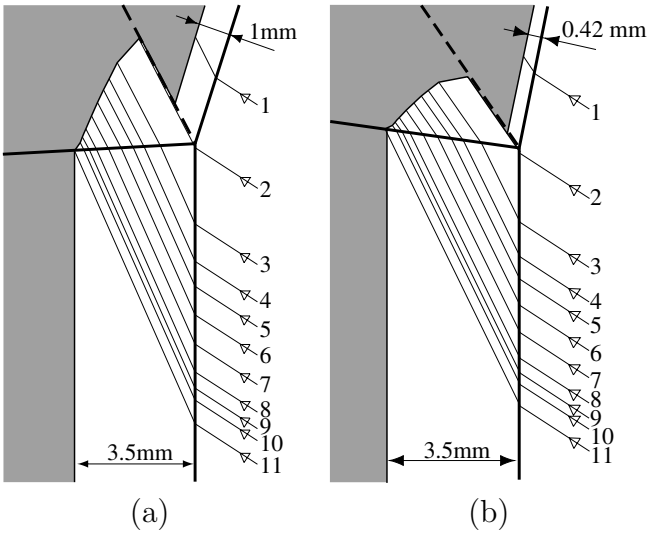

Figure 4.5: Prediction of the keystone region shape for $2H_2$-O_2-17Ar for (a) $\phi = 33°$ and (b) $\phi = 40°$. These predictions are based on the idealized model of the triple point configuration and estimates of the OH mole fraction using zero-dimensional reaction zone models, as discussed in the text. The transverse wave is assumed to be straight with constant Mach number. The edge of the reaction zone is defined as the location of the contour χ_{OH}=0.005, an arbitrary choice but as the OH rise is exponential, the features remain qualitatively the same irrespective of the chosen value.

4.1.2 Detonation in narrow channel

In the narrow channel facility, the facility dimension is smaller than the characteristic length scale of the instability, the cell width, and the out-of-plane transverse wave structure is suppressed or weakened. As a result, schlieren images of the lead shock

configuration may be directly compared to PLIF images of the reaction front.

Triple point configurations in general appear to be of weak type, irrespective of the location in the cell cycle. Images of a detonation in the narrow channel for a weakly unstable detonation in a similar mixture to Fig. 4.3 is shown in Fig. 4.6. Keystone features are again apparent in the PLIF images. From the overlaid images of the shock configurations and the reaction front structure in Fig. 4.6 (c), it can be seen that as expected from the ZND model, the stronger portions of the lead shock have a significantly shorter induction time than weaker portions. The keystones are associated with the spatial instability of the front and the shear layer separates reacted and unreacted gas, forming the boundary of the keystone, while the transverse wave does not significantly accelerate combustion, as predicted by the analysis in Section 4.1.1.

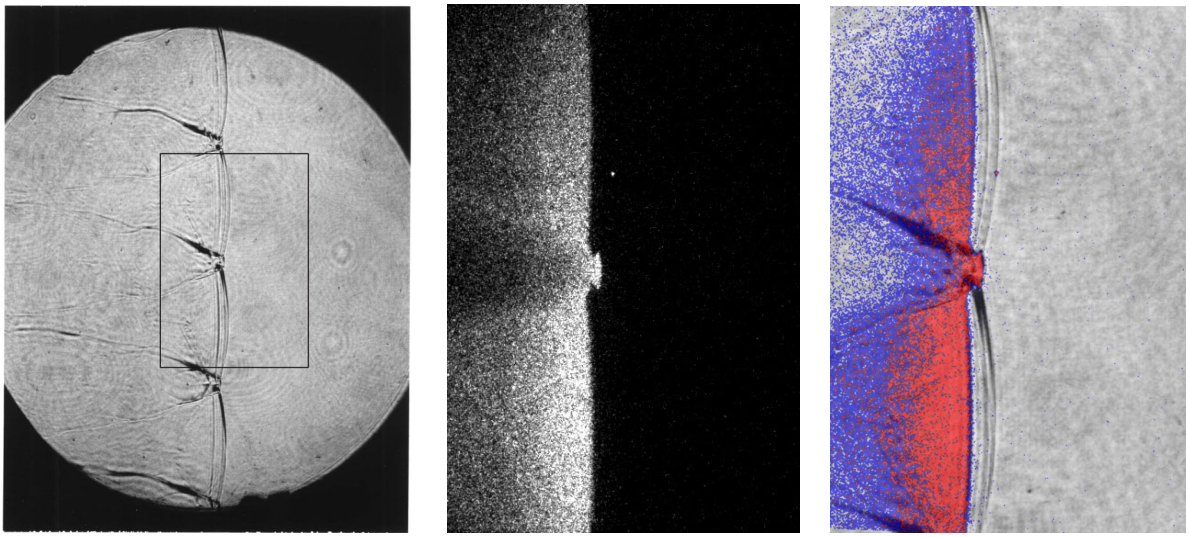

(a) (b) (c)

Figure 4.6: Images of detonation front propagating from left to right in $2H_2$-O_2-12Ar, P_1=20 kPa in the narrow channel (Shot nc73). (a) Schlieren image. The box shows the location of the corresponding OH fluorescence image shown in (b). (c) Superimposed schlieren and fluorescence image (the false color is a function of the intensity of the signal). PLIF image is 60 mm high.

Schlieren images of the front in the narrow channel show a "double" structure, shown in detail in Fig. 4.7. One possible explanation of this structure is that it is an artifact due to either (a) misalignment of the axis of the schlieren light beam and the windows

or (b) shock front curvature. Possibility (a) may be discounted since the alignment of the schlieren system through the windows was measured to be less than 0.05°, while a minimum 3° misalignment is required to result in the 1-2 mm spacing observed in the images. Possibility (b), shock front curvature was considered. A shock front with constant negative curvature of 80 mm radius will produce a 1 mm displacement of the front across the channel. This radius of curvature is greater than the cell length of the detonations in Fig. 4.2 (28 and 70 mm respectively). In addition, both the curved (Mach stem) and relatively straight (incident wave) portions of the front display the double structure to the same degree. Most compellingly, constant shock curvature does not produce two distinct fronts in a schlieren image. As pointed out by Prof. Hans Hornung of GALCIT, an inflection point is required. We conclude that the double front is not an artifact and the inflection point is explained by the presence of a single-mode out-of-plane instability. Although the channel is narrow, apparently a small amplitude instability is excited in the narrow dimension, resulting in a three-dimensional structure. A schematic of three-dimensional wave structure with a single out-of-plane transverse wave is shown in Fig. 4.8.

An oscillation in the OH number density along the centerline of a cell, forming a vertical stripe, is observed in several images, one of which is shown in Fig. 4.9. This feature occurs in the second half of the cell cycle and may be attributed to the out-of-plane instability which is seen in the schlieren images. The vertical line is the tip of a keystone in the perpendicular direction. For a more detailed discussion see Pintgen et al. (2003). This out-of-plane structure is is commonly observed in images from the narrow channel (Appendix A). It is less common in images from the GDT, but does occur (Pintgen, 2000). The two planes of the cellular structure are expected to be more repeatably orthogonal in the narrow channel since there are no area changes.

When the out-of-plane structure appears in the PLIF images, the keystones are no longer as evident. Instead, a portion of the transverse wave appears to become more closely coupled with the reaction, and a second triple point may occur at the intersection with the out-of-plane structure.

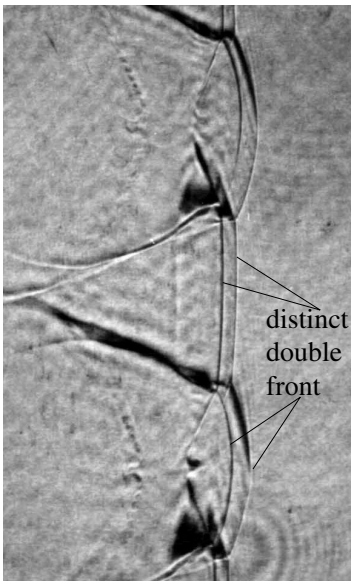

Figure 4.7: Detail from Fig. 4.2 (b) showing distinct double waves at front. Image height is 62 mm.

4.2 Collision process

Fig. 4.10 shows the post collision structure in a weakly unstable $2H_2$-O_2-17Ar mixture. Two pairs of shear layers may clearly be seen: the first pair attached to the front behind the newly formed Mach stem and the second, downstream, pair which were formed by the previous cell cycle and now interact with the reflected transverse waves. A jet of fluid may be seen between the two pairs, a feature which is seen in the numerical simulations of Sharpe (2001). A triangular region of low OH mole fraction that was part of the keystone before collision at the end of the previous cell cycle may be seen downstream of the second shear layer pair. As the transverse wave propagate through this gas, reaction occurs behind it. Incomplete consumption of the unreacted gas behind the incident wave by the transverse waves during the collision has been proposed as a mechanism for the formation of pockets of unreacted gas downstream of the front (Section 4.2.1).

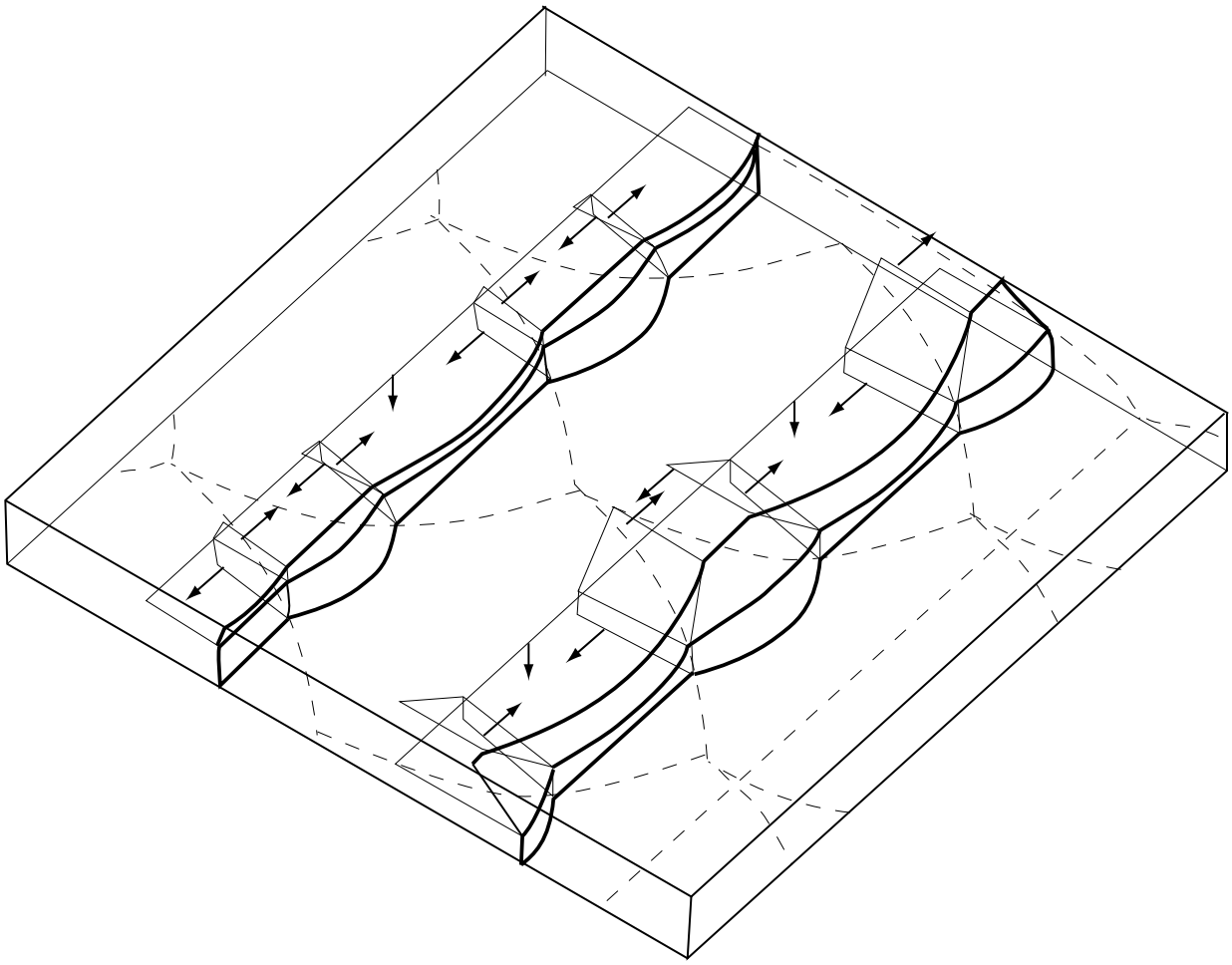

Figure 4.8: Schematic of detonation front propagating in narrow channel at two times. One out-of-plane instability (or slapping wave) is present, resulting an inflection point in the leading shock front. Shear layers are omitted for clarity.

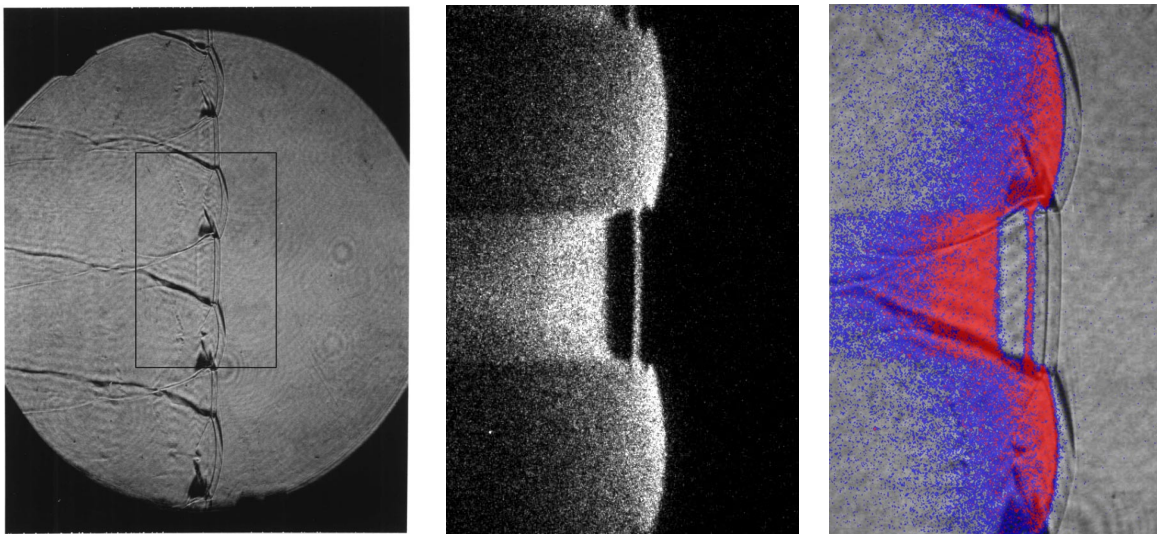

(a) (b) (c)

Figure 4.9: Images of a detonation front in $2H_2$-O_2-12Ar, P_1=20 kPa in the narrow channel (Shot nc77). (a) Schlieren image. The box shows the location of the corresponding OH fluorescence image shown in (b). (c) Superimposed schlieren and fluorescence image. PLIF image is 60 mm high.

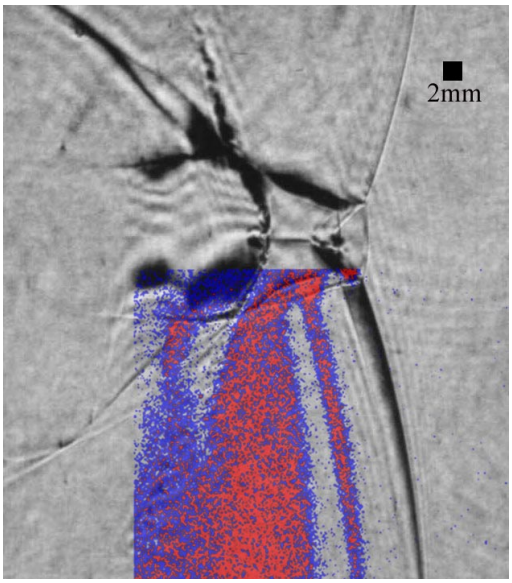

Figure 4.10: Overlaid schlieren and OH fluorescence images showing post-triple point collision structure in $2H_2$-O_2-17Ar, P_1=20 kPa (Shot nc82). Only a portion of the schlieren image was simultaneously imaged by the ICCD camera.

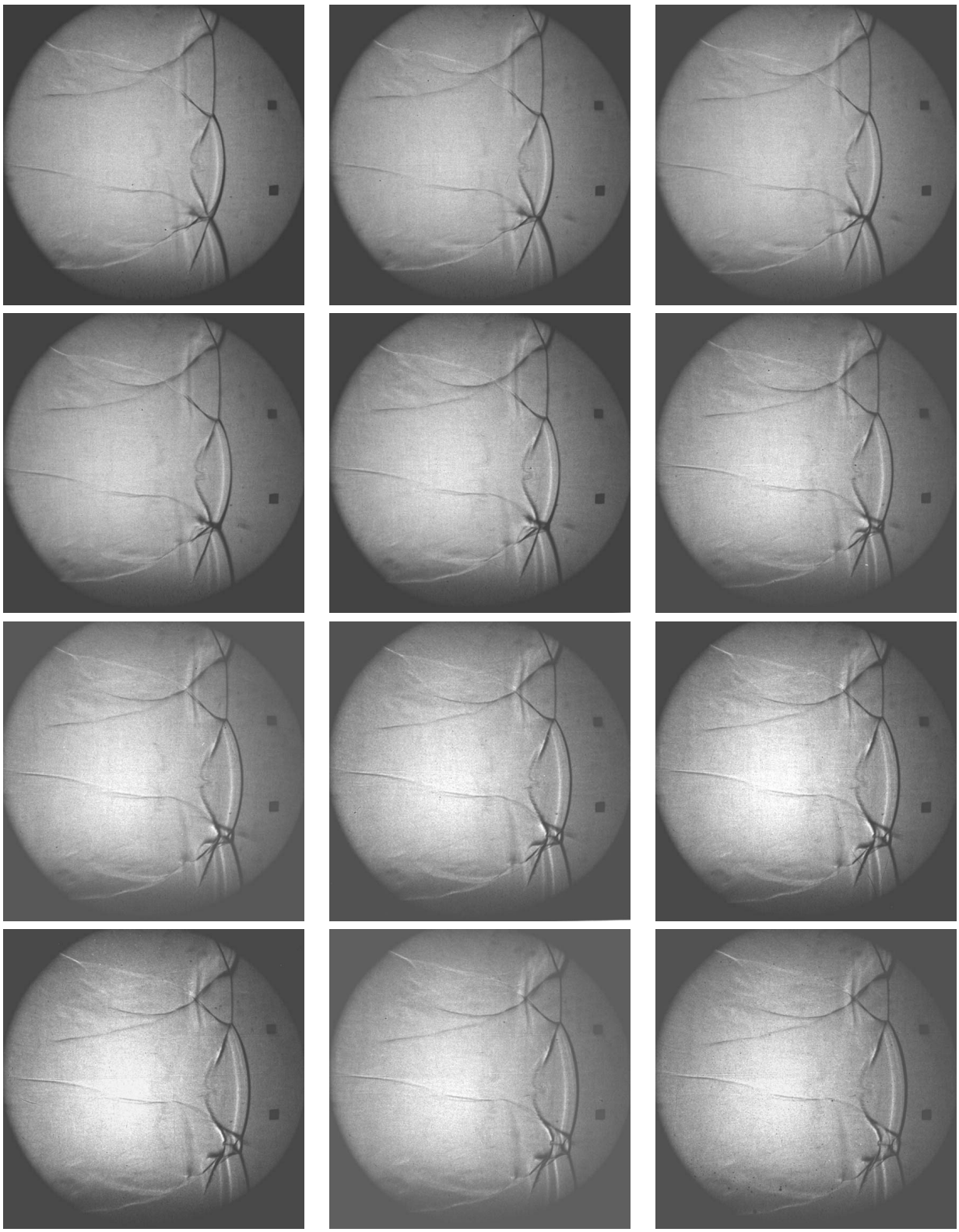

Figure 4.11: Time-resolved shadowgraph images of $2H_2$-O_2-17Ar, P_1=20 kPa, in the narrow channel (Shot nc260). Time between frames is 0.83 μs. Field of view is about 138 mm.

4.2.1 Unreacted gas pockets

"Islands" of unreacted gas that become isolated downstream of the main detonation front were first discussed by Subbotin (1975) in his schlieren study of the detonation structure of regular and irregular mixtures. In an irregular mixture, CH_4-$2O_2$-0.2Air [1], he concluded from polar calculations based on the observed wave angles that the transverse wave configurations were usually unreactive and reported that unburnt islands of gas were formed. In these irregular methane mixtures, the unburnt islands were fragmented by the fine scale cellular structure. These detonations were reported to be self-sustaining. In a regular mixture, $2H_2$-O_2-3Ar, he reported reactive transverse waves and no pocket formation except when the initial pressure was lowered sufficiently for the detonation to become marginal. In these marginal cases, he concluded both reactive and unreactive transverse wave configurations were observed. He showed schematically how regular, triangular-shaped, unburnt gas islands could be formed after the collision of unreactive transverse waves. He noted that in these mixtures, the detonation was unstable and failing. Subbotin's conclusions about the reaction zone structure, while very interesting, are based on (often unpublished) schlieren images, and furthermore, result from experiments conducted in a very narrow (4.7 mm) channel which was also rather short (1.4 m long), making it difficult to determine whether the detonation was self-sustaining.

In 1982, Edwards made schlieren images in a $2H_2$-O_2-4.5Ar mixture in a narrow (6.3 mm) channel and observed density gradients of irregular regions of gas on the order of one cell width downstream of the front (Oran et al., 1982). An accompanying numerical simulation of a detonation near its initiation limit in this mixture shows a region of increased induction time left isolated after the collision of an unreactive triple point with an axis of symmetry. In more recent numerical simulations, Gamezo et al. (1999b) report that unburnt pockets are commonly observed and conclude mixtures with low activation energies (E_a/RT_{vN}=2.1) show unburnt pockets that are triangular in shape with indistinct boundaries while higher activation energy (E_a/RT_{vN}=7.4) mixtures have

[1] stoichiometric CH_4-O_2 diluted with 6% air

distinct, irregular pockets which survive further downstream. Gamezo et al. (1999a) believe the mechanism by which the pockets are consumed also varies with the activation energy of the mixture. Pockets in low activation energy mixtures react by auto-ignition after shock compression, while pockets in irregular mixtures are consumed by heat and mass exchange with neighboring hot gases through diffusion and turbulence.

Sharpe (2001) observes the collision of two transverse wave configurations in which the secondary triple point becomes detached from the front before collision. The triple point configuration that remains attached to the front is not strong enough to consume the unreacted gas upon collision, resulting in an unburnt pocket. Sharpe also shows that numerical resolution can play an important role in determining the structure of the triple point and the presence of unburnt regions with insufficient resolution resulting in an artificially accelerated reaction rate.

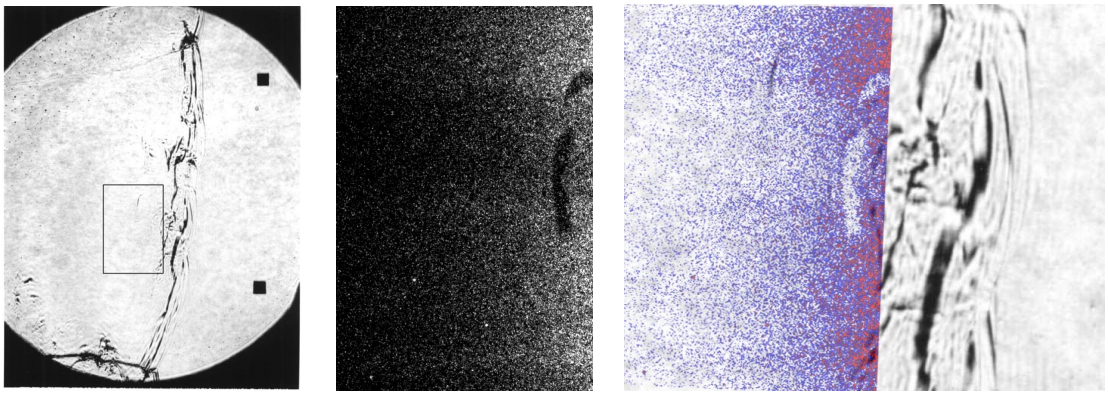

(a) (b) (c)

Figure 4.12: Images of detonation front propagating from left to right in $2H_2$-O_2-$5.6N_2$, P_1=20 kPa in the narrow channel (Shot nc115). Isolated regions of low fluorescence intensity are evident downstream of the lead shock. (a) Schlieren image. The box shows the location of the corresponding OH fluorescence image shown in (b). (c) Superimposed schlieren and fluorescence images (The false color is a function of the intensity of the signal). PLIF image is 60 mm high.

In detonations propagating in the narrow channel, isolated regions of low OH mole fraction are observed a distance on the order of a cell width downstream of the leading front. Fig. 4.12 shows two isolated low OH fluorescence signal regions approximately 13 mm downstream of the lead shock. It is important to note, however, that the detona-

tion in this experiment was traveling with a gradually decaying wave speed and a velocity deficit of 11% was measured by the window location, indicating the wave may be failing. Regions of low fluorescence intensity are not observed this far downstream in hydrocarbon mixtures, but the fluorescence intensity decreases more rapidly with increasing downstream distance in hydrocarbon mixtures.

Chapter 5 Highly Unstable Detonation

We extend our study to highly unstable detonation fronts, which include hydrocarbon mixtures. Table 5.1 gives mixtures parameters for some mixtures considered in this study. These mixtures have a range of values of the stability parameters θ and Q and so have different locations relative to the neutral stability boundary, Fig. 1.6. Argon-diluted mixtures have been classified as weakly unstable since they are close to the neutral stability boundary with low activation energy and chemical energy. The structure of these mixtures has been relatively well studied and they are used for comparison and contrast with more unstable fronts. Over 110 experiments were performed in highly unstable mixtures, over 90 in N_2-diluted H_2-O_2 and over 60 in Ar-diluted H_2-O_2 in order i) to capture different portions of the cell cycle and ii) ensure features were repeatable.

Mixture	U_{CJ} (m/s)	Δ (mm)	T_{vN} (K)	P_{vN} (MPa)	θ	Q	Instability
$2H_2$-O_2-12Ar	1517.9	0.7	1899.3	0.41	5.2	24.2	weak
$2H_2$-O_2-17Ar	1415.0	1.3	1775.3	0.44	5.4	14.7	weak
$2H_2$-O_2-3.5N_2	1958.0	0.7	1501.4	0.54	6.2	45.3	moderate
$2H_2$-O_2-5.6N_2	1796.6	1.4	1403.2	0.49	6.9	36.3	moderate
H_2-N_2O-1.33N_2	2017.5	1.5	1613.7	0.72	11.1	55.2	high
H_2-N_2O-1.77N_2	1954.7	2.3	1574.4	0.68	11.5	52.2	high
C_2H_4-3O_2-8N_2	1870.1	2.6	1627.4	0.72	12.4	53.7	high
C_2H_4-3O_2-10.5N_2	1844.1	3.2	1613.5	0.69	12.1	56.9	high
C_3H_8-5O_2-9N_2	1934.4	1.7	1643.7	0.82	12.7	65.3	high

Table 5.1: Some calculated detonation front mixture parameters. The induction length, Δ is calculated using the ZND code and detailed kinetics as described in Section 1.3.2. The normalized activation energy θ is calculated as described in Section 1.3.3 using a constant volume assumption and detailed kinetics. The Warnatz and Karbach (1997) mechanism was used for ethylene mixtures, the Mueller et al. (2000) mechanism for N_2O mixtures and the Konnov (1998) mechanism for all others. Other parameters are calculated using STANJAN. Parameters are calculated at 20 kPa initial pressure, and 298 K nominal initial temperature.

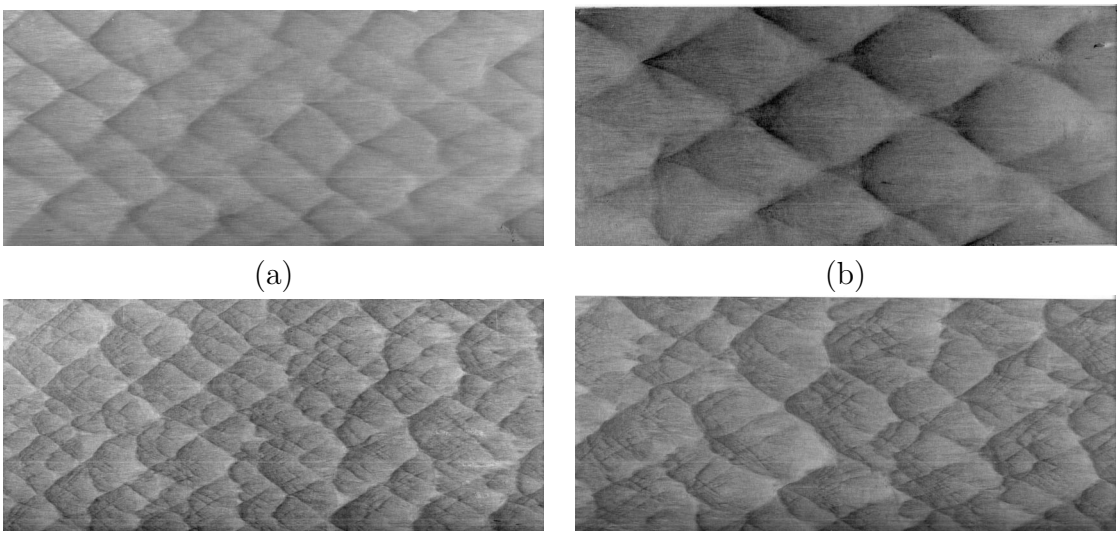

Figure 5.1: Sample soot foils from weakly unstable detonation (a)$2H_2$-O_2-12Ar (Shot nc39) and (b) $2H_2$-O_2-17Ar (Shot nc38), and from highly unstable detonation (c) H_2-N_2O-$1.33N_2$ (Shot nc43) and (d) C_3H_8-$5O_2$-$9N_2$ (Shot nc47). Detonation propagated from left to right and foils were mounted downstream of the window section of the narrow channel. Image height is about 152 mm.

Velocity deficits in highly unstable fronts are about a factor of two less than in weakly unstable fronts, as shown in Sect. 3.2. As discussed in Chapter 1, soot foils show a marked difference in weakly unstable and highly unstable detonation. Fig. 5.1 shows soot foils for weakly unstable mixtures (a and b) and highly unstable mixtures (c and d). Two different length scales (cell width or induction length) are shown for each mixture. In both cases, a much broader spectrum of scales of cellular instability is observed in the highly unstable detonations.

This more complex structure with a large range of scales is also observed in schlieren images. Sample schlieren images of weakly unstable and highly unstable detonation fronts in the narrow channel are shown in Fig. 5.2. The dominant cell width is approximately the same for mixtures (a) and (c), and (b) and (d), but additional structure is observed in the highly unstable fronts. The lead shock is more irregular and structures over a broader range of scales are apparent. The spatial oscillation in the lead shock location

is greater for highly unstable detonation. The temporal oscillation of the front through one cell cycle will be considered in the Section 5.2.

OH fluorescence images are shown in Fig. 5.3. Highly unstable detonation fronts contrast markedly with weakly unstable fronts. The "keystone" features are not as distinct and the front appears rough and wrinkled rather than smooth. Isolated, small-scale, regions of low fluorescence are observed within the high intensity region behind the main reaction front. The appearance of these fronts suggests that velocity and density fluctuations occur on a scale much smaller than that of the dominant cell width.

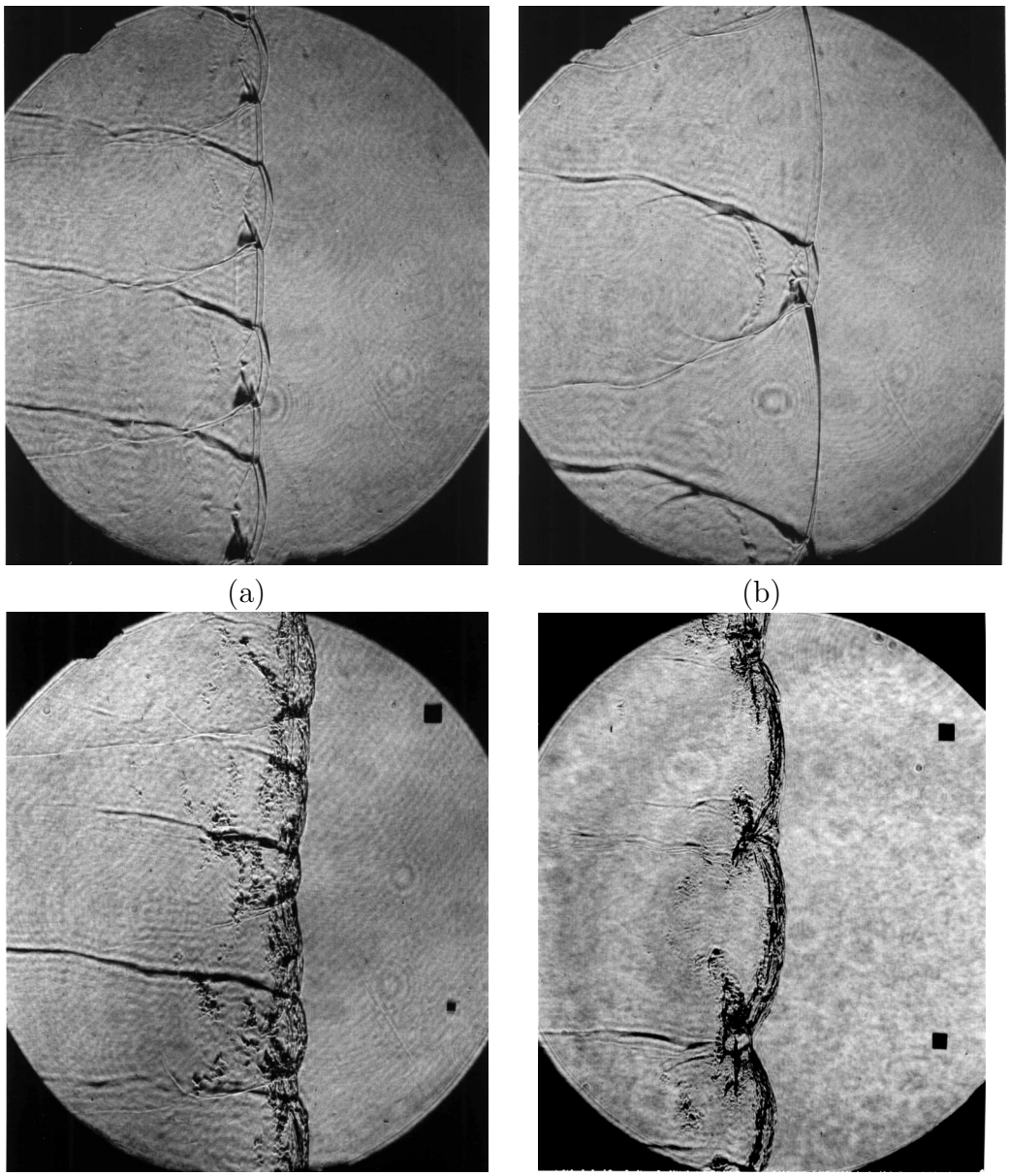

Figure 5.2: Schlieren images of weakly unstable detonation: (a) $2H_2$-O_2-12Ar (Shot nc77) and in (b) $2H_2$-O_2-17Ar (Shot nc81) and highly unstable detonation: (c) H_2-N_2O-1.77N_2 (Shot nc85) and in (d) C_2H_4-$3O_2$-$9N_2$ (Shot nc148), P_1=20 kPa. Field of view is about 146 mm. Detonations propagate from left to right in the narrow channel facility.

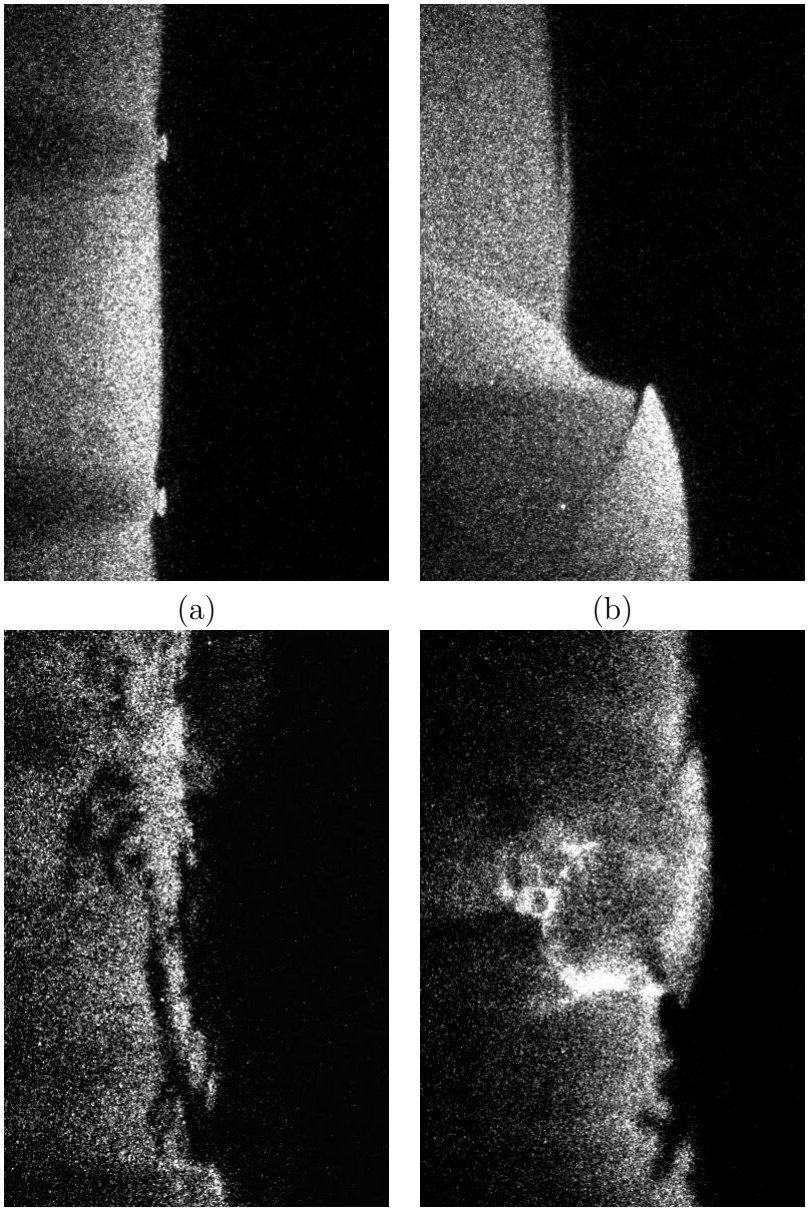

Figure 5.3: OH fluorescence images in weakly unstable detonation: (a) $2H_2$-O_2-12Ar (Shot nc65), (b) $2H_2$-O_2-17Ar (Shot nc78) and highly unstable detonation: (c) H_2-N_2O-$1.33N_2$ (Shot nc163), (d) C_2H_4-$3O_2$-$9N_2$ (Shot nc188), all at P_1=20 kPa. Image height is 60 mm in (a) and (b) and 30 mm in (c) and (d). Detonations propagate from left to right in the narrow channel facility.

5.1 Transverse waves and triple point structure

Triple point calculations were made to determine transverse wave strengths and induction times as discussed in Section 4.1.1. Parameters for a range of mixtures from weakly unstable Ar-diluted H_2-O_2 to highly unstable mixtures are shown in Table 5.2.

Mixture	$C_{p_{vN}}$ kJ/kg-K	c_1 m/s	M_T	$(P_3 - P_2)/P_2$	E_a/RT_{vN}	τ_T μs	τ_T/τ_I
$2H_2$-O_2	2.87	537	1.4	0.38	5.4	0.25	0.54
$2H_2$-O_2-3Ar	1.08	379	1.3	0.36	5.0	0.32	0.54
$2H_2$-O_2-12Ar	0.69	339	1.2	0.33	5.2	0.94	0.51
$2H_2$-O_2-$3N_2$	1.72	416	1.4	0.38	6.1	0.89	0.52
$2H_2$-O_2-CO_2	1.96	411	1.4	0.38	10.1	1.5	0.54
CH_4-$2O_2$	2.09	355	1.5	0.38	11.8	1.3	0.44
C_2H_4-$3O_2$	1.86	326	1.6	0.39	6.8	0.38	0.58
C_3H_8-$5O_2$	2.01	306	1.7	0.40	10.5	0.28	0.56

Table 5.2: Mixture parameters and transverse wave strengths for some sample mixtures, calculated in the vicinity of a primary triple point. All calculations are for mixtures at 20 kPa. $C_{p_{vN}}$ and c_1 are calculated using STANJAN. E_a/RT_{vN} is calculated as described in Section 1.3.3. Other parameters are calculated from a three shock polar calculation, as discussed in Section 4.1.1. The incident wave Mach number is kept constant at M_{CJ}, the track angle is assumed to be 33°. Activation energy and induction time calculations use the detailed chemical mechanism of Konnov (1998), previously validated against shock tube ignition delay data by Schultz and Shepherd (2000).

The reactivity of the transverse waves can be ordered by τ_T/τ_I, the ratio of the constant volume induction time for a particle passing through the incident wave and then immediately through the transverse wave τ_T normalized by the induction time behind the incident wave τ_I. This parameter has a range $0 \leq \tau_T/\tau_I \leq 1$. Values close to 0 correspond to a very short induction time behind the transverse wave, so that the transverse wave may be called reactive. Values close to 1 correspond to a relatively long induction time, meaning the transverse wave has a negligible effect on the reaction. For all the mixtures shown here, τ_T/τ_I is about 0.5. Transverse wave strength $(P_3 - P_2)/P_2$ increases with increasing distance from the stability boundary, from 0.33 to 0.40, as θ increases from 5 to 11.

5.2 Lead shock oscillation

Time-resolved studies of the detonation front can provide information about the unsteadiness of the front and the variation of fluid properties through a cell cycle. Fig. 5.4 shows the lead shock velocity U as a function of distance through the cell cycle from numerical simulation by Eckett (2000) for weakly unstable $2H_2$-O_2-7Ar, P_1=6.67 kPa. A schematic of a cell is also shown. In the simulation by Eckett, the velocity of the lead shock smoothly decays from U=1.2U_{CJ} at the beginning of the cell to U=0.9U_{CJ} at the end before the next transverse wave collision. The magnitude of the oscillation in the lead shock velocity for this numerical simulation of weakly unstable detonation in two dimensions is $0.3U_{CJ}$.

High-speed shadowgraph movies may be used to track the lead shock location along the cell centerline through the cell cycle. x-t diagrams for a sample weakly unstable and highly unstable detonation are shown in Fig 5.5. Data from several separate experiments in the same mixture are combined, since one movie is not sufficiently long to collect data through an entire cycle. Fig. 5.5 (a) shows the upstream portion of the cell and (b) shows a downstream portion. The velocity of the hydrocarbon mixture at the apex of the cell is $1.42U_{CJ}$ and at the end of the cell is $0.69U_{CJ}$. For a weakly unstable, $2H_2$-O_2-17Ar, detonation, the wave is traveling at the CJ velocity at the apex of the cell and at $0.84U_{CJ}$ at the end (a global velocity deficit is expected in the narrow channel). The oscillation in the centerline velocity for the highly unstable mixture, $0.73U_{CJ}$, is significantly more substantial than for weakly unstable detonation, $0.16U_{CJ}$. The magnitude of the lead shock oscillation for the weakly unstable case is about half that of Eckett's simulation.

Data from two-dimensional numerical simulations support this result. The velocity of the lead shock through a cell cycle for three different activation energies has been calculated numerically by Gamezo et al. (1999b). They found the magnitude of the temporal oscillation in the lead shock strength increased for higher activation energy mixtures.

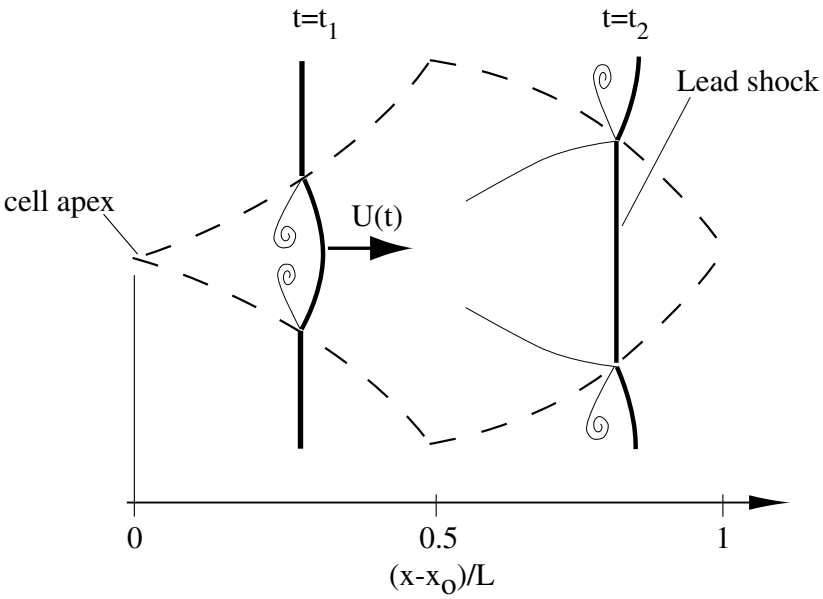

(a)

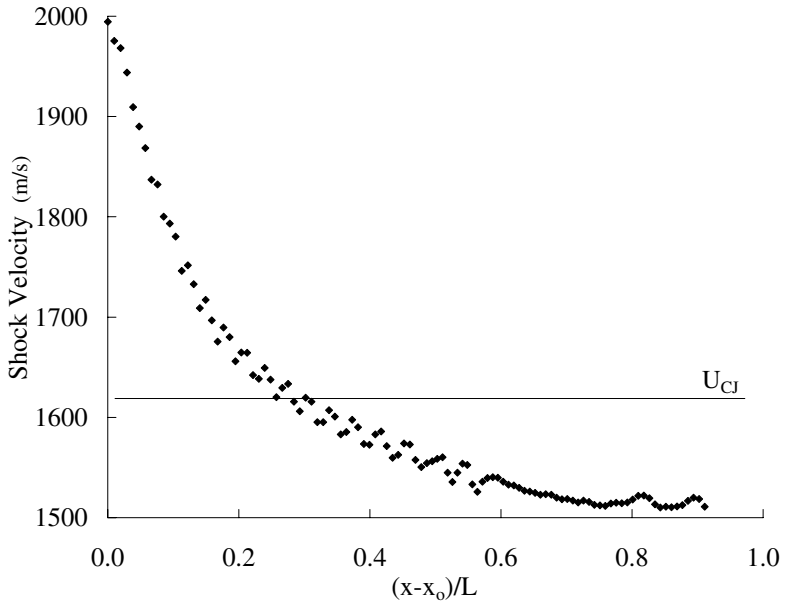

(b)

Figure 5.4: (a) Schematic of a portion of the lead shock propagating through cell of length L. The dashed line is the triple point track. The lead shock is shown at two different times. After a triple point collision (at x-x_o/L=0), the shock velocity is greater than U_{CJ}. As the shock progresses through the cell, the velocity decays smoothly until it is less than U_{CJ} at the end of the cell (at x-x_o/L=1). In the first half of the cell, x-$x_o/L < 0.5$, the lead shock is referred to as a Mach stem. In the second half of the cell, x-$x_o/L > 0.5$, the lead shock is referred to as an incident wave. (b) Lead shock velocity as a function of distance x from the cell apex at x_o from numerical simulation by Eckett (2000) for weakly unstable $2H_2$-O_2-7Ar, P_1=6.67 kPa.

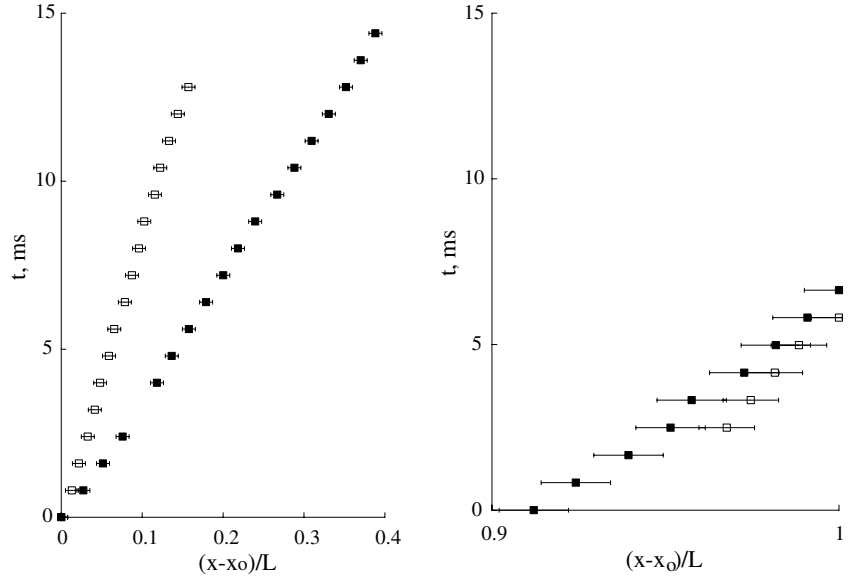

Figure 5.5: x-t diagrams of lead shock location through a cell cycle: (a) upstream portion of the cell from the apex at x_o to $(x - x_o)/L = 0.4$ where L is the cell length, and (b) downstream portion of the cell from $(x - x_o)/L = 0.9$ to $(x - x_o)/L = 1$ at the end of the cell. The time origin is arbitrary in each figure. Note the difference in scale on the abscissa. Closed squares: C_3H_8-5O_2-9N_2, open squares: 2H_2-O_2-17Ar

5.3 Local decoupling

The velocity profile of the lead shock along the cell centerline through one cell cycle, Fig. 5.4 may be compared to that of a decaying blast wave due to a release of energy at the triple point collision at the beginning of a cell (Voitsekhovskii et al., 1963, Lundstrom and Oppenheim, 1969). An analogy may be made with detonation initiation by a strong, spherical blast wave. In that situation, two outcomes are possible. Successful initiation occurs when the strong blast wave decays approximately to the CJ velocity and becomes a self-sustained spherical detonation wave. Failed initiation occurs when the shock and reaction decouple and the blast wave continues to decay to an acoustic wave.

Lundstrom and Oppenheim (1969) studied the influence of the decaying lead shock on the induction time using a "quasi-steady" model. They assumed the thermodynamic properties through the cell vary as a result of the time-dependent, decaying lead shock, but that a steady induction time could be calculated as a function of the local lead shock strength. They found reasonable agreement with experimental schlieren images of detonation in $2H_2$-O_2-$3N_2$.

We investigate the possibility of decoupling of the decaying lead shock and the reaction along the centerline of one cell cycle using the the critical decay rate (CDR) model. The CDR model was developed by Eckett et al. (2000) and includes the effect of unsteadiness on the induction time. Their results were extended to more general wave geometries by Arienti (2003). To illustrate the CDR model, the temperature reaction zone structure equation, simplified to a single-step, irreversible reaction, for a spherical wave of radius R at velocity U is

$$(1-M^2)C_P\frac{DT}{Dt} = \underbrace{(1-\gamma M^2)Qk(1-Z)\exp\left(-\frac{E_a}{R_gT}\right)}_{chemical\ energy\ release} + \underbrace{\frac{j}{R-x}w^2(U-w)}_{curvature} + \underbrace{w\frac{dU}{dt} - w\frac{\partial w}{\partial t} + \frac{1}{\rho}\frac{\partial P}{\partial t}}_{unsteadiness} \tag{5.1}$$

where Q is the chemical energy, k is the pre-exponential in the one-step reaction, Z is the product mass fraction, j is the geometry integer, x is the distance behind the lead shock, and ρ, P, T, w are the density, pressure, temperature, and fluid velocity.

The first term on the right hand side of Eqn. 5.1 is due to the chemical energy release, the second is due to wave curvature and the remaining terms are due to unsteadiness. The key result of Eckett (2000) is that the curvature term was found to be negligible and a local criterion for detonation decoupling was found as a balance between the chemical energy release term and the unsteadiness terms. Failure occurs if the shock decay time

t_d is less than a critical value $t_{d,c}$ where

$$\frac{1}{t_d} = -\frac{1}{U}\frac{dU}{dt} \quad , \tag{5.2}$$

$$t_{d,c} = 6\frac{\gamma - 1}{\gamma + 1}\theta\tau \quad . \tag{5.3}$$

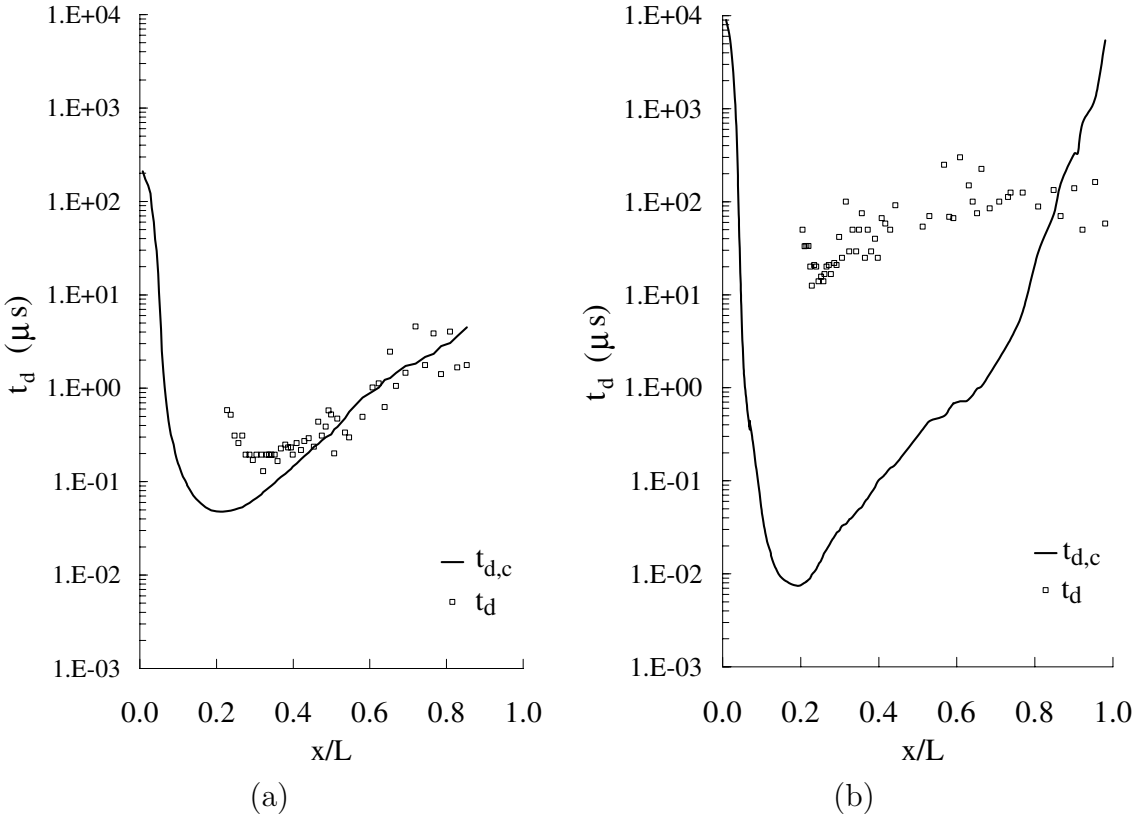

Figure 5.6: Shock decay time vs. critical decay time for (a) θ=4.9 and (b) θ=7.9 based on data from Gamezo et al. (1999b)

Lead shock velocities along the cell centerline from the numerical simulations of Gamezo et al. were used for $U(t)$. As discussed in Section 5.2, Gamezo et al. report that increasing the activation energy results in an increase in the magnitude of the lead shock oscillation through the cell. Shock decay times are calculated from this data and compared to the critical value and results are shown in Fig. 5.6 for two selected activation energies: θ=4.9 and θ=7.4. In the case of θ=4.9, Fig. 5.6(a), the decay time is never

less than the critical value, although it becomes comparable at the end of the cell. For θ=7.4, Fig. 5.6(b), the decay time is less than the critical value at the end of the cell, corresponding to local decoupling, or quenching, of the detonation wave.

(a) (b) (c) (d)

Figure 5.7: Images of the detonation front in C_2H_4-$3O_2$-$10.5N_2$, P_1=20 kPa at end of cell cycle (Shot nc177). (a) Schlieren image with outline showing location of corresponding OH fluorescence image (b) Detail of schlieren image corresponding to fluorescence image. (c) OH fluorescence image (d) Overlaid fluorescence image from (c) in false color and schlieren image from (b). Image height for (b-d) is 30 mm.

Local decoupling at the end of the cell cycle is observed in images of highly unstable fronts in the narrow channel. Fig. 5.8 shows a large oscillation in the reaction front that is apparently uncorrelated with the lead shock which appears smooth and straight.

5.4 Collision process

High-speed movies provide information about the collision process at the apex of the cell. In Fig. 5.9, a local explosion is observed to occur at the apex. Overlaid schlieren and PLIF images of the collision process have also been obtained, an example is shown in Fig. 5.8. The timing between acquiring the schlieren and PLIF images was 800 ns in this experiment, and it can be seen that the overlaid images do not correspond. The PLIF image is taken after the wave has accelerated substantially. This explosive interaction contrasts with the less dramatic interaction observed in the weakly unstable mixtures.

A "microexplosion" at the cell apex was also observed using schlieren by Vasiliev and Nikolaev (1978) in C_2H_2-2.5O_2, P_1=1.0 kPa in a 5×60 mm channel. To our knowledge, these are the only other experimental images of a collision process in a propagating detonation.

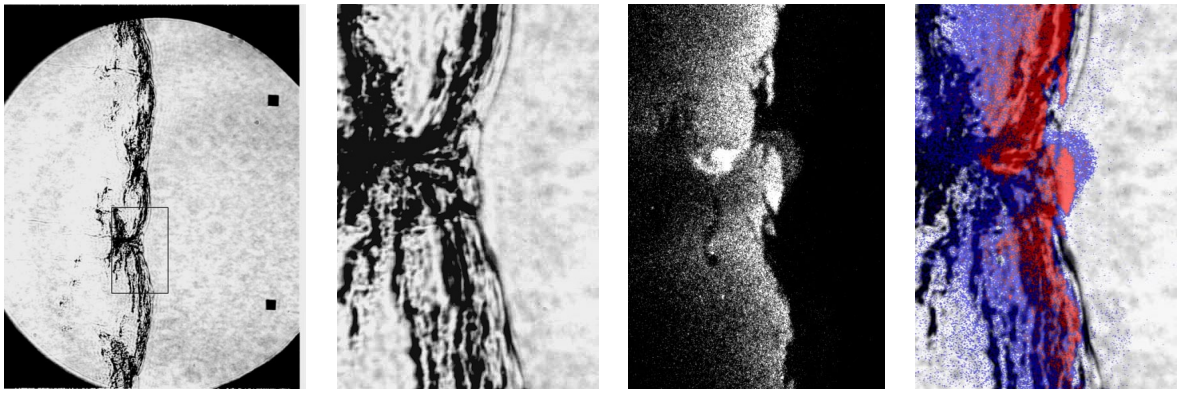

Figure 5.8: Images of explosive reinitiation at the apex of cell in a detonation front in C_2H_4-3O_2-8N_2, P_1=20 kPa (Shot nc180). (a) Schlieren image with outline showing location of corresponding OH fluorescence image (b) Detail of schlieren image corresponding to fluorescence image. (c) OH fluorescence image (d) Overlaid fluorescence image from (c) in false color and schlieren image from (b). Image height for (b-d) is 30 mm.

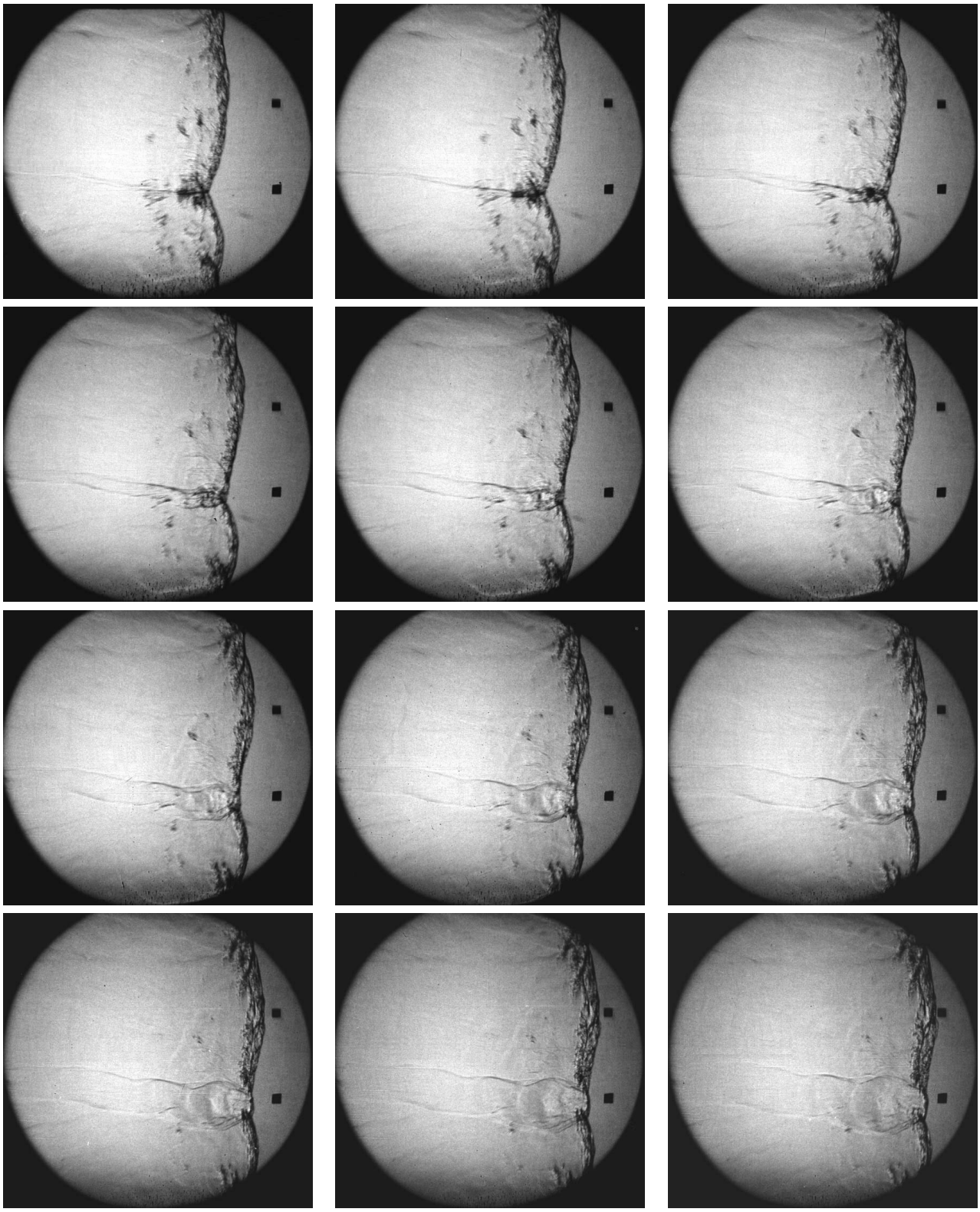

Figure 5.9: Time-resolved shadowgraph images of C_3H_8-$5O_2$-$9N_2$ in the narrow channel (Shot nc236). Time between frames is 0.83 μs. Field of view is about 138 mm.

5.4.1 Shear layers

As discussed in Section 4.1.1, "keystones" are formed in weakly unstable fronts due to spatial oscillations in the lead shock strength. The triple point analysis shows that the shear layers form the boundary between fluid particles that have passed through the strong portion of the lead shock front (Mach stem) and react relatively quickly, and particles that have passed through the weak portion of the front (incident wave) and the transverse wave and react more slowly.

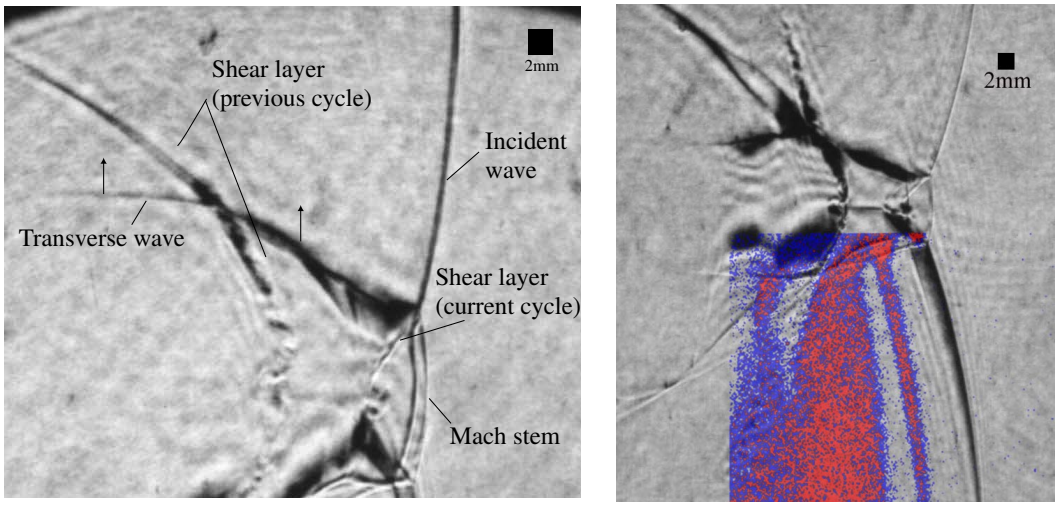

(a) (b)

Figure 5.10: Images from two separate experiments in $2H_2$-O_2-17Ar, P_1=20 kPa. Detonation propagates left to right. (a) Transverse wave has interacted with the wave of opposing family at the end of previous cell cycle. The refracted wave propagates upwards, interacting with the shear layer from the previous cycle (Shot nc83). (b) Overlaid fluorescence and schlieren images indicating reaction of unreacted gas occurs behind the transverse wave (Shot nc82).

Shear layer instabilities are observed in schlieren images of weakly unstable fronts. In Fig. 5.10 (a), the shear layer attached to the leading shock (current cycle) appears unstable. In Fig. 5.10 (b), shear layer (previous cycle) appears unstable while in Fig. 5.10 (a), the shear layer from the previous cycle appears to become unstable after interaction with the transverse wave. The instability is not evident in the corresponding fluorescence im-

age. In weakly unstable fronts, several hundred experiments have shown no shear layer instabilities in fluorescence images to the resolution of the study (at best 50 μm/pixel).

In N_2-diluted $2H_2$-O_2 mixtures, shear layer instabilities are observed in schlieren images and also in OH fluorescence images from both facilities, Fig. 5.11. Features commonly associated with Kelvin-Helmholtz instability are evident. The vortical structures have the expected rotation as the fast stream occurs behind the transverse wave where the gas is unreacted while slow stream occurs behind the Mach stem where the gas has reacted. In the GDT experiment, Fig. 5.11 (a), the cell location is unknown. In the NC experiment, Fig. 5.11 (b and c), the shear layer is not at the triple point of the dominant cellular instability, but at an intermediate triple point in the front. The appearance of unstable shear layers in PLIF images shows that, in these fronts, the instability may occur with a large difference in OH concentration across the shear layer.

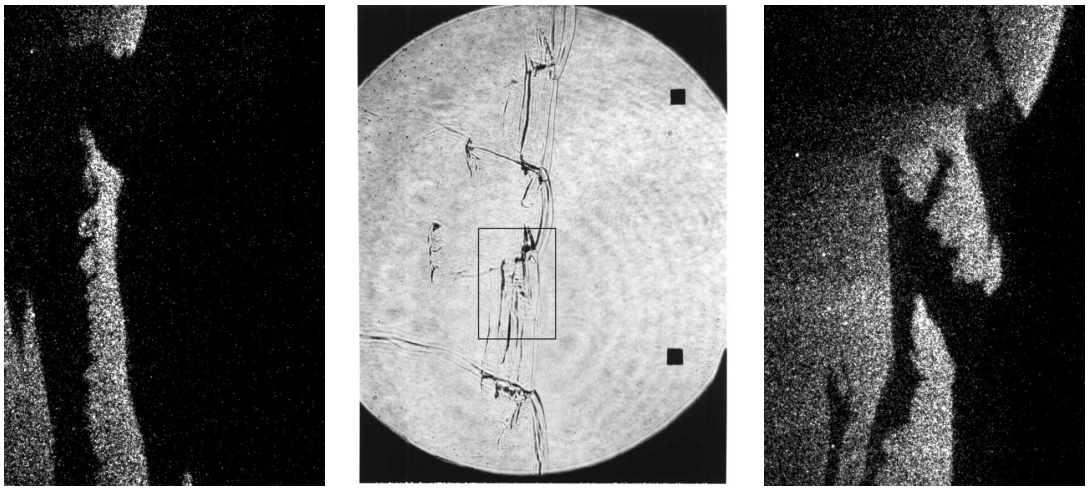

(a) (b) (c)

Figure 5.11: Images of unstable shear layers in (a) $2H_2$-O_2-$7.7N_2$, taken in the 150x150 mm test section of the GDT (Shot gdt1598), (b) schlieren and (c) OH fluorescence image in $2H_2$-O_2-$5.6N_2$ in the NC facility. (Shot nc110)

Local triple point calculations (Section 4.1.1) may be used to estimate thermodynamic properties across the shear layers, Table 5.3. Velocity differences across the shear layers are calculated to be 233 to 364 m/s, with the greatest value for N_2-diluted H_2-O_2. The

Mixture	Δ	$(P_3 - P_2)/P_2$	u_3	u_4	ρ_3	ρ_4	τ_3	τ_4
$2H_2$-O_2-17Ar	1.4	0.32	623	390	1.03	1.09	5.8	2.7
$2H_2$-O_2-5.6N_2	1.4	0.37	716	352	0.89	0.98	7.9	2.5
C_3H_8-5O_2-9N_2	1.7	0.39	554	269	1.70	1.89	5.8	1.6

Table 5.3: Calculated properties across a triple point contact surface for sample mixtures from this study. State 3 is behind the incident and transverse waves and state 4 is behind the Mach stem (Schematic is shown in Fig. 5.12). Δ is the induction length behind the incident wave (state 2). τ is the induction time. These parameters are calculated using a constant volume explosion assumption, as discussed in Section 4.1.1, using the detailed Konnov mechanism. The incident wave velocity wave is taken to be $0.9U_{CJ}$, representative of conditions near the end of the cell. In calculating the transverse wave strength, the track angle is assumed to be 33°.

induction time ratio, τ_3/τ_4, is larger for the N_2-diluted H_2-O_2 than for the Ar-diluted H_2-O_2. This calculation indicates that the shear layer separates reacted and unreacted gas over a greater length in the N_2-diluted H_2-O_2, increasing the likelihood of observing the instability in that portion of the shear layer. In contrast, shear layer instability in weakly unstable fronts appears most likely to occur either in reacted gas or at an unresolvable scale for the present experiment.

In C_3H_8-5O_2-9N_2, regions of intense chemiluminescence have been observed, Fig. 5.13. From the schlieren images, it can be determined that these regions correspond with the location of shear layers. The detonation appears to have locally decoupled at the end of the cell cycle, but the transverse wave collision has not yet occurred. If the shock and reaction front decouples at the end of the cell, the shear layer separates reacted and unreacted gas over a considerable length. With the increase in surface area in an unstable shear layer, we may speculate that local "hot spots" may be formed due to mixing of hot products and cold reactants, and possibly contribute to the re-ignition process at the end of the cell. This is a "turbulent" combustion mechanism that is not included in traditional detonation models based on shock-induced explosion.

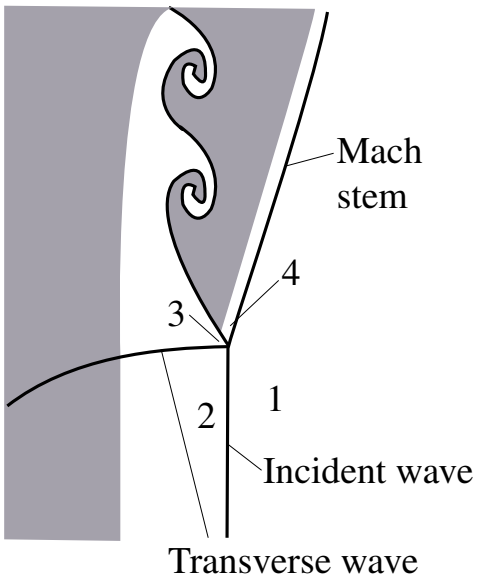

Figure 5.12: Cartoon showing states at triple point configuration. For each mixture in Table 5.3, the triple point configuration is calculated using shock polars, as discussed in Section 4.1.1. Induction times τ are calculated by taking particle paths through the three-shock configuration and using a constant volume explosion assumption.

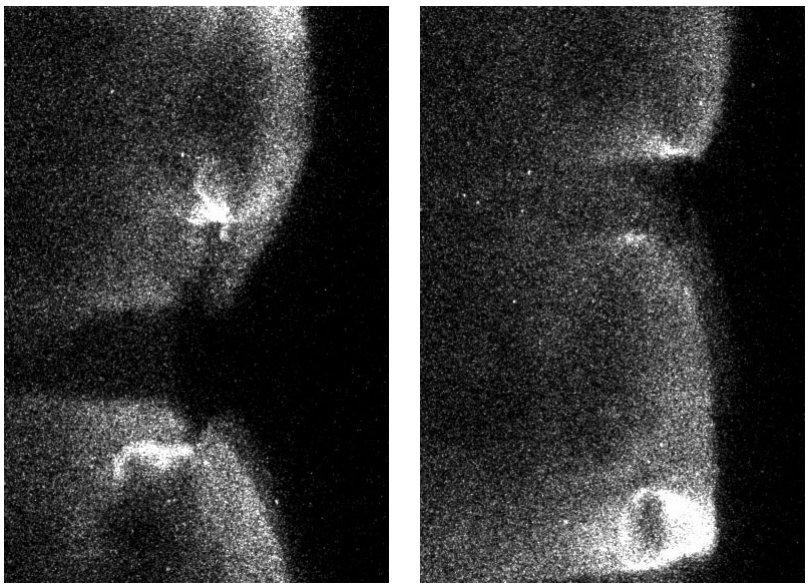

(a) (b)

Figure 5.13: Chemiluminescence images in C_3H_8-$5O_2$-$9N_2$, P_1=20 kPa. (a) Shot nc205 and (b) Shot nc206. Image height is 65 mm.

5.5 Structure over a range of scales

In some mixtures substructure is observed – cellular soot foil tracks similar in appearance to the large scale structure but appearing at multiple scales smaller than the main cell size. A soot foil showing substructure is shown in Fig. 5.14. The substructure cells are observed on the soot tracks in the upstream apex of the main cell and increase in size as the velocity of the Mach stem decays. Substructure is usually not observed in the second half of the main cell.

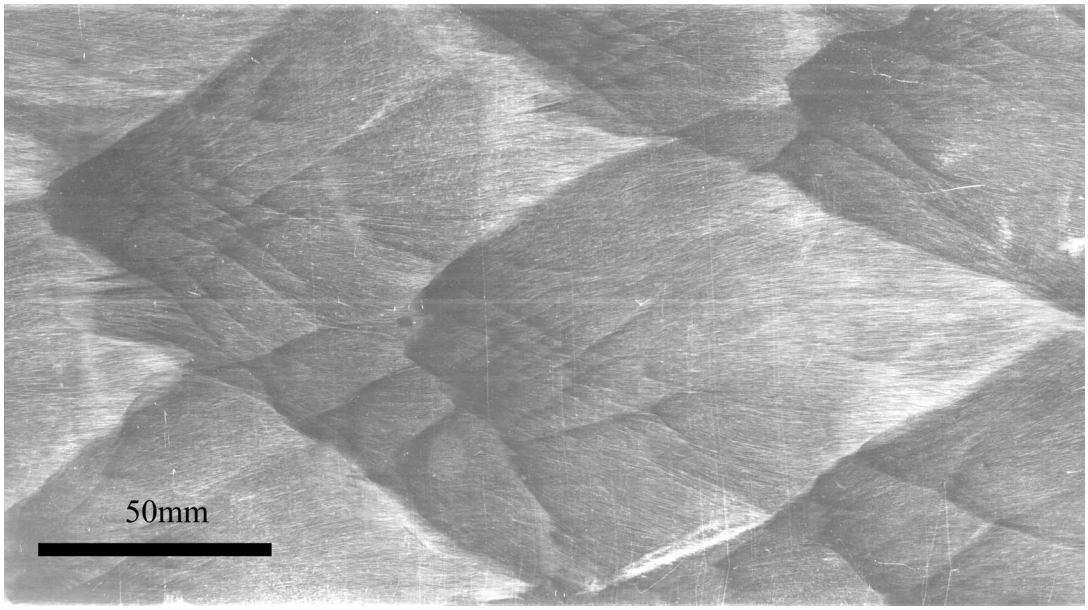

Figure 5.14: Soot foil from detonation in CH_4-$2O_2$-0.2Air, P_1=11 kPa, propagating left to right (Shot gdt1524). Substructure appears in the first half of the cell at gradually increasing length scales. Foil is from 18×127 mm channel experiment described in Section 3.1. Scale is 50 mm total length.

Substructure has been reported in several specific mixtures, including C_2H_2-N_2O-Ar (Libouton et al., 1981), lean H_2-O_2, lean C_2H_2-O_2, CH_4-O_2, C_6H_14-$11O_2$ (Manzhalei, 1977), and $3NH_3$-$3O_2$ (Strehlow, 1969). Manzhalei (1977) proposed a minimum activation energy criterion of $E_a/RT_{vN} \geq 6.5$ for substructure to occur. We observe fine scale structure in all N_2O and hydrocarbon mixtures we studied. Manzhalei's criterion is

satisfied by the hydrocarbon mixtures in this study while some N_2-diluted H_2 mixtures exceed this activation energy by up to 30% and do not have substructure. The nature and role of substructure in detonation propagation is still poorly understood.

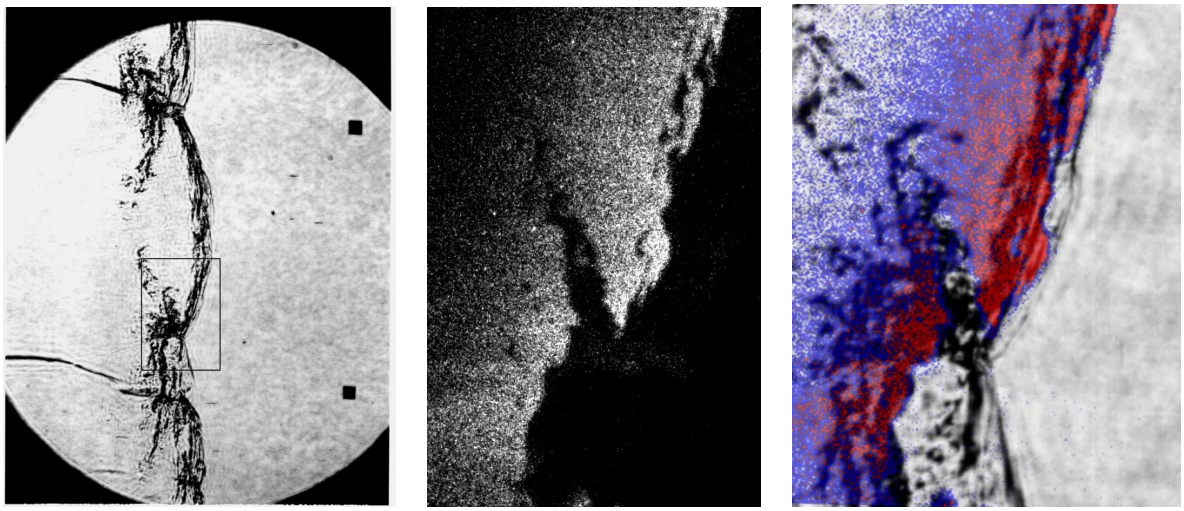

(a) (b) (c)

Figure 5.15: Schlieren and corresponding OH fluorescence images of highly unstable detonation front in stoichiometric C_2H_4-$3O_2$-$10.5N_2$, P_1=20 kPa, in the narrow channel (Shot nc175).

Sample images of a detonation in an N_2-diluted C_3H_8-O_2 mixture in the narrow channel are shown in Fig. 5.15. Half a keystone region is seen, with a very prominent region of low OH intensity at the shear layer. In contrast to weakly unstable detonation, the front in a highly unstable detonation appears rough and wrinkled and features over a wide range of length scales may be observed. Oscillations are less prominent in the schlieren image than the PLIF image due to two effects. First, changes in the lead shock strength result in larger changes in the induction time due to the Arrhenius dependence on the post-shock temperature. Second, the structure is three-dimensional at this scale and will be superimposed in an integrating schlieren image. OH fluorescence images of a H_2-N_2O mixture from (a) the 280 mm GDT facility and (b) from the narrow channel facility are shown in Fig 5.16. All fluorescence images appear to have similar small scale wrinkling of the front. A key question is whether this structure results from an instability

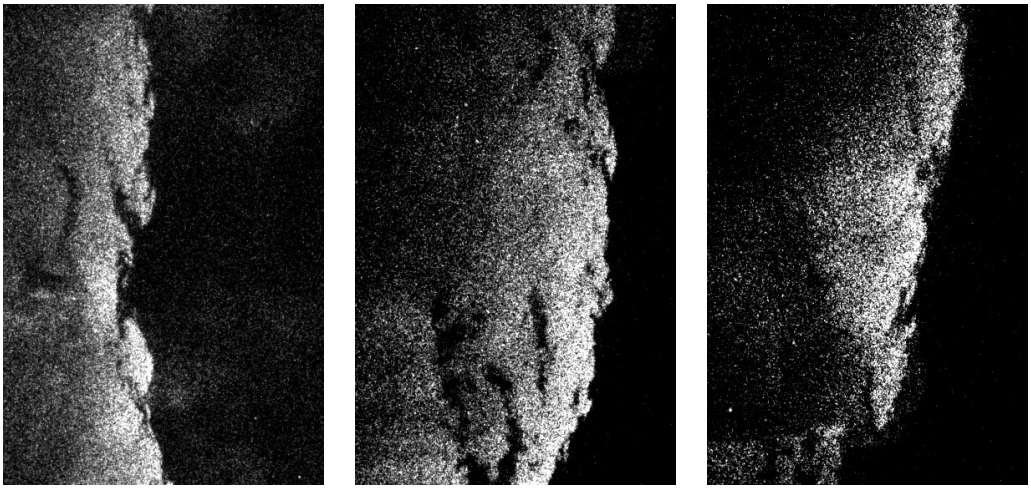

(a) (b) (c)

Figure 5.16: OH fluorescence images of H_2-N_2O-$2N_2$ detonation in the (a) 280 mm facility (Shot gdt1687) and (b) (Shot nc136) and (c) (Shot nc93) in the narrow channel. Image height is 30 mm in all three cases.

that is similar in nature to the large-scale cellular instability but occurs at a smaller scale behind the overdriven Mach stem, i.e., substructure, or whether this is due to a change in combustion regime, i.e., turbulent mixing induced by spatial and temporal fluctuations in the shock front strength.

5.5.1 Range of length scales

A range of length scales of cellular instability is observed on soot foils in highly unstable fronts. For example in C_3-$5O_2$-$9N_2$, the dominant cell width is measured to be 45±8 mm. In addition, cell width are observed over a range of smaller length scales, from 10 mm to unresolvable scales at < 1 mm.

As discussed in Section 1.3.3, the cell width is approximately proportional to the induction length for particular mixture and so the length scales of cellular instability may be estimated by considering the induction time as a function of the lead shock strength through one cell cycle. Induction time τ is calculated as a function of lead shock strength by making a constant-volume adiabatic explosion assumption for a particle behind the

lead shock. The calculation is zero-dimensional, steady, and a detailed kinetics scheme is used. Induction time vs. lead shock strength is shown in Fig. 5.17 (a). The range of lead shock strength for each mixture is chosen based on the numerical data of Gamezo et al. (1999b). From our experiments (Section 5.2), we observe the change in the lead shock strength through one cell cycle is even greater - a factor of 4 times more - in highly unstable fronts than in weakly unstable fronts.

Assuming the post-shock velocity w_{vN} is constant in the induction region, the induction length Δ is calculated as $\Delta = w_{vN}\tau$. The induction length and cell width have been found empirically to be approximately proportional over a range of mixtures. Assuming the same constant of proportionality may be used over a range of scales, the cell width of the small-scale structure or substructure may be estimated from the calculated induction time. Fig. 5.17 (b) shows the substructure cell width, normalized by the dominant cell width, as a function of lead shock strength. It can be seen that the range of scales at which cellular instability may occur in highly unstable mixtures is about 3.5 orders of magnitude in comparison with only about 2 orders of magnitude for the weakly unstable case, and structure at significantly smaller scale is possible.

Stability considerations may be used to further limit the range of available scales by considering the stabilizing effect of increasing the lead shock velocity. As discussed in Section 1.3.4, hydrodynamic stability analysis of detonations to longitudinal perturbations was carried by Lee and Stewart using a normal modes approach. The one-dimensonal analysis was extended to transverse instability by Short and Stewart. The relevant mixture parameters are: the chemical energy Q, and the activation energy E. The third parameter, the overdrive f, is defined as the square of the ratio of the local shock velocity to the CJ value. Short and Stewart found that increasing the overdrive leads to sequential suppression of high frequency modes, so that at higher overdrive only a limited range of frequencies remains unstable until at sufficiently high overdrive only one low frequency mode is unstable. Except in the case of infinitely low energy release, the detonation can not be overdriven to be stable to transverse instability (although this is possible in the case of longitudinal disturbances).

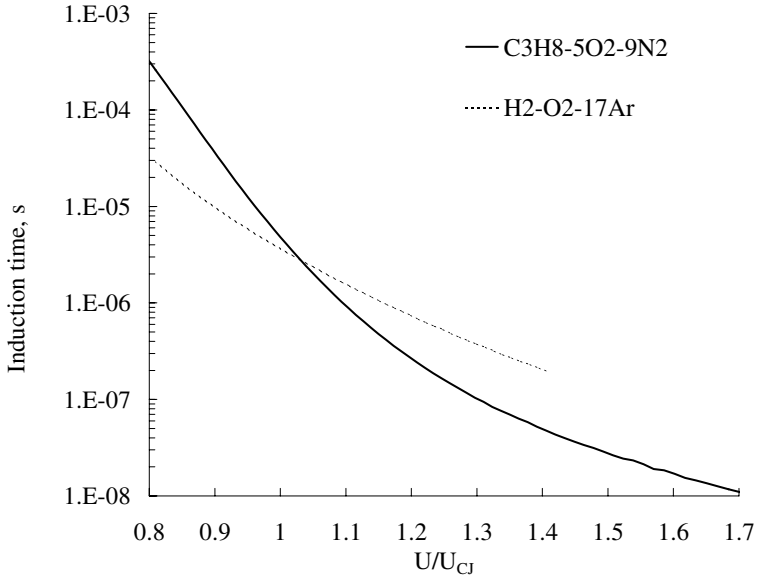

(a)

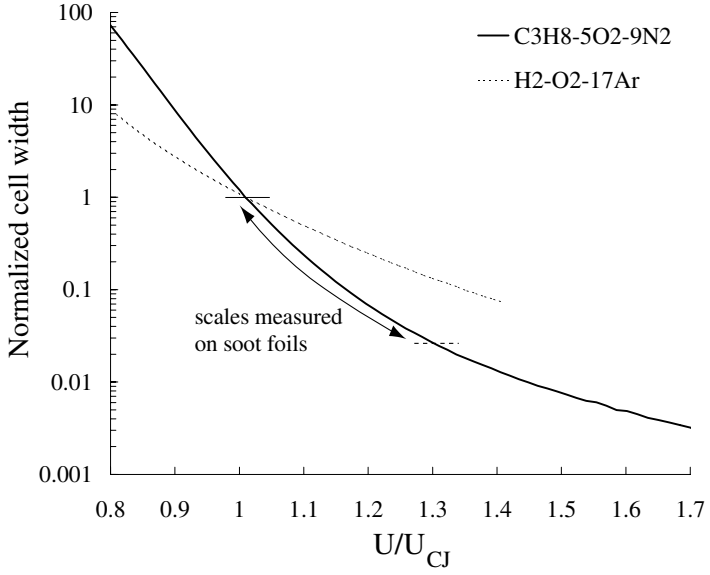

(b)

Figure 5.17: (a) Induction time calculated as a function of lead shock strength using a zero-dimensional constant volume appoximation and the detailed kinetics mechanism of Konnov (1998). (b) Estimation of substructure cell width as a function of lead shock strength. The range of fine scale cells observed on a soot foil in this mixture is also shown. The lower bound is set by the resolution at which cells may be detected by eye, about 1 mm.

5.6 Statistical description of fluctuations

Experiments show spatial and temporal oscillations of the detonation front occur over a large range of scales for highly unstable mixtures. In highly unstable fronts, the change in the induction zone length through one cell cycle is calculated to be 3.5 orders of magnitude. An even larger range of scales needs to be considered if diffusive processes, which are traditionally neglected, play a role, for example in the shear layers, (Section 5.4.1). Resolving this range of structure in a numerical simulation is an extremely challenging problem and a subgrid scale model may be neccesary. The cellular structure is random in the sense that the phase at one location or one time is not repeatable and multiple experiments may not be combined in a coherent sequence. These considerations motivate a statistical approach.

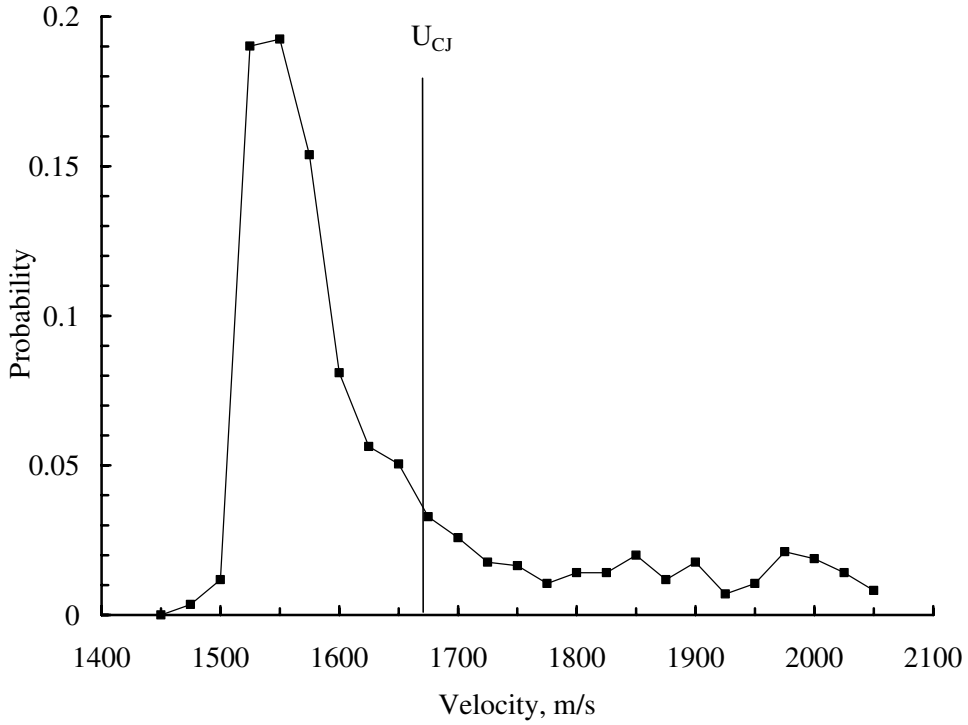

Figure 5.18: Probability distribution of lead shock velocity through one cell cycle. Data from numerical simulation by Eckett (2000), $2H_2$-O_2-7Ar, P_1=6.67 kPa.

The oscillations due to the cellular instability at the dominant scale are first con-

sidered, using data from a numerical simulations by Eckett for the velocity of the lead shock through one cell cycle, shown in Fig. 1.2 (b). A discrete time series of lead shock velocities was analyzed to determine the frequency of occurrence in the following fashion. The velocity range is divided into bins, the number of total observations in each were normalized to obtain the probability estimate, and the resulting probability distribution is shown in Fig. 5.6. The CJ velocity is shown by the vertical line. The distribution is skewed towards the left of the CJ value as the detonation spends more time at slower speeds.

Temporal data for small-scale structure (substructure) is very difficult to obtain. Instead, the spatial data in the fluorescence images may be considered, with the caveat that the analogy between fluctuations in time and in space is valid for a uncorrelated, stationary process. A sample image is shown in Fig 5.6 (a). Image processing was carried in MATLAB. The image was first filtered with a gaussian filter of 1 pixel radius, the contrast was increased so that each pixel was either black or white (threshold 0.5), and edge detection was carried out. The resulting image is shown in Fig. 5.6 (b). The mean of the edge contour is calculated, Δ_s, together with the horizontal displacement of the edge about the mean.

The goal is to obtain a first estimate of the lead shock fluctuations from the fluctuations in the induction time. The location through the cell at which the image was taken may be estimated from the corresponding schlieren image to be (x-x$_o$)/L = 0.29. The mean local shock velocity U_s corresponding to this location in the cell can be estimated from the data of Gamezo et al. to be $U_s = 1.05\ U_{CJ}$ for a mixture with an activation energy of 7.4.

We calculated the induction length for $U_s = 1.05\ U_{CJ}$ in the experimental mixture, H_2-N_2O-1.64N_2, using a constant volume, adiabatic explosion assumption to be 0.59 mm. The mean location of the reaction in Fig. 5.6 (a) Δ_s is set to this value, so that Δ_s =0.59 mm.

A probability distribution of the horizontal displacement of the edge about the mean is shown in Fig. 5.6 (a). From this, we find that the most probable induction length

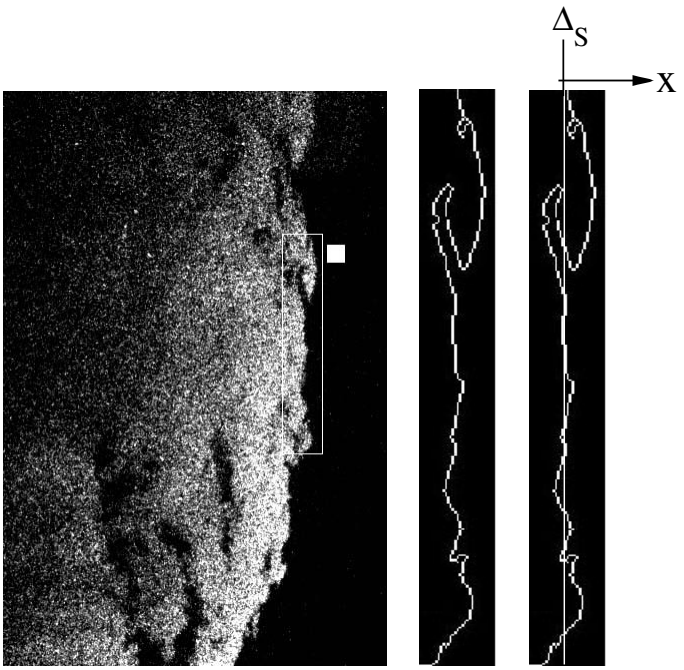

Figure 5.19: (a) Fluorescence image of a portion of the reaction front in H_2-N_2O-1.64N_2 (Shot nc136). Scale is 1 mm. (b) Location of sharp rise in OH radical at end of induction zone, found from applying the edge detection algorithm on the outlined region in (a). (c) We calculate the mean of this contour, Δ_s, and the horizontal displacement of the edge in x about the mean, Δ_s. The mean, Δ_s, is then set to be the local calculated induction length, a function of the local lead shock velocity, as discussed in the text.

is about 0.2 mm longer than the mean value. This is consistent with the lead shock probability distribution shown in Fig. 5.6, which shows the most probable velocity in the cell cycle is less than the CJ value. From Fig. 5.6 (a), the magnitude of the fluctuation about the mean is estimated to be about 1 mm. So we have an estimate of the magnitude of the fluctuations in the induction length Δ' about the mean induction length Δ_s in the detonation front shown in Fig. 5.6 (a)

$$\Delta'/\Delta_s \sim 1.0/0.59 = 1.7 \tag{5.4}$$

As discussed in Section 1.3.3, the induction time τ and induction length Δ may be

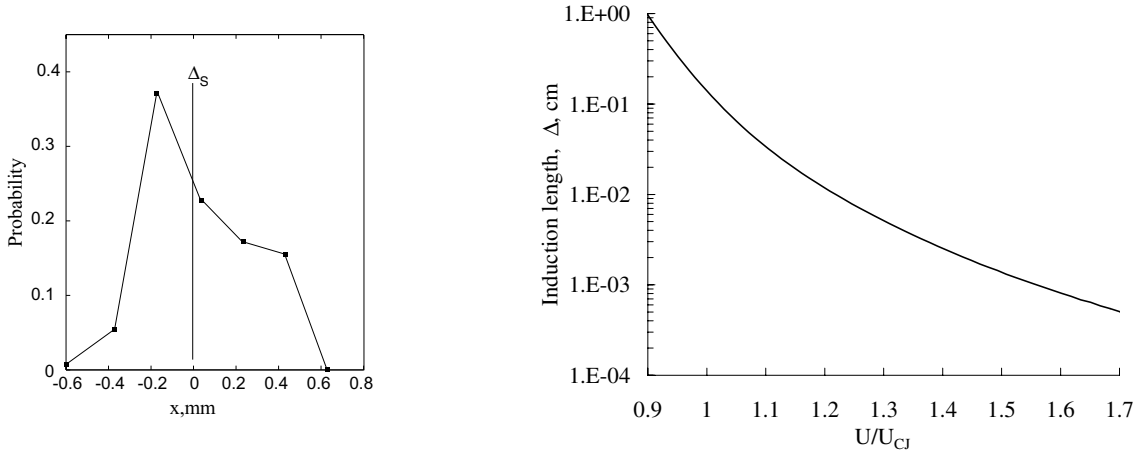

(a) (b)

Figure 5.20: (a) Probability distribution of horizontal fluctuations of the edge of the reaction zone about the mean from the data of Fig. 5.6. In the analysis described in the text, the mean is taken to correspond to the calculated induction length at the appropriate location in the cell cycle. (b) Calculated induction length, Δ, as a function of lead shock strength for H_2-N_2O-1.64N_2. Induction length is calculated assuming a constant volume explosion behind the lead shock. The detailed kinetics mechanism of Mueller et al. (2000) is used.

related by the postshock fluid velocity w_{vN}

$$\Delta = w_{vN}\tau \tag{5.5}$$

The post-shock velocity is given by the shock jump conditions as a function of the local lead shock velocity. The induction time is calculated using a constant volume explosion approximation given a lead shock velocity. We calculate induction times, and induction lengths using Eqn. 5.5, for a range of lead shock strengths for the mixture of interest (H_2-N_2O-1.64N_2). Calculated induction lengths are shown in Fig. 5.6 (b). From the measured minimum and maximum values of $\Delta \sim \Delta_s \pm 0.5$ mm, we may obtain an estimate of the fluctuation in the lead shock strength U'/U_s from this figure

$$U'/U_s \sim 0.24 \quad , \tag{5.6}$$

or

$$U'/U_{CJ} \sim 0.26 \quad . \tag{5.7}$$

The minimum and maximum lead shock velocities are therefore estimated to be $1.13U_{CJ}$ and $0.87U_{CJ}$. The induction time corresponding to each of these two lead shock velocities is directly calculated using the constant volume approximation to estimate the fluctuation in the induction time to be

$$\tau'/\tau_{CJ} \sim 2.5 \quad . \tag{5.8}$$

Shchelkin (1959) estimated that a fluctuation of $\tau'/\tau_{CJ} \sim 1$ was sufficient to cause the shock and reaction to become unstable.

In obtaining these estimates, we have assumed that spatial and temporal fluctuations in the chemical energy release relative to the lead shock location may be related using Eqn. 5.5. The constant volume, adiabatic explosion calculation is carried out assuming a steady flow, although unsteadiness may be included relatively simply (Eckett et al., 2000). The analysis is sensitive to the sample chosen and a much more extensive range of sample sizes and images needs to be analyzed.

Chapter 6 Detonation Regimes

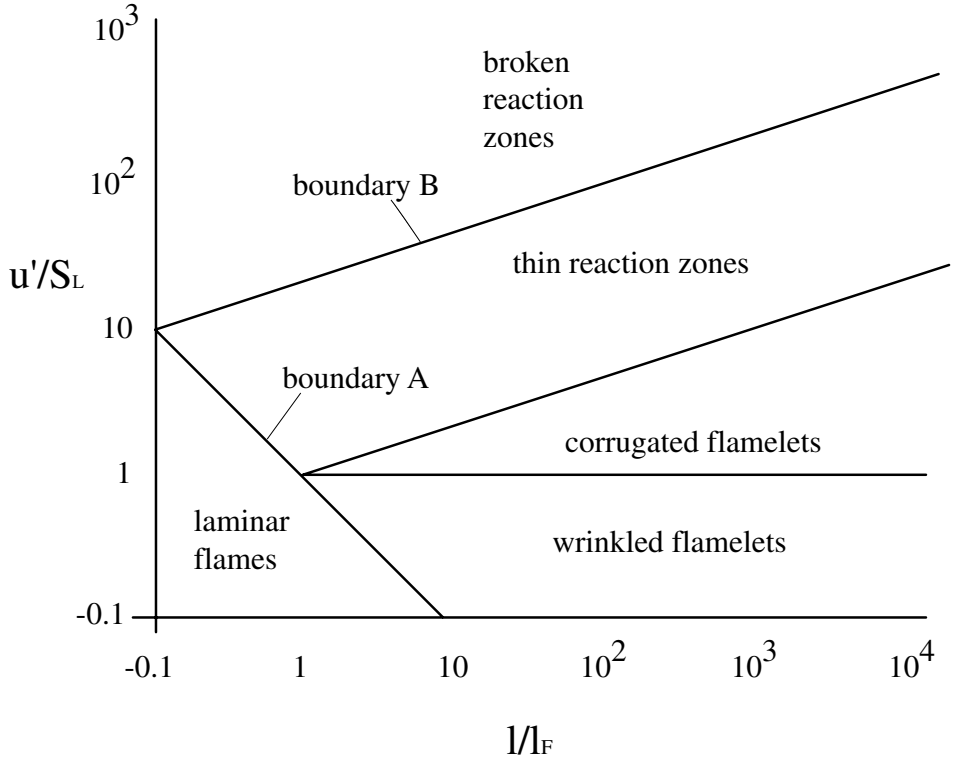

Figure 6.1: Premixed combustion regimes after Peters (2000). u' is the rms velocity fluctuation, S_L is the laminar flame speed, l is the integral length scale, and l_F is the flame thickness

The spectrum of length scales observed on soot foils and schlieren images in highly unstable detonation fronts has been motivated some researchers to make a comparison with turbulent combustion (White, 1961, Lee, 1991). Premixed turbulent combustion and detonation both involve unstable, chemically-reacting fronts and some analogies may be made, although the physical mechanisms involved are different. In turbulent combustion, the reaction front is affected by incoming eddies of the external flow which stretch the flame front, increasing the surface area and burning velocity. If strain rates are high

enough (on the order of $10^2 - 10^3$ s^{-1}, depending on the chemistry) local extinction of the reaction results. In detonation, the reaction is affected by oscillation in the lead shock strength that results in changes in the reaction rate through the Arrhenius kinetics. If the lead shock oscillations are rapid enough (with fluctuation rates exceeding the critical decay rate), local decoupling, or quenching of the detonation results.

In turbulent combustion, the effects of turbulence can be summarized in a map of combustion regimes, commonly called the Borghi diagram, Fig. 6.1, which is based on the work of numerous researchers as discussed in Peters (2000). We propose that a similar diagram may be constructed for detonation. As the axes of the diagram, we choose the magnitude of the lead shock oscillation normalized by the local average U'/U_{CJ}, and the magnitude of the fluctuation in the reaction time normalized by the local average τ'/τ_{CJ}, shown in Fig. 6.2. The induction time for a detonation propagating at U_{CJ} is τ_{CJ}. These quantities are analogous to the axes defined in Fig. 6.1 since the fluctuation (due to the cellular instability) is about the stable or "laminar" CJ solution.

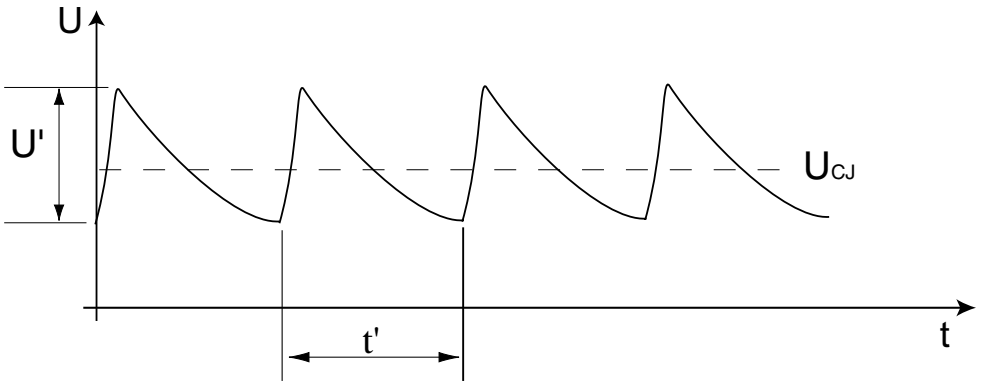

Figure 6.2: Cartoon showing lead shock velocity as a function of time through several cell cycles, based on simulation from Eckett (2000), see Fig. 1.2 (b). U_{CJ} is the velocity of the front calculated from the steady, one-dimensional CJ model.

Two boundaries from the Borghi diagram are considered in particular (Fig. 6.1): boundary A is the boundary between laminar and turbulent flames, and boundary B is boundary between distributed, or broken, reaction zones and continuous reaction zones.

Boundary A is given by setting the turbulent Reynolds number equal to one. Boundary B is unity Karlovitz number

$$Ka_\delta = \frac{l_\delta^2}{\eta^2} = 1 \tag{6.1}$$

where $l_\delta = \delta l_F$ is the inner layer thickness which is some fraction of the flame thickness, l_F, and η is the Kolmogorov length scale. Quenching due to vortices occurs above this limit, resulting in discontinuous or "broken" reaction fronts.

Now we consider how to construct the analog of Boundary A for the detonation case. We draw the analogy between the Reynolds number in turbulent flames and the activation energy in detonation. These quantities each play the role of control parameters that determine if the systems are unstable to small disturbances. The following analysis relates induction time fluctuations to lead shock velocity fluctuations through the activation energy. This can be expressed as a boundary for the onset of instability by using the 1-D neutral stability curve (Lee and Stewart, 1990) computed for one-step, irreversible reaction.

The induction time may be approximated as

$$\tau = A \exp\left(\frac{E_a}{RT_{vN}}\right) \tag{6.2}$$

where T_{vN} is the post-shock temperature. If we consider a change in the post-shock temperature δT_{vN}, the resulting change in the induction time $\delta\tau$ is

$$\delta\tau = A \exp\left(\frac{E_a}{RT_{vN}}\right)\left(-\frac{E_a}{RT_{vN}^2}\right)\delta T_{vN} \tag{6.3}$$

$$= -\tau\theta\frac{\delta T_{vN}}{T_{vN}} \tag{6.4}$$

where $\theta = E_a/RT_{vN}$ is the non-dimensional activation energy. So we have

$$\frac{\delta\tau}{\tau} = -\theta\frac{\delta T_{vN}}{T_{vN}} \tag{6.5}$$

We will assume a perfect gas. The change in the post-shock temperature may be related

to the change in the lead shock velocity δU

$$\frac{\delta T_{vN}}{T_{vN}} = \frac{1}{T_{vN}} \frac{dT_{vN}}{dU} \delta U \tag{6.6}$$

With the strong shock approximation

$$\frac{\rho_{vN}}{\rho_1} \sim \frac{\gamma + 1}{\gamma - 1} \tag{6.7}$$

where ρ_{vN} is the post-shock density, the Rayleigh line is

$$P_{vN} \sim P_1 + \frac{2}{\gamma + 1} \rho_1 U^2 \tag{6.8}$$

so that

$$\frac{dP_{vN}}{dU} \sim \frac{4\rho_1 U}{\gamma + 1} \quad . \tag{6.9}$$

From the equation of state and using the strong shock assumption, Eqn. 6.6 becomes

$$\frac{\delta T_{vN}}{T_{vN}} \sim 2 \frac{\delta U}{U} \tag{6.10}$$

so that

$$\frac{\delta \tau_{vN}}{\tau_{vN}} \sim -2\theta \frac{\delta U}{U} \tag{6.11}$$

The negative sign occurs because an increase in the lead shock strength decreases the induction time. For the present analysis, we are interested in the magnitude of the fluctuation, so we define

$$\tau' = |\delta \tau| \tag{6.12}$$

$$U' = |\delta U| \tag{6.13}$$

and relate the lead shock velocity fluctuation to the induction time fluctuation

$$\frac{U'}{U_{CJ}} \sim \frac{1}{2\theta}\frac{\tau'}{\tau_{CJ}} \tag{6.14}$$

Fig. 6.3 (a) shows Eqn. 6.14 plotted for different values of θ. From Fig. 1.6, a critical value of the activation energy for the onset of instability may be taken as the asymptote, $\theta \sim 4.5$. The induction time vs lead shock strength curve corresponding to this critical value of the activation energy is selected as the boundary (Fig 6.6) for the onset of instability, or the transition between stable (or "laminar") detonations, which are only observed in numerical studies, and unstable detonations.

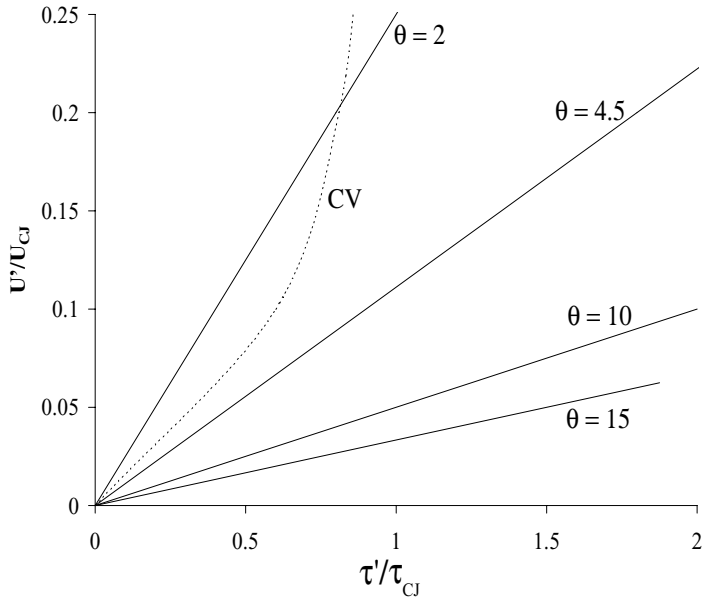

Figure 6.3: Lead shock velocity fluctuations vs. induction time fluctuations. Lines are given by expression 6.14, with slope $1/2\theta$. The critical value of θ for the onset of longitudinal instability is taken as the boundary between stable and unstable detonation.

The induction time may be also calculated as a function of the lead shock velocity for a given mixture using a constant volume approximation and detailed kinetics mechanism (Section 1.3.3). For a change in the lead shock velocity U' about the mean U_{CJ} of a given magnitude, the change in the induction time τ' about the mean τ_{CJ} may be calculated,

see Fig. 6.4. This calculation is also shown on Fig. 6.3 as the curve labeled "CV" for a mixture ($2H_2$-O_2-17Ar) with $\theta \sim 5$. The curve is linear for small variations in U and τ and lies close to the $\theta \sim 4.5$ curve for $\tau'/\tau_{CJ} \leq 0.5$.

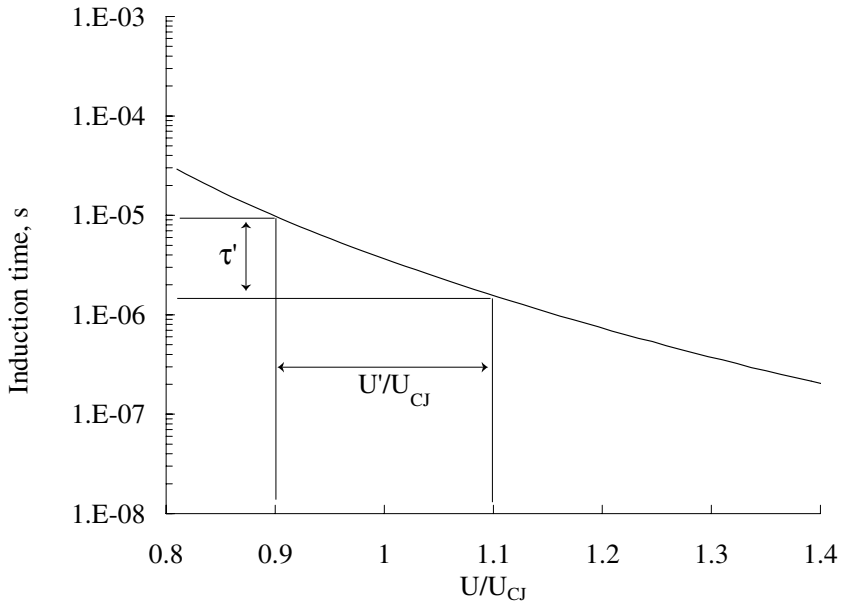

Figure 6.4: Induction time vs. lead shock velocity calculated using a constant volume approximation and detailed mechanism (Konnov, 1998) for $2H_2$-O_2-17Ar, 20 kPa. The curve labeled "CV" in Fig. 6.3 shows the induction time fluctuation for a given lead shock fluctuation from this data.

The second boundary B, between distributed and wrinkled reaction fronts, marked on Fig. 6.1 is considered. The critical decay rate (CDR) model of Eckett et al. (2000) is used. This model was applied in Section 5.3 as a criterion for local decoupling, or quenching, of the detonation through a cell cycle. We can recast the model to form a boundary for decoupled and coupled fronts. From Section 5.3, the local criterion for decoupling is

$$t_d \leq t_{d,c} \tag{6.15}$$

where

$$\frac{1}{t_d} = -\frac{1}{U(t)}\frac{dU(t)}{dt} \tag{6.16}$$

and

$$t_{d,c} = 6\frac{\gamma - 1}{\gamma + 1}\theta\tau \quad . \tag{6.17}$$

If the front has not decoupled, we approximate the change in the centerline velocity as linear in time

$$\frac{dU}{dt} \sim \frac{U'}{t'} \tag{6.18}$$

where t' and U' are the characteristic decay time and the magnitude of the fluctuation, as shown in Fig. 6.2.

The characteristic decay time t' for one cell cycle may be written

$$t' \sim L/U_a \tag{6.19}$$

where L is the characteristic cell length, and U_a is an average velocity over the cycle. As discussed in Section 1.3.3, the global scales of detonation are empirically related

$$L = C\lambda = Cw_{vN,a}\Delta_a = CAw_{vN,a}\tau_a \tag{6.20}$$

where λ is the cell width, w_{vN} is the post-shock velocity, and τ is the induction time. A typical value for C is 1.5, based on an aspect ratio of the cell with a track angle of 33° (Strehlow and Biller, 1969). As discussed in Section 1.3.3, A is typically $10 \leq A \leq 100$. The subscript a is used to denote the mean value over one cell cycle. The post-shock velocity can be obtained from the shock jump equations. Using the strong

shock approximation and neglecting terms of order $1/M$, we have

$$\frac{w_{vN}}{c_1} \sim \frac{\gamma-1}{\gamma+1}\frac{U}{c_1} \tag{6.21}$$

so that

$$t' \sim L/U_a \sim CA\frac{\gamma-1}{\gamma+1}\tau_a \quad . \tag{6.22}$$

The critical condition for decoupling from the CDR model is Eqn. 6.17, which may be approximated using the above arguments as

$$\frac{U}{U'}CA\frac{\gamma-1}{\gamma+1}\tau_a \sim 6\frac{\gamma-1}{\gamma+1}\theta\tau \tag{6.23}$$

$$\frac{U}{U'} \sim \frac{6}{CA}\theta\frac{\tau}{\tau_a} \tag{6.24}$$

where τ is the local induction time, evaluated as a function of the local lead shock strength, U, and θ is the non-dimensional activation energy.

We estimate the value of the local parameters at the end of the cell where decoupling occurs

$$U \sim U_a - U'/2 \tag{6.25}$$

where

$$\tau \sim \tau_a + \tau'/2 \tag{6.26}$$

So that the resulting expression for the critical decoupling condition is

$$\left(\frac{U_a}{U'} - \frac{1}{2}\right) \sim \frac{6\theta}{CA}\left(\frac{\tau'}{2\tau_a} + 1\right) \tag{6.27}$$

In the context of the large scale oscillations, $U_a = U_{CJ}$ and $\tau_a = \tau_{CJ}$, so

$$\left(\frac{U_{CJ}}{U'} - \frac{1}{2}\right) \sim \frac{6\theta}{CA}\left(\frac{\tau'}{2\tau_{CJ}} + 1\right) \tag{6.28}$$

Expression 6.28 may be plotted as shown in Fig. 6.5 as the boundary between coupled

and locally decoupled detonation. Representative values of C and A were chosen. Curves for different activation energy θ are shown.

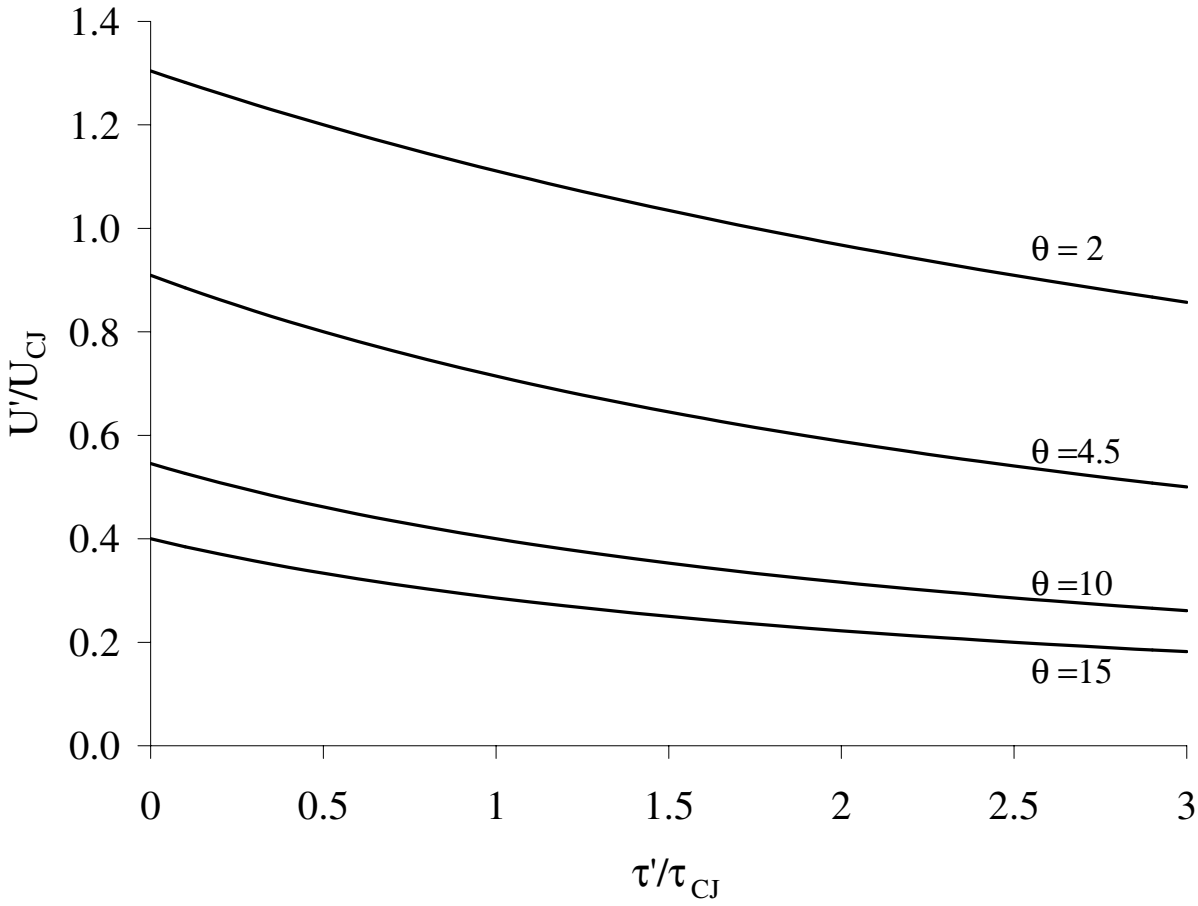

Figure 6.5: Critical decay rate model applied to form a boundary between coupled and locally decoupled detonation, Eqn 6.28. Curves for different values of the non-dimensional activation energy θ are shown. C=1.5 and A=30.

The results of the stability and decoupling analyses presented above are combined in Fig. 6.6 to delineate four regions of detonation behavior for θ= 4.5. The decoupling boundary for θ=4.5 is shown. Consider a fixed perturbation in the lead shock velocity of about 30%, corresponding to $U'/U_{CJ} = 0.3$ in Fig. 6.6. If the chemistry (or more specifically the activation energy of the mixture) is such that this perturbation in the lead shock strength results in a fluctuation in the induction time of less than 2.5 times the CJ

induction time, $\tau' \leq 2.5\tau_{CJ}$, the detonation is stable with no cellular structure. This case is not physically realistic since all laboratory experiments result in unstable fronts and stable fronts are only observed in numerical simulations. If the chemistry of the mixture is such that the response in the induction time is $2.5 \leq \tau'/\tau_{CJ} \leq 8$, a coupled detonation with cellular instability results. This is the case in marginally unstable detonation. If the normalized fluctuation in the induction time is larger, $\tau' \geq 8\tau_{CJ}$, local decoupling, or quenching, of the front, may occur. This is the case for highly unstable detonation.

As discussed in Section 5.2, the numerical results of Eckett (2000) show the lead shock fluctuation through one cell cycle is $0.3U_{CJ}$, from $1.23U_{CJ}$ to $0.91U_{CJ}$. The activation energy of the mixture used in this calculation is 5.2. The resulting induction time fluctuation may be estimated (from the equivalent to Fig. 6.4 for this mixture) to be about $2.4\tau_{CJ}$ which puts the calculation in the coupled region, very close to the stability boundary.

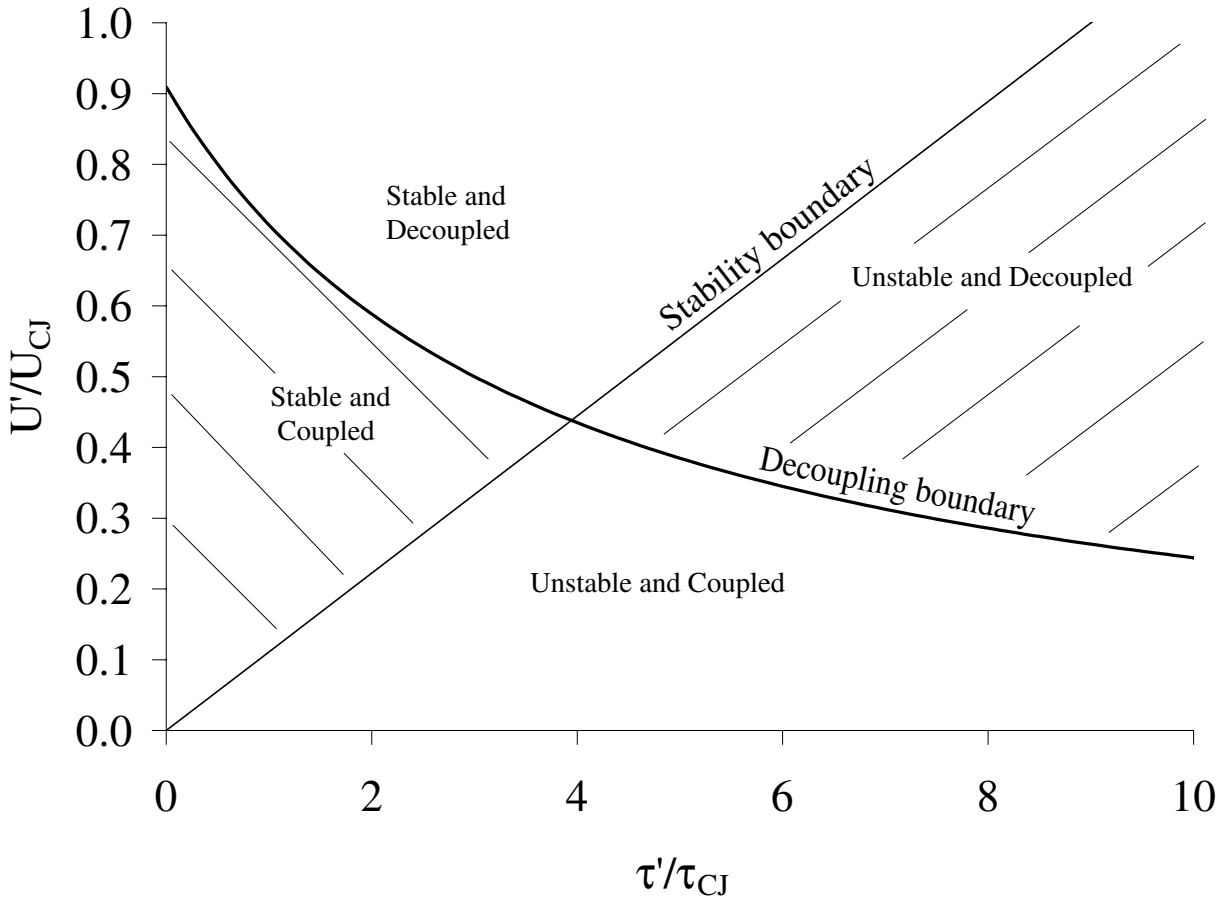

Figure 6.6: Combustion regime boundaries for detonation for θ=4.5. The axes are the magnitude of the lead shock oscillation normalized by the local average U'/U_{CJ} and the magnitude of the fluctuation in the reaction time normalized by the local average τ'/τ_{CJ}. These quantities are analogous to the axes defined in Fig. 6.1 since the fluctuation (due to the cellular instability) is about the stable or "laminar" CJ solution. Four regimes have been identified. The boundary (Eqn. 6.14) between unstable and stable detonation refers to the presence or absence of cellular instability. (Stable fronts are only observed in numerical simulations.) The boundary (Eqn. 6.28)between coupled and decoupled is determined by the decay rate of the lead shock front, as discussed in the text.

In addition, small-scale fluctuations that are evident in highly unstable detonation may be considered. Fig. 6.7 shows schematically how small scale fluctuations might be superimposed on the large scale oscillations. If it is possible to assume a slow and fast time, the model discussed above may be applied directly to the small scales with averages now taken as the local slow time value.

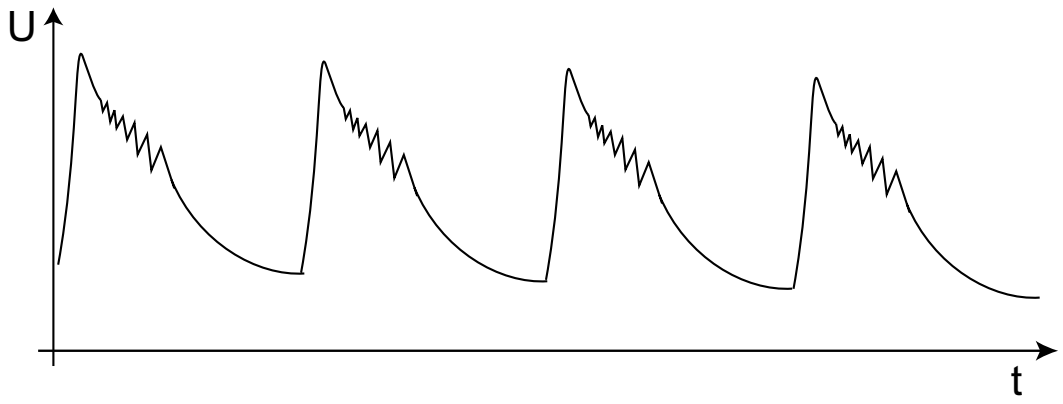

Figure 6.7: Cartoon showing small-scale fluctuations in the lead shock velocity superimposed on the large scale instability.

Chapter 7 Conclusions

This work is an experimental study of gaseous detonation structure investigating the time-dependent, instability of the lead shock front and the nature of the combustion process behind it. Non-intrusive measurements and visualizations of the shock and reaction front were made in propagating detonation waves. A range of fuel-oxidizer mixtures were studied to address differences in soot foil patterns, schlieren images, and scaling parameters (such as critical diameter) that have been previously reported in mixtures with different chemical composition.

A broad spectrum of behavior is observed. The structure of the front has traditionally been classified by the regularity of the cellular pattern observed on soot foils. Instead, we classify different mixtures by comparing calculated mixture parameters with the neutral stability curve for longitudinal oscillations of Lee and Stewart (1990). Two extreme categories are identified: weakly unstable detonation in mixtures with low activation energy and heat release resulting in states which are close to the neutral stability curve, and highly unstable detonation in mixtures with higher activation energy and heat release that are substantially further from the neutral stability curve. Very different structure is observed for detonation fronts in these two categories.

In weakly unstable detonation, one dominant length scale, the cell width, is observed in images and on soot foils. Keystone structures were observed in OH fluorescence images by Pintgen (2000) in a square (150×150) test section and are analyzed in this work. The triple point shock configuration is calculated using shock polars and combined with zero-dimensional constant volume adiabatic explosion calculations along particle paths to locate the increase in OH number density for comparison with experimental images, Fig. 7.1 (a). Shear layers form the boundary of the keystones, separating gas that has passed through the Mach stem portion of the front and reacts relatively quickly, with gas that has passed through the incident and transverse waves and reacts relatively slowly.

From the images and the analysis, we find transverse waves do not significantly accelerate combustion and have a non-essential role in the propagation of weakly unstable fronts.

The calculated keystone configurations may also be compared to experimental images from a second facility that was built for this study, Fig. 7.1 (b and c). The facility is a (high-aspect ratio) narrow channel designed to suppress or weaken the out-of-plane detonation structure so that schlieren images may be directly compared to OH fluorescence images made using PLIF (Pintgen, 2000). Fig. 7.1 (c) shows an overlaid schlieren and fluorescence image which directly shows the location and structure of the lead shock and the reaction front. Chemiluminescence is also reduced in this facility so that the current PLIF imaging technique may be used in hydrocarbon mixtures.

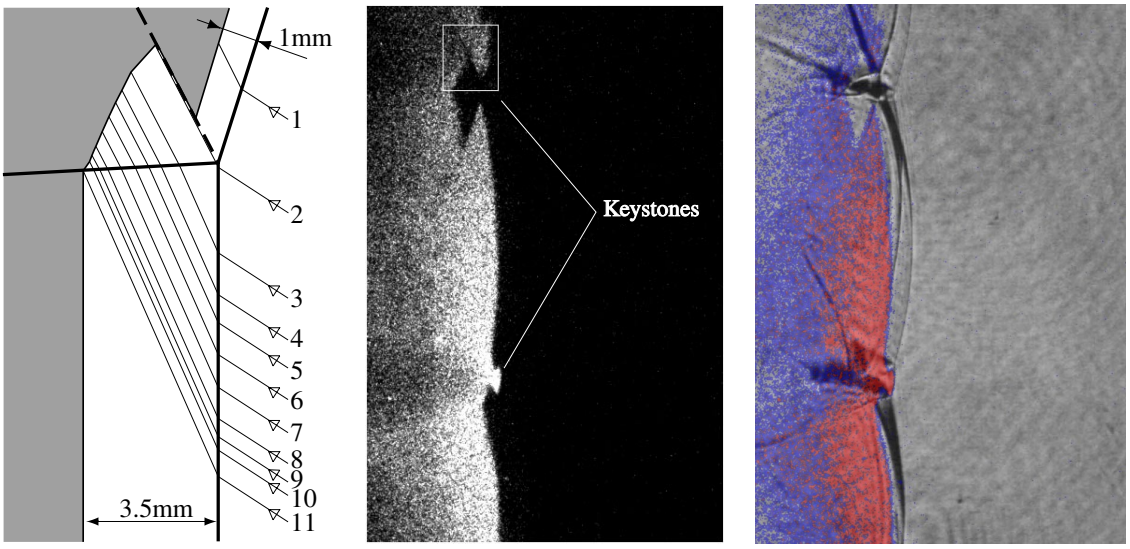

Figure 7.1: (a) Prediction of the keystone region shape in reaction zone of detonation in for $2H_2$-O_2-17Ar, from Fig. 4.5. The prediction is based on the idealized three-shock calculation using shock polars and an estimates of the OH mole fraction using zero-dimensional reaction zone models along particle paths. (b) OH fluorescence image of reaction zone in $2H_2$-O_2-17Ar (Shot nc74), showing two keystone structures at different phases in the cell cycle. Outline shows the portion of the keystone feature in (a). (c) Overlaid schlieren and fluorescence image (false color) showing the correspondence of the lead shock location and configuration with the keystones (Shot nc74). Image height for (b and c) is 60 mm. Detonation is propagating left to right in all cases.

Substantially different structure is observed in highly unstable detonation. As reported by previous researchers, soot foils show cellular structure over a large range of scales in these fronts and schlieren images show a more irregular lead shock front with larger spatial oscillations. From shadowgraph movies made in the present study, we measure the magnitude of the temporal oscillation of the lead shock velocity through the cell cycle. The lead shock velocity decreases from U=1.42U_{CJ} at the beginning of the cell to $U = 0.69U_{CJ}$ at the end of the cell in a sample highly unstable detonation in C_3H_8-5O_2-9N_2. The magnitude of the oscillation, $0.73U_{CJ}$, is about 4 times the value measured in a weakly unstable detonation in 2H_2-O_2-17Ar.

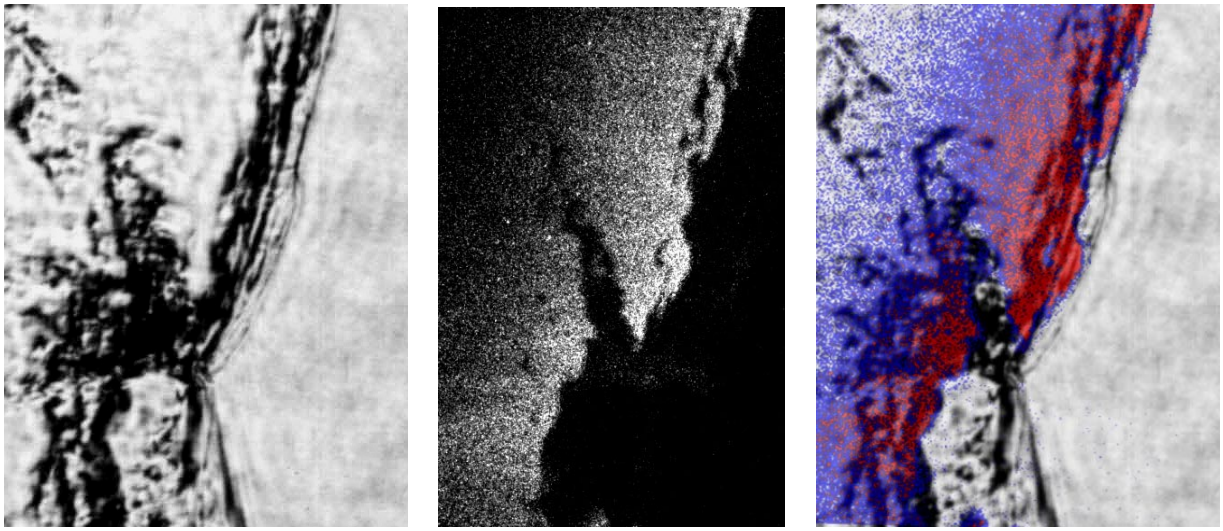

(a) (b) (c)

Figure 7.2: Images of highly unstable detonation front in C_2H_4-3O_2-10.5N_2, P_1=20 kPa. (a) schlieren image (b) OH fluorescence image (c) overlay of (a) and (b) in false color (Shot nc175). Detonation propagated left to right. Image height is 30 mm.

The effect of the oscillation in lead shock strength through one cell cycle on the coupling between the shock and the reaction was investigated using the critical decay rate (CDR) model of Eckett et al. (2000). The CDR model was developed for study of detonation initiation by a decaying spherical shock wave. We make an analogy with the decaying lead shock velocity along the centerline in a cell cycle. Using velocity data from

numerical simulations by Gamezo et al. (1999b), we show that the CDR model predicts decoupling of the lead shock from the reaction, or local quenching of the detonation near the end of the cell, for a mixture with non-dimensional activation energy θ=7.4 but not for θ=4.9. Decoupling is also inferred from experimental images of highly unstable detonations, which show substantial oscillations in the location of the reaction behind a smooth lead shock.

Contrasting with the collision process in weakly unstable fronts, localized explosions are observed at the beginning of a new cell cycle in highly unstable fronts, with a blast wave propagating back into the combustion products.

In N_2-diluted stoichiometric H_2-O_2 mixtures, the portion of the shear layer that separates reacted and unreacted gas is sometimes observed to become unstable, resulting in Kelvin-Helmholtz type features (vortex "rollers") rolled up in the direction of the slower, reacted, stream behind the Mach stem. In C_3H_8-O_2-N_2 mixtures, local "hot spots" or regions of intense luminescence are observed in chemiluminesence images of the front. Comparison with the corresponding schlieren images shows the hot spots occur in the shear layer near the end of the cell cycle, but before the triple point collision. This release of energy may possibly contribute to the re-ignition process at the end of the cell - a "turbulent" combustion mechanism that is not included in traditional detonation models based on shock-induced explosion.

Soot foils and schlieren images from previous researchers and the present study show structure over a large range of scales in mixtures with high activation energy. OH fluorescence images from the present study show the reaction front appears very rough and wrinkled with isolated small scale regions of low fluorescence intensity. We show that a larger range of scales of cellular instability results from the stronger dependence of the induction time on lead shock strength. The instability properties (Short and Stewart, 1998) of mixtures with high activation energy suggest that a broad spectrum of disturbance wave lengths can be amplified over a large range of overdrives. These factors may explain the large range of cell sizes and cellular substructure in these cases.

We consider a statistical description of the fluctuations in the front, and estimate

small-scale fluctuations for highly unstable mixtures to be about 20% of the local lead shock velocity, and small-scale fluctuations in the induction time to be about 2.5 times the local induction time.

A detonation regime diagram is proposed, similar in concept to the Borghi diagram in premixed turbulent combustion. The axes are the magnitude of the lead shock oscillation normalized by the local average U'/U_{CJ} and the magnitude of the fluctuation in the reaction time normalized by the local average τ'/τ_{CJ}. These quantities are analogous to the axes defined in the Broghi diagram (Fig. 6.1) since the fluctuation due to the cellular instability is about the stable or "laminar" CJ solution. We propose two boundaries: stable and unstable, and coupled and decoupled, forming four regions. The boundary between stable and unstable is given by the calculated relation between lead shock velocity U and induction time τ using a constant volume explosion assumption for a particle behind the lead shock. The U-τ relation for an activation energy of 4.5 is selected as the boundary since this value of the activation energy corresponds to the asymptote of the neutral stability curve of Lee and Stewart (1990). The boundary between coupled and decoupled detonation is given by recasting the CDR model in the appropriate coordinates.

7.1 Future Work

An important issue that remains to be addressed is: what is the nature of the small-scale structure and what role, if any, does it play in the propagation of highly unstable detonation. In particular, can the observed macroscopic differences in scaling of parameters such as the critical initiation energy, critical diffraction diameter etc. be explained by the presence of this structure.

To address these issues, the statistical description of the spatial and temporal fluctuations of the front could be extended, firstly over a larger range of sample sizes and images. The possibility of separation of scales between the dominant length scale and substructure could be investigated and potentially exploited.

Bibliography

Akbar, R. (1997, August). *Mach Reflection of Gaseous Detonations*. Ph. D. thesis, Rensselaer Polytechnic Institute, Troy, New York.

Akbar, R., M. J. Kaneshige, E. Schultz, and J. E. Shepherd (1997). Detonations in H_2-N_2O-CH_4-NH_3-O_2-N_2 mixtures. Technical Report FM97-3, Graduate Aeronautical Laboratories: California Institute of Technology.

Andresen, P., W. Reckers, H. G. Wagner, E. K. Dabora, and H. Voges (1992). The structure of gaseous detonations as revealed by laser-induced fluorescence of the OH-radical. *Zeitschrift fur Physicalische Chemie Neue Folge 175*, 129–143.

Arienti, M. (2003, January). *A Numerical and Analytical Study of Detonation Diffraction*. Ph. D. thesis, California Institute of Technology, Pasadena, California.

Barthel, H. (1972). Reaction zone-shock front coupling in detonations. *Phys. Fluids 15*(1), 43–50.

Chapman, D. L. (1899). On the rate of explosion in gases. *Philos. Mag. 47*, 90–104.

Deiterding, R. (2003). *Parallel Adaptive Simulation of Multi-Dimensional Detonation Dtructures*. Ph. D. thesis, Brandenburgischen Technischen Universität Cottbus, Germany.

Denisov, Y. N. and Y. K. Troshin (1959). Pulsating and spinning detonation of gaseous mixtures in tubes. *Dokl. Akad. Nauk. 125*, 110–113.

Desbordes, D. (1988). Transmission of overdriven plane detonations: critical diameter as a function of cell regularity and size. *Prog. Astronaut. Aeronaut. 114*, 170–185.

Döring, W. (1943). On detonation processes in gases. *Ann. Phys. 43*, 421–436.

Dormal, M., J. C. Libouton, and P. Van Tiggelen (1979). Evolution of induction time in detonation cells. *Acta Astronautica 6*(1), 875–88.

DuPre, G., O. Peraldi, J. H. Lee, and R. Knystautas (1988). Propagation of detonation waves in an acoustic walled tube. *Prog. Astronaut. Aeronaut. 114*, 248–263.

Eckett, C. A. (2000, September). *Numerical and Analytical Studies of the Dynamics of Gaseous Detonations*. Ph. D. thesis, California Institute of Technology, Pasadena, California.

Eckett, C. A., J. J. Quirk, and J. E. Shepherd (2000). The role of unsteadiness in direct initiation of gaseous detonation. *J. Fluid Mechanics 421*, 147–183.

Eder, A. (2001, January). *Brennerverhalten schnallnaher und überschall-schneller Wasserstoff-Luft Flammen*. Ph. D. thesis, Technische Universität München, Munich, Germany.

Edwards, D. H., G. Hooper, and R. J. Meddins (1972). Instabilities in the reaction zones of detonation waves. *Astronautica Acta 17*(4-5), 475–485.

Erpenbeck, J. J. (1964). Stability of idealized one-reaction detonations. *Phys. Fluids 7*, 684–696.

Fay, J. A. (1959). Two-dimensional gaseous detonations: velocity deficit. *Phys. Fluids. 2*(1), 283–289.

Gamezo, V. N., D. Desbordes, and E. S. Oran (1999a). Formation and evolution of two-dimensional cellular detonations. *Combust. Flame 116*, 154–165.

Gamezo, V. N., D. Desbordes, and E. S. Oran (1999b). Two-dimensional reactive flow dynamics in cellular detonation waves. *Shock Waves 9*, 11–17.

Gerlach, C. (1996, December). *Laseroptische Unersuchung der Wechselwirkung von Turbulenz und Reaktionskinetik in turbulent reagierenden Strömungen*. Diplom Arbeit, Technische Universität München, Munich, Germany.

Gooderum, P. B. (1958). Technical Report 4243, NACA.

Hidaka, Y., H. Takuma, and M. Suga (1985a). Shock-tube studies of N_2O decomposition and N_2O-H_2 reaction. *Bull. Chem. Soc. Japan 58*(10), 2911–2916.

Hidaka, Y., H. Takuma, and M. Suga (1985b). Shock-tube study of the rate constant for excited $OH^*(^2\sigma^+)$ formation in the N_2O-H_2 reaction. *J. Phys. Chem. 89*(23), 4903–4905.

Huang, Z., M. Lefebvre, and P. Van Tiggelen (2000). Experiments on spinning detonations with detailed analysis of the shock structure. *Shock Waves 10*(2), 119–125.

Inaba, K. and A. Matsuo (2001). Cellular structure of planar detonations with a detailed chemical reaction model. *AIAA 10*.

Inaba, K., A. Matsuo, K. Tanaka, A. K. W. Lam, F. Pintgen, E. Wintenberger, and J. E. Shepherd (2002). Soot track generation by Mach reflection over a wedge. *Japanese Symp. Shock Waves, Ibarki, Japan, March 14-16*.

Jackson, S. I. and J. E. Shepherd (2002, July 7-10). Initiation systems for pulse detonation engines. Technical Report AIAA 2002-3627, 38th AIAA/ASME/SAE/ASEE Joint Propulsion Conference, Indianapolis, IN.

Jouguet, E. (1905). On the propagation of chemical reactions in gases. *J. de Mathematiques Pures et Appliquees 1*, 347.

Kaneshige, M. J. (1999, January). *Gaseous Detonation Initiation and Stabilization by Hypervelocity Projectiles*. Ph. D. thesis, California Institute of Technology, Pasadena, California.

Kee, R., F. Rupley, and J. Miller (1989). Technical Report SAND89-8009, Sandia National Laboratory.

Khoklov, A. (2003). *Personal Communication*.

Konnov, A. (1998). Detailed reaction mechanism for small hydrocarbon combustion. release 4.0. *http://homepages.vub.ac.be/ akonnov*.

Law, C. K. and I. I. Glass (1971). Diffraction of strong shock waves by a sharp compressive corner. *C.A.S.I. Transactions 4*(1), 2–12.

Lee, H. I. and D. S. Stewart (1990). Calculation of linear detonation instability: one-dimensional instability of plane detonation. *J. Fluid Mech. 216*, 103–132.

Lee, J. H. (1991). Dynamic structure of gaseous detonation. In *Fluid Mechanics and its Applications v.5 Dynamic structure of detonation in gaseous and dispersed media*, Netherlands, pp. 1. Kluwer Academic Publishers.

Lee, J. H. S. (1984). *Ann. Rev. Fluid Mech. 16*, 311–316.

Lefebvre, M. H. and E. S. Oran (1995). Analysis of the shock structures in a regular detonation. *Shock Waves 4*, 277–283.

Libouton, J. C., A. Jacques, and P. Van Tiggelen (1981). Cinétique, structure et entretien des ondes de détonation. *Actes du Colloque International Berthelot-Vieille-Mallard-Le Chatelier 2*, 437–442. Bordeaux.

Liu, W. S., X. X. Du, and I. I. Glass (1983). Laminar boundary layers behind detontion waves. *Proc. Roy. Soc. A 387*, 331–349.

Lundstrom, E. A. and A. K. Oppenheim (1969). On the influence of non-steadiness on the thickness of the detonation wave. *Proc. Roy. Soc. A 310*, 463–478.

Manzhalei, V. I. (1977). Fine structure of the leading front of a gaseous detonation. *Fizika Goreniya i Vzryva 13*(3), 470–472.

Moen, I. O., J. W. Funk, S. A. Ward, G. M. Rude, and P. A. Thibault (1984). Detonation length scales for fuel-air explosives. *Prog. Aeronaut. Astronaut. 94*, 55–79.

Moen, I. O., A. Sulmistras, G. O. Thomas, D. Bjerketvedt, and P. A. Thibault (1986). Influence of cellular regularity on the behavior of gaseous detonation. *Prog. Astronaut. Aeronaut. 106*, 220–243.

Mueller, M. A., R. A. Yetter, and F. L. Dryer (2000). Kinetic modeling of the $CO/H_2O/O_2/NO/SO_2$ system: Implications for high-pressure fall-off in the SO_2+O(+M)=SO_3(+M) reaction. *Int. J. Chem. Kinetics 32*(6), 317–339.

Murray, S. B. (1985). *The influence of initial and boundary conditions on gaseous detonation waves*. Ph. D. thesis, McGill University, Montreal, Canada.

Nagaishi, T., K. Yoneda, and T. Hikita (1971). On the structure of detonation waves in gases. *Combust. Flame 16*(1), 35–38.

Oppenheim, A., J. Smolen, and L. Zajac (1968). Vector polar method for the analysis of wave intersections. *Combust. Flame 12*, 63–76.

Oran, E. S., J. W. Weber Jr., E. I. Stefaniw, M. H. Lefebvre, and J. D. Anderson Jr. (1998). A numerical study of a two-dimensional H_2-O_2-Ar detonation using a detailed chemical reaction model. *Combust. Flame 113*, 147–163.

Oran, E. S., T. R. Young, J. P. Boris, J. P. Picone, and D. H. Edwards (1982). A study of detonation structure: The formation of unreacted gas pockets. In *19th Symposium (International) on Combustion*, Pittsburgh, PA, pp. 573–582. The Combustion Institute.

Pamidimukkala, K. and G. Skinner (1982). Resonance absorption measurements of atom concentration in reacting gas mixtures. VIII Rate constants for O+H_2=OH+H and O+D_2=OD+D from measurements of O atoms in oxidation in H_2 and D_2 by N_2O. *J. Phys. Chem. 76*(1), 311–315.

Peters, N. (2000). *Turbulent Combustion*. Cambridge University Press.

Pintgen, F. (2000, December). *Laser-Optical Visualization of Detonation Structures*. Diplom Arbeit, Lehrstuhl für Thermodynamik: Technische Universität München / Graduate Aeronautical Laboratories: California Institute of Technology.

Pintgen, F., C. A. Eckett, J. M. Austin, and J. E. Shepherd (2003). Direct observations of reaction zone structure in propagating detonations. *Combust. Flame (in press)*.

Pintgen, F. and J. E. Shepherd (July 27 - August 1, 2003). Simultaneous soot foil and PLIF imaging of propagating detonations. *19th ICDERS, Hakone, Japan*.

Quirk, J. J. (1998). (i) Amrita: A computational facility (for CFD modelling), (ii) Amr_sol: Design principles and practice. In H. Deconinck (Ed.), 29$^{\text{th}}$ *Computational Fluid Dynamics lecture series*. von Karman Institute. `http://www.amrita-cfd.org/doc`.

Radulescu, M. I. and J. H. S. Lee (2002). The failure mechanism of gaseous detonations: Experiments in porous wall tubes. *Combust. Flame 131*(1-2), 29–46.

Reynolds, W. C. (1986, January). The element potential for chemical equilibrium analysis: implementation in the interactive program STANJAN. Technical Report A-3991, Dept. of Mechanical Engineering, Stanford University, Stanford, CA.

Schott, G. L. (1965). Observations of the structure of spinning detonation. *Phys. Fluids 8*(5), 850–865.

Schultz, E. (2000, April). *Detonation Diffraction Through an Abrupt Area Expansion*. Ph. D. thesis, California Institute of Technology, Pasadena, California.

Schultz, E. and J. E. Shepherd (2000). Validation of detailed reaction mechanisms for detonation simulation. Technical Report FM99-5, Graduate Aeronautical Laboratories: California Institute of Technology.

Sharpe, G. J. (2001). Transverse waves in numerical simulations of cellular detonations. *J. Fluid Mech. 447*, 31–51.

Shchelkin, K. and Y. Troshin (1964). *Gasdynamics of Combustion*. English Translation NASA-TT-F-23.

Shchelkin, K. I. (1959). Two cases of unstable combustion. *Soviet Phys. JETP 36*(9), 416–420.

Shepherd, J. E. (1986). The chemical kinetics of hydrogen-air-diluent detonations. *Prog. Astronaut. Aeronaut. 106*, 263–293.

Shepherd, J. E. (1994). Detonation waves and propulsion. In *Combustion in High-Speed Flows*, pp. 373–420. Kluwer Academic Publishers.

Shepherd, J. E., I. O. Moen, S. B. Murray, and P. A. Thibault (1986). Analysis of the cellular structure of detonations. *21st Symp. (Int.) Combust.*, 1649–1657.

Short, M. and J. J. Quirk (1997). On the nonlinear stability and detonability limit of a detonation wave for a model three-step chain-branching reaction. *J. Fluid Mech. 339*, 89–119.

Short, M. and D. S. Stewart (1998). Cellular detonation stability. Part 1. A normal-mode linear analysis. *J. Fluid Mech. 368*, 229–262.

Strehlow, R. (1969). The natue of transverse waves in detonations. *Astronautica Acta 14*, 539–548.

Strehlow, R. and A. Crooker (1974). The structure of marginal detonation waves. *Acta Astronautica 1*, 303–315.

Strehlow, R. A. (1964). Reactive gas mach stems. *Phys. Fluids 7*, 908–9.

Strehlow, R. A. and J. R. Biller (1969). On the strength of transverse waves in gaseous detonations. *Combust. Flame 13*, 577–582.

Strehlow, R. A. and R. J. Salm (1976). The failure of marginal detonations in expanding channels. *Acta Atronaut. 3*, 983–993.

Subbotin, V. (1975). Two kinds of transverse wave structures in multi-front detonation. *Fizika Goreniya i Vzryva 11*(1), 96–102.

Takai, R., K. Yoneda, and T. Hikita (1974). Study of detonation wave structure. In *15th Symposium (International) on Combustion*, Pittsburgh, PA, pp. 69–78. The Combustion Institute.

Thibault, P., J. Penrose, J. Shepherd, W. Benedick, and D. Ritzel (1987). *Shock Tubes and Waves*, 765–771.

Tieszen, S., D. Stamps, C. Westbrook, and W. Pitz (1991). Gaseous hydrocarbon-air detonations. *Combust. Flame 84*, 376–390.

Ul'yanitskii, V. Y. (1981). *Fizika Goreniya i Vzryva 17*, 227.

Urtiew, P. A. (1970). Reflections of wave intersections in marginal detonations. *Astronautica Acta 15*, 335–343.

Urtiew, P. A. (1976). Idealized two-dimensional detonation waves in gaseous mixtures. *Acta Astronautica 3*, 187–200.

Urtiew, P. A. and A. K. Oppenheim (1966). Experimental observations of transition to detonation in an explosive gas. *Proc. Royal Soc. A 295*, 13.

Vasiliev, A. A. and Y. Nikolaev (1978). Closed theoretical model of a detonation cell. *Acta Astronaut. 5*, 983–996.

Voitsekhovskii, B. V., V. V. Mitrofanov, and M. E. Topchian (1963). Struktura fronta detonastii i gaza. *Akad. Nauk., SSSR, Novosibirsk*. Translation: The structure of a detonation front in gases Rep. FTD-MT-64-527, Foreign Technology Division, Wright-Patterson A.F.B., Ohio,(1966).

von Neumann, J. (1942). *John von Neumann, collected works. Vol. 6., ed. A. J. Taub. New York: Macmillan*.

Warnatz, J. and V. Karbach (1997). C2 mechanism for methane-air combustion. *http://www.ca.sandia.gov/tdf/3rdWorkshop/ch4mech.html*.

Westbrook, C. K. (1982). Chemical-kinetics of hydrocarbon oxidation in gaseous detonation. *Combust. Flame 46*, 191–210.

White, D. (1961). Turbulent structure of gaseous detonation. *Phys. Fluids 4*, 465–480.

White, D. and K. Cary (1963). Structure of gaseous detonation. II Generation of laminar detonation. *Phys. Fluids 6*, 749–750.

Wolanski, P., C. W. Kauffman, M. Sichel, and J. A. Nicholls (1981). Detonation in methane-air mixtures. *18th Symp. (Int.) Combust.*, 1651–1660.

Zel'dovich, Y. B. (1940). On the theory of the propagation of detonation in gaseous systems. *Zh. Eksp. Teor. Fiz. 10*(542-568).

Appendix B Triple Point Calculation

A shock polar is a locus of solutions across an oblique shock wave. The pressure jump across an oblique shock at angle β to the flow direction is given by

$$\frac{P_2}{P_1} = 1 + \frac{2\gamma_1}{\gamma_1 + 1}\left(M_1^2 \sin^2 \beta - 1\right) \tag{B.1}$$

where P is the pressure, M_1 is the shock Mach number, and states 1 and 2 are upstream and downstream of the shock respectively. We assume a perfect gas and take the ratio of specific heats to be that of the reactants, γ_1. The flow deflection, θ, can be expressed as function of the same parameters by manipulating the shock jump equations.

$$\tan\ \theta = \frac{M_1^2 \sin^2 \beta - 1}{\tan\ \beta\left(\frac{\gamma_1+1}{2} M_1^2 - M_1^2 \sin^2 \beta + 1\right)} \tag{B.2}$$

A triple point consists of three intersecting shock waves and a contact surface, see Fig. B.1 (a). The nomenclature for shock reflexion is commonly used to identify the three waves: the incident wave (which in detonation corresponds to the portion of the lead shock at the end of the cell), the Mach stem (the portion of the lead shock at the beginning of the neighboring cell) and the reflected (or transerve) wave. Shock polars may be used to calculate local wave angles, flow deflection, and shock strengths for the triple point. As the pressure, P, and flow deflection, θ, are matched across the contact surface, it is convenient to express the triple point calculation in the P-θ plane, as shown in Fig. B.1 (b), using Equations B.1 and B.2 with β as an implicit parameter which varies from $\pi/2$ to the Mach angle.

The local triple point analysis assumes the flow is steady in the frame of the triple point and the waves are straight in the vicinity of the triple point. This assumption is more valid for a nonreactive flow than reactive, and a probable effect of the chemistry

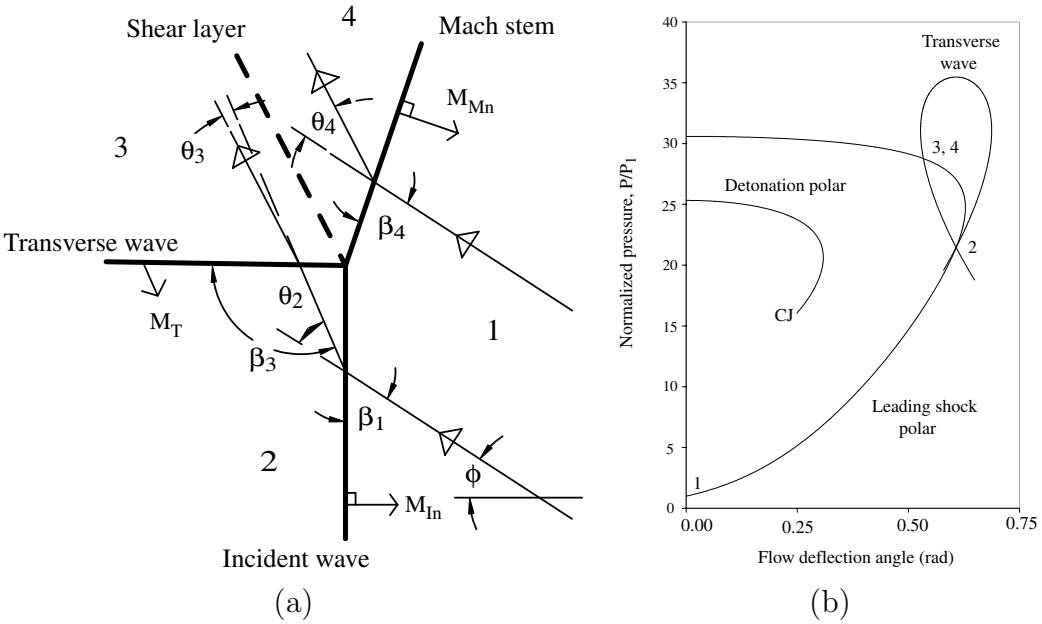

Figure B.1: (a) Geometry and nomenclature for three shock intersection showing triple point, incident wave, Mach stem, transverse or reflected wave, and contact surface. (b) Shock and detonation polars for stoichiometric hydrogen–oxygen mixture diluted with 70% argon, initial pressure 6.67 kPa, $x - x_o$= 0.91L, ϕ=33°. This calulation is used to produce the configuration shown in (a).

will be to produce some wave curvature in the vicinity of the triple point.

Two inputs are required to close the system; we choose the incident wave velocity and shock angle. In the analysis discussed in the main text in Section 4.1.1, the incident wave velocity is obtained from two-dimensional numerical simulations by Eckett (2000). The incident wave velocity is a function of the location of the lead shock through the cell cycle. If the analysis is done for comparison with a particular experimental image, the location through the cell cycle is estimated from the measured length of the Mach stem and incident wave portions of the front in the image. The second input, the angle of the incident wave to the flow, β_1, is assumed to be $\pi/2 - \phi$ where ϕ is the track angle, or the angle of the cellular pattern observed on soot foils. The analysis is sensitive to this parameter, and an analysis of the implications of this is contained in the main text, Section 4.1.1.

An example of a triple point solution is depicted graphically in Fig. B.1 (b). A shock polar locus is drawn for the lead shock of given Mach number (this is the first input). The post-shock state behind the incident wave, state 2, is found along this polar given the value of the shock angle, β_1 (the second input). A second polar is then calculated for the transverse wave, originating at state 2. The intersection of the lead shock and transverse wave polars is found to give states 3 and 4 which are equivalent in the P-θ plane. The value of β along the transverse polar at the intersection is β_3, the value of β along the lead shock polar at the intersection is β_4.

A detonation polar (Shepherd, 1994) is a locus of solutions possible for an oblique detonation which is overdriven at shock angles greater than that corresponding to the CJ wave. No solution exists for waves at Mach number less than the CJ value. A two-gamma model is used to model the variation in thermodynamic properties between the reactants and products. Manipulation of the conservation equations across a control volume containing the detonation gives

$$\frac{P_2}{P_1} = \frac{1+\gamma_1 M_1^2 \sin^2\beta}{1+\gamma_2 M_{2n}^2} \tag{B.3}$$

$$\tan\ \theta = \frac{P_2/P_1 - 1}{\gamma_1 M_1^2 \tan\ \beta \left(1 - \frac{P_2/P_1 - 1}{\gamma_1 M_1^2}\right)} \tag{B.4}$$

where

$$M_{2n}^2 = \frac{2\gamma_2 A - 1 + \sqrt{1 - 2A - 2\gamma_2 A}}{\gamma_2 - 1 - 2A\gamma_2^2} \tag{B.5}$$

$$A = \gamma_1(\gamma_2 - 1) M_1^2 \sin^2\beta \left(\frac{Q + \gamma_1 \left(1 + \frac{\gamma_1 - 1}{2} M_1^2 \sin^2\beta\right)}{\gamma_2^2 \left(1 + \gamma_1 M_1^2 \sin^2\beta\right)^2} \right) \tag{B.6}$$

In the mixtures considered in this study, there is no intersection of the transverse wave polar and the lead wave detonation polar, and no detonation polar exists for the transverse wave. Therefore only unreactive solutions are found.

Appendix C Mixture Parameters

A list of mixtures included in this study together with some calculated mixture parameters is shown in Tabs. C.1 and C.2. P_1 is the initial pressure. The next seven parameters are calculated using STANJAN (Reynolds, 1986): γ_1 and γ_2 are the specific heat ratio for the reactants and products respectively, c_1 is the initial sound speed, P_{vN} and T_{vN} are the post-shock pressure and temperature, and U_{CJ} is the Chapman-Jouguet velocity. Q is the non-dimensional chemical energy calculated as discussed in Section 1.3.1. M_{CJ} is the Chapman-Jouguet Mach number, $M_{CJ} = U_{CJ}/c_1$, Δ is the ZND induction length calculated as described in Section 1.3.2 using the detailed mechanism of Konnov (1998) for all mixtures except thos containing N_2O when the Mueller et al. (2000) mechanism was used. θ is the non-dimensional activation energy, calculated as shown in Section 1.3.3 using three different mechanisms.

Mixture	P_1 kPa	γ_1	γ_2	MW	c_1 m/s	P_{vN} Pa	T_{vN} K	U_{CJ} m/s	Q
$2H_2$-O_2-20Ar	20	1.63	1.46	36.3	333.0	4.11E+05	1687.0	1356.9	11.25
$2H_2$-O_2-17Ar	20	1.62	1.40	35.8	334.7	4.11E+05	1775.3	1415.0	14.73
$2H_2$-O_2-12Ar	20	1.60	1.29	34.4	339.4	4.95E+05	1899.3	1517.9	24.21
$2H_2$-O_2-7Ar	6.67	1.57	1.20	31.6	350.2	1.76E+05	1903.9	1618.3	38.68
$2H_2$-O_2-3.5N_2	20	1.39	1.16	20.6	410.0	5.40E+05	1501.4	1958.0	45.30
$2H_2$-O_2-4.5N_2	20	1.41	1.17	21.6	400.6	4.52E+05	1454.7	1874.3	41.60
$2H_2$-O_2-5.6N_2	20	1.41	1.19	22.4	393.2	4.93E+05	1403.2	1796.6	36.30
$2H_2$-O_2-8N_2	20	1.39	1.23	23.6	382.9	4.40E+05	1290.5	1653.8	25.21
$2H_2$-O_2-9N_2	20	1.39	1.24	24.0	380.0	4.18E+05	1245.1	1601.6	22.14
$2H_2$-O_2-CO_2	20	1.35	1.15	20.0	410.7	5.40E+05	1342.9	1964.7	47.66
H_2-N_2O-3N_2	20	1.36	1.19	26.0	360.6	6.00E+05	1470.6	1815.4	41.05
H_2-N_2O-2N_2	30.4	1.35	1.17	25.5	363.1	1.03E+06	1554.3	1925.5	50.38
H_2-0.75N_2O-0.125O_2-2.25N_2	13.3	1.36	1.17	24.7	370.1	4.11E+05	1516.9	1891.1	46.61
H_2-0.5N_2O-0.25O_2-2.5N_2	11.3	1.37	1.18	24.0	377.1	3.23E+05	1476.4	1854.2	42.39
H_2-0.25N_2O-0.375O_2-2.75N_2	12.4	1.38	1.18	23.3	384.1	3.28E+05	1432.5	1814.4	38.32
H_2-0.5O_2-3N_2	17.7	1.39	1.19	22.7	391.0	4.30E+05	1384.2	1770.8	33.83
H_2-N_2O-1.33N_2	20	1.34	1.17	25.0	365.9	7.19E+05	1613.7	2017.5	55.19
H_2-N_2O-1.64N_2	20	1.35	1.17	25.3	364.4	6.92E+05	1585.6	1972.3	53.13
H_2-N_2O-1.77N_2	20	1.35	1.17	25.4	363.9	6.83E+05	1574.3	1954.7	52.15
C_2H_4-3O_2-5N_2	20	1.36	1.17	29.4	339.7	8.05E+05	1711.3	1965.0	62.27
C_2H_4-3O_2-6N_2	20	1.36	1.16	29.2	340.9	7.71E+05	1681.2	1929.6	61.32
C_2H_4-3O_2-8N_2	20	1.27	1.16	27.0	342.6	7.15E+05	1627.4	1870.0	53.66
C_2H_4-3O_2-10.5N_2	20	1.37	1.16	28.8	344.2	6.88E+05	1613.5	1844.1	56.89
C_3H_8-5O_2-9N_2	20	1.34	1.16	30.4	331.0	8.15E+05	1643.7	1934.4	65.33
C_3H_8-5O_2-10.5N_2	20	1.34	1.16	30.2	332.8	7.81E+05	1620.0	1903.3	63.68

Table C.1: List of mixtures studied together with calculated parameters.

Mixture	M_{CJ}	Δ mm	θ (Konnov)	θ (Warnatz)	θ (Dryer)
$2H_2$-O_2-20Ar	4.08	1.98	5.7	5.5	
$2H_2$-O_2-17Ar	4.23	1.33	5.4	5.3	
$2H_2$-O_2-12Ar	4.47	0.72	5.2	5.1	
$2H_2$-O_2-7Ar	4.62	1.2	5.3	5.2	
$2H_2$-O_2-3.5N_2	4.78	0.72	6.2	6.2	
$2H_2$-O_2-4.5N_2	4.68	0.99	6.5	6.4	
$2H_2$-O_2-5.6N_2	4.57	1.39	6.9	6.8	
$2H_2$-O_2-8N_2	4.32	3.06	8.3	7.8	
$2H_2$-O_2-9N_2	4.22	4.31	9.3	8.5	
$2H_2$-O_2-CO_2	4.78	0.93	10.1	9.4	
H_2-N_2O-3N_2	5.04	7.5			12.7
H_2-N_2O-2N_2	5.30	2.0			11.9
H_2-0.75N_2O-0.125O_2-2.25N_2	5.11	2.0			7.4
H_2-0.5N_2O-0.25O_2-2.5N_2	4.92	2.0			7.1
H_2-0.25N_2O-0.375O_2-2.75N_2	4.72	2.0			7.1
H_2-0.5O_2-3N_2	4.53	2.0			7.1
H_2-N_2O-1.33N_2	5.52	1.5			11.1
H_2-N_2O-1.64N_2	5.41	2.1			11.4
H_2-N_2O-1.77N_2	5.37	2.3			11.5
C_2H_4-3O_2-5N_2	5.79	1.0	5.6	11.4	
C_2H_4-3O_2-6N_2	5.66	1.24	5.9	11.7	
C_2H_4-3O_2-8N_2	5.46	2.6	6.9	12.4	
C_2H_4-3O_2-10.5N_2	5.36	3.2	7.2	12.1	
C_3H_8-5O_2-9N_2	5.84	1.7	12.7		
C_3H_8-5O_2-10.5N_2	5.72	2.25	12.9		

Table C.2: List of mixtures studied together with calculated parameters.

Appendix D Narrow Channel Shot List

shot no	Mixture	PLIF	FOV	Schlieren	Framer	Chem.	Soot foil
33	CH_4-$2O_2$-$2N_2$			yes			
37	$2H_2$-O_2-$4.5N_2$						yes
38	$2H_2$-O_2-17Ar						yes
39	$2H_2$-O_2-12Ar						yes
42	H_2-N_2O-$0.86N_2$						yes
43	H_2-N_2O-$1.33N_2$						yes
44	H_2-N_2O-$1.77N_2$						yes
45	$2H_2$-O_2-CO_2						yes
46	$2H_2$-O_2-$5.6N_2$						yes
47	C_3H_8-$5O_2$-$9N_2$						yes
48	C_3H_8-$5O_2$-$10.5N_2$						yes
49	C_2H_4-$3O_2$-$5N_2$						yes
50	C_2H_4-$3O_2$-$9N_2$						yes
51	$2H_2$-O_2-$3.5N_2$						yes
52	$2H_2$-O_2-$1.33N_2$						yes
53	$2H_2$-O_2-7Ar						yes
62	$2H_2$-O_2-12Ar	yes	60				
64	$2H_2$-O_2-12Ar	yes	60				
65	$2H_2$-O_2-12Ar	yes	60				
66	$2H_2$-O_2-12Ar	yes	60				
67	$2H_2$-O_2-$3.5N_2$	yes	60				
68	$2H_2$-O_2-$4.5N_2$	yes	60				
69	C_2H_4-$3O_2$-$6N_2$	yes	60				
70	$2H_2$-O_2-12Ar	yes	60				
71	$2H_2$-O_2-12Ar	yes	60				
72	$2H_2$-O_2-12Ar	yes	60	yes			
73	$2H_2$-O_2-12Ar	yes	60	yes			
74	$2H_2$-O_2-12Ar	yes	60	yes			
75	$2H_2$-O_2-12Ar	yes	60				
76	$2H_2$-O_2-12Ar	yes	60	yes			
77	$2H_2$-O_2-12Ar	yes	60	yes			
78	$2H_2$-O_2-17Ar	yes	60				
79	$2H_2$-O_2-17Ar	yes	60	yes			
80	$2H_2$-O_2-17Ar	yes	60	yes			
81	$2H_2$-O_2-17Ar	yes	60	yes			
82	$2H_2$-O_2-17Ar	yes	60	yes			
83	$2H_2$-O_2-17Ar	yes	60	yes			
85	C_2H_4-O_2-$9N_2$	yes	60	yes			
86	C_2H_4-$O_2$10.5N_2	yes	60	yes			
87	C_2H_4-O_2-$10.5N_2$	yes	60	yes			
88	$2H_2$-O_2-$4.5N_2$	yes	60				

Table D.1: Narrow channel experiments. FOV is the height of the PLIF or chemiluminescence (Chem.) image. The field of view of schlieren images was about 146 mm and of framing camera images was about 138 mm. Initial pressure is 20 kPa unless otherwise noted, initial temperature is 295 K.

shot no	Mixture	PLIF	FOV	Schlieren	Framer	Chem.	Soot foil
89	H_2-N_2O-1.33N_2	yes	60	yes			
90	2H_2-O_2-3.5N_2	yes	60	yes			
91	H_2-N_2O-1.77N_2	yes	60				
92	H_2-N_2O-1.77N_2	yes	60	yes			
93	H_2-N_2O-1.77N_2	yes	60	yes			
94	H_2-N_2O-1.77N_2	yes	60	yes			
95	2H_2-O_2-12Ar	yes	30				
96	2H_2-O_2-12Ar	yes	30	yes			
97	2H_2-O_2-4.5N_2	yes	30				
98	2H_2-O_2-4.5N_2	yes	30				
99	2H_2-O_2-4.5N_2	yes	30				
100	2H_2-O_2-4.5N_2		30	yes			
101	2H_2-O_2-4.5N_2		30	yes			
102	2H_2-O_2-4.5N_2		30	yes			
103	2H_2-O_2-4.5N_2		30	yes			
104	2H_2-O_2-4.5N_2	yes	30	yes			
105	2H_2-O_2-4.5N_2		30	yes			
106	2H_2-O_2-4.5N_2	yes	30	yes			
107	2H_2-O_2-5.6N_2		30	yes			
108	2H_2-O_2-5.6N_2		30	yes			
109	2H_2-O_2-5.6N_2		30	yes			
110	2H_2-O_2-5.6N_2	yes	30	yes			
111	2H_2-O_2-5.6N_2	yes	30	yes			
112	2H_2-O_2-5.6N_2	yes	30	yes			
113	2H_2-O_2-5.6N_2		30	yes			
114	2H_2-O_2-5.6N_2	yes	30	yes			
115	2H_2-O_2-5.6N_2	yes	30	yes			
116	2H_2-O_2-5.6N_2	yes	30				
117	2H_2-O_2-5.6N_2		30	yes			
118	2H_2-O_2-5.6N_2	yes	30	yes			
119	2H_2-O_2-5.6N_2	yes	30	yes			
120	2H_2-O_2-5.6N_2	yes	30	yes			
121	2H_2-O_2-5.6N_2	yes	30	yes			
122	2H_2-O_2-5.6N_2	yes	30	yes			
123	2H_2-O_2-5.6N_2	yes	30	yes			
124	2H_2-O_2-5.6N_2	yes	30	yes			
125	2H_2-O_2-5.6N_2		30	yes			
126	2H_2-O_2-3.5N_2	yes	30	yes			
127	2H_2-O_2-3.5N_2	yes	30	yes			
128	2H_2-O_2-3.5N_2	yes	30	yes			
129	2H_2-O_2-12Ar	yes	60				

Table D.2: Narrow channel experiments. FOV is the height of the PLIF or chemiluminescence (Chem.) image. The field of view of schlieren images was about 146 mm and of framing camera images was about 138 mm. Initial pressure is 20 kPa unless otherwise noted, initial temperature is 295 K.

shot no	Mixture	PLIF	FOV	Schlieren	Framer	Chem.	Soot foil
130	$2H_2$-O_2-12Ar	yes	60	yes			
131	$2H_2$-O_2-3.5N_2	yes	60	yes			
132	$2H_2$-O_2-3.5N_2	yes	30	yes			
135	H_2-N_2O-1.64N_2	yes	30	yes			
136	H_2-N_2O-1.64N_2	yes	30	yes			
137	H_2-N_2O-1.64N_2	yes	30	yes			
138	$2H_2$-O_2-3.5N_2	yes	30	yes			
139	H_2-N_2O-1.77N_2	yes	30				
140	H_2-N_2O-1.77N_2	yes	30	yes			
143	$2H_2$-O_2-3.5N_2	yes	30				
144	$2H_2$-O_2-3.5N_2	yes	30	yes			
145	$2H_2$-O_2-3.5N_2	yes	30	yes			
146	1.76H_2-O_2-3.7N_2	yes	30	yes			
147	H_2-N_2O-1.77N_2	yes	30	yes			
148	H_2-N_2O-1.77N_2	yes	30	yes			
150	H_2-0.84N_2O-1.52N_2	yes	30	yes			
151	$2H_2$-O_2-5.6N_2	yes	30	yes			
152	H_2-N_2O-1.64N_2	yes	30	yes			
153	H_2-N_2O-1.64N_2	yes	30	yes			
154	H_2-N_2O-1.64N_2	yes	30	yes			
155	H_2-N_2O-1.64N_2	yes	30	yes			
156	2.8H_2-2.9N_2O-4.3N_2, 21.4kPa	yes	30	yes			
157	$2H_2$-O_2-3.5N_2	yes	30	yes			
158	H_2-N_2O-1.64N_2	yes	30				
159	H_2-N_2O-1.64N_2	yes	30	yes			
160	2.8H_2-2.7N_2O-4.4N_2	yes	30	yes			
161	H_2-N_2O-1.64N_2	yes	30	yes			
162	H_2-N_2O-1.64N_2	yes	30	yes			
163	H_2-N_2O-1.33N_2	yes	30	yes			
164	5.2H_2-2.5O_2-2.3CO_2, 21.3kPa	yes	30	yes			
165	$2H_2$-O_2-CO_2	yes	30	yes			
166	$2H_2$-O_2-5.6N_2	yes	30	yes			
167	$2H_2$-O_2-5.6N_2	yes	30	yes			
168	2.66H_2-1.11O_2-6.2N_2	yes	30	yes			
169	$2H_2$-O_2-5.6N_2	yes	30	yes			
170	$2H_2$-O_2-5.6N_2	yes	30	yes			
171	$2H_2$-O_2-3.5N_2	yes	30	yes			
172	$2H_2$-O_2-3.5N_2	yes	30	yes			
173	C_2H_4-3O_2-10.5N_2	yes	30	yes			
174	C_2H_4-3O_2-10.5N_2	yes	30	yes			
175	C_2H_4-3O_2-10.5N_2	yes	30	yes			

Table D.3: Narrow channel experiments. FOV is the height of the PLIF or chemiluminescence (Chem.) image. The field of view of schlieren images was about 146 mm and of framing camera images was about 138 mm. Initial pressure is 20 kPa unless otherwise noted, initial temperature is 295 K.

shot no	Mixture	PLIF	FOV	Schlieren	Framer	Chem.	Soot foil
176	C_2H_4-$3O_2$-$10.5N_2$	yes	30	yes			
177	C_2H_4-$3O_2$-$10.5N_2$	yes	30	yes			
178	C_2H_4-$3O_2$-$9N_2$, 26.9kPa	yes	30	yes			
179	$2H_2$-O_2-$3.5N_2$	yes	30				
180	C_2H_4-$3O_2$-$8N_2$	yes	30	yes			
181	C_2H_4-$3O_2$-$8N_2$	yes	30	yes			
182	C_2H_4-$3O_2$-$8N_2$	yes	30	yes			
183	C_2H_4-$3O_2$-$8N_2$	yes	30	yes			
184	C_2H_4-$3O_2$-$6N_2$	yes	30	yes			
185	C_3H_8-$5O_2$-$9N_2$	yes	30				
186	C_3H_8-$5O_2$-$9N_2$	yes	30	yes			
187	C_3H_8-$5O_2$-$9N_2$	yes	30	yes			
188	C_3H_8-$5O_2$-$9N_2$	yes	30	yes			
190	C_3H_8-$5O_2$-$9N_2$	yes	30	yes			
191	C_3H_8-$5O_2$-$9N_2$	yes	30	yes			
192	C_3H_8-$5O_2$-$9N_2$	yes	30	yes			
193	$2H_2$-O_2-$5.6N_2$	yes	30	yes			
194	$2H_2$-O_2-$4.5N_2$	yes	30	yes			
195	$2H_2$-O_2-$4.5N_2$		30	yes		yes	
196	C_2H_4-$3O_2$-$8N_2$		30	yes		yes	
197	C_2H_4-$3O_2$-$8N_2$		30			yes	
198	C_2H_4-$3O_2$-$8N_2$		30			yes	
199	C_2H_4-$3O_2$-$8N_2$		30	yes		yes	
200	C_2H_4-$3O_2$-$10.5N_2$		30	yes		yes	
201	$2H_2$-O_2-$3.5N_2$		30	yes		yes	
202	$2H_2$-O_2-$5.6N_2$		30	yes		yes	
203	H_2-N_2O-$1.64N_2$		30	yes		yes	
204	C_3H_8-$5O_2$-$9N_2$		30	yes		yes	
205	C_3H_8-$5O_2$-$9N_2$		60	yes		yes	
206	C_3H_8-$5O_2$-$9N_2$		60	yes		yes	
207	C_3H_8-$5O_2$-$9N_2$		60	yes		yes	
208	C_3H_8-$5O_2$-$9N_2$		60	yes		yes	
209	C_3H_8-$5O_2$-$9N_2$		60	yes		yes	
210	C_3H_8-$5O_2$-$9N_2$		60	yes		yes	
215	$2H_2$-O_2-12Ar				yes		
216	$2H_2$-O_2-12Ar				yes		
217	C_3H_8-$5O_2$-$9N_2$				yes		
218	$2H_2$-O_2-12Ar				yes		
220	$2H_2$-O_2-12Ar				yes		
227	C_3H_8-$5O_2$-$9N_2$				yes		
228	C_3H_8-$5O_2$-$9N_2$				yes		

Table D.4: Narrow channel experiments. FOV is the height of the PLIF or chemiluminescence (Chem.) image. The field of view of schlieren images was about 146 mm and of framing camera images was about 138 mm. Initial pressure is 20 kPa unless otherwise noted, initial temperature is 295 K.

shot no	Mixture	PLIF	FOV	Schlieren	Framer	Chem.	Soot foil
229	$2H_2$-O_2-12Ar				yes		
230	C_3H_8-$5O_2$-$9N_2$				yes		
232	$2H_2$-O_2-17Ar				yes		
234	C_3H_8-$5O_2$-$9N_2$				yes		
235	C_3H_8-$5O_2$-$9N_2$				yes		
236	C_3H_8-$5O_2$-$9N_2$				yes		
237	C_3H_8-$5O_2$-$9N_2$				yes		
238	$2H_2$-O_2-$5.6N_2$				yes		
239	$2H_2$-O_2-$4.5N_2$				yes		
240	$2H_2$-O_2-$3.5N_2$				yes		
246	C_2H_4-$3O_2$-$8N_2$				yes		
247	C_2H_4-$3O_2$-$8N_2$				yes		
248	C_2H_4-$3O_2$-$8N_2$				yes		
249	C_2H_4-$3O_2$-$10.5N_2$				yes		
251	C_2H_4-$3O_2$-$10.5N_2$				yes		
254	C_2H_4-$3O_2$-$10.5N_2$				yes		
256	H_2-N_2O-$1.64N_2$				yes		
258	H_2-N_2O-$1.64N_2$				yes		
260	$2H_2$-O_2-17Ar				yes		
266	H_2-N_2O-$1.64N_2$				yes		
267	$2H_2$-O_2-$4.5N_2$				yes		
268	C_2H_4-$3O_2$-$6N_2$				yes		

Table D.5: Narrow channel experiments. FOV is the height of the PLIF or chemiluminescence (Chem.) image. The field of view of schlieren images was about 146 mm and of framing camera images was about 138 mm. Initial pressure is 20 kPa unless otherwise noted, initial temperature is 295 K.

Appendix E Mechanism validation for N_2O mixtures

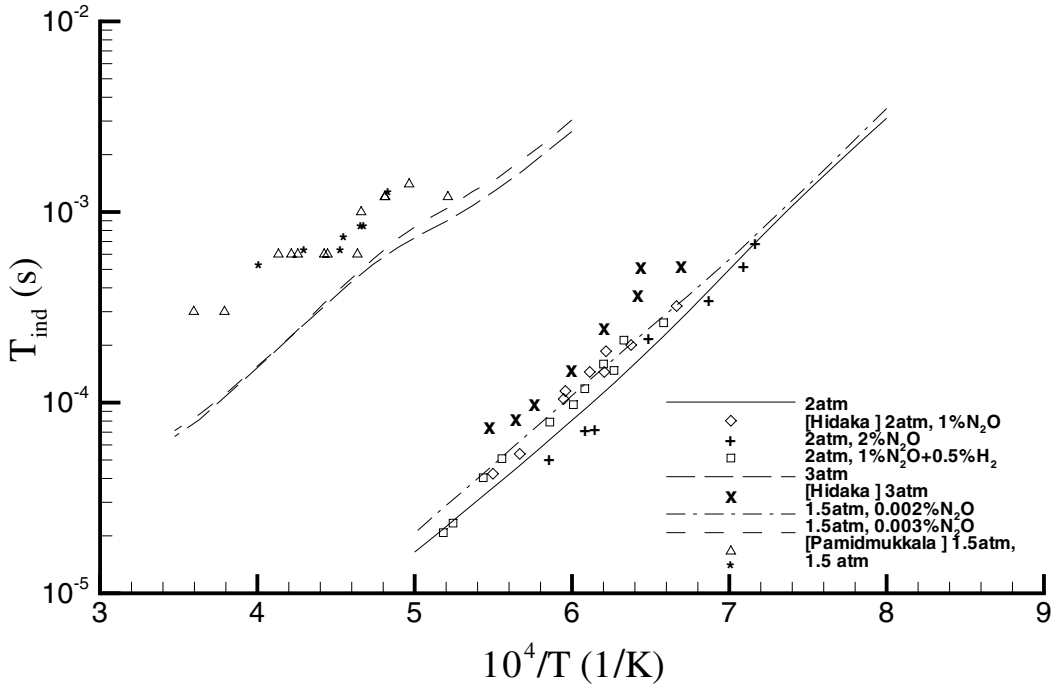

Figure E.1: Comparison of induction time calculated with detailed chemical kinetics mechanism of Mueller et al. (2000) with experimental data from Hidaka et al. (1985a), Hidaka et al. (1985b), and Pamidimukkala and Skinner (1982). Induction times are calculated assuming a constant volume adiabatic explosion, see Akbar et al. (1997).